Universidade de Aveiro
2014

Departamento de Engenharia de Materiais e Cerâmica

Eduardo Luis Trindade da Silva

Microelétrodos de Diamante para Estudos de Corrosão

Eduardo Luis Trindade da Silva

Diamond Microelectrodes for Corrosion Studies

o júri

presidente
Professor Doutor Luís Filipe Pinheiro de Castro
Professor Catedrático da Universidade de Aveiro

Professor Doutor Christopher Michael Ashton Brett
Professor Catedrático da Faculdade de Ciências e Tecnologia da Universidade de Coimbra

Professor Doutor Mário Guerreiro da Silva Ferreira
Professor Catedrático da Universidade de Aveiro

Professor Doutor Cristiano Simões de Abreu
Professor Adjunto do Instituto Superior de Engenharia do Instituto Politécnico do Porto

Doutora Sviatlana Lamaka
Investigadora Auxiliar Convidada do Instituto Superior Técnico da Universidade de Lisboa

Doutor Filipe José Alves de Oliveira
Investigador Auxiliar da Universidade de Aveiro

agradecimentos

Agradeço à minha família e amigos, fontes inesgotáveis de onde brotam a felicidade, o conforto, a inspiração, a energia e o embalo necessários à execução de qualquer capítulo desta vida, e sem os quais se torna descabido batalhar seja pelo que for.

Agradeço igualmente aos meus orientadores, (Dr.) Filipe Oliveira e (Dr.) Mikhail Zheludkevich, assim como ao (Prof. Dr.) Rui Silva, por todo o apoio e meios disponibilizados, e a todos os colegas que ajudaram a construir cada parte deste trabalho, com o sucesso, as qualidades e as imperfeições que lhe observo. Em todos eles encontrei preciosos colaboradores, guias e conselheiros, a cada passada deste doutoramento. Foi com a sua ajuda que se alcançaram as pequenas conquistas descritas neste documento, que julgo trazerem algum contributo de valor à ciência, embora me entristeça que o intercâmbio de conhecimento útil entre a ciência e o Mundo seja cada vez mais condicionado pela ignóbil perversão político-económica dos dias que correm.

palavras-chave

Diamante dopado com boro, Microelétrodos, Corrosão, Funcionalização da superfície.

resumo

Este trabalho teve como objetivos a produção, caracterização e aplicação de microelétrodos (MEs) de diamante como sensores amperométricos e potenciométricos em sistemas de corrosão nos quais a agressividade do meio e a presença de produtos de corrosão, constituem obstáculos que podem diminuir o desempenho, ou inviabilizar a utilização, de outros tipos de sensores.

Os microeléctrodos são baseados em filmes finos de diamante dopado com boro (BDD – Boron Doped Diamond) depositados sobre fios de tungsténio afiados, através do método de deposição química a partir da fase vapor, assistida por filamento quente (HFCVD – Hot Filament Chemical Vapor Deposition). A otimização das diversas etapas de fabricação dos MEs deu origem ao desenvolvimento de um novo sistema de afiamento eletroquímico para obtenção destes fios e a várias opções para a obtenção dos filmes de diamante condutor e seu isolamento com resinas para exposição apenas da ponta cilíndrica.

A qualidade cristalina dos filmes de diamante foi avaliada por espectroscopia de Raman. Esta informação foi complementada com uma caracterização microestrutural dos filmes de diamante por microscopia eletrónica de varrimento (SEM), em que se fez a identificação da tipologia dos cristais como pertencendo às gamas de diamante nanocristalino ou microcristalino.

Os filmes de BDD foram utilizados na sua forma não modificada, com terminações em hidrogénio e também com modificação da superfície através de tratamentos de plasma RF de CF_4 e O_2 indutores de terminações C-F no primeiro caso e de grupos C=O, C-O-C e C-OH no segundo, tal como determinado por XPS.

A caracterização eletroquímica dos MEs não modificados revelou uma resposta voltamétrica com elevada razão sinal/ruído e baixa corrente capacitiva, numa gama de polarização quasi-ideal com extensão de 3 V a 4 V, dependente dos parâmetros de crescimento e pós-tratamentos de superfície. Estudou-se a reversibilidade de algumas reações heterogéneas com os pares redox $Fe(CN)_6^{3-/4-}$ e $FcOH^{0/+}$ e verificou-se que a constante cinética, k_0, é mais elevada em elétrodos com terminações em hidrogénio, nos quais não se procedeu a qualquer modificação da superfície. Estes MEs não modificados foram também testados na deteção de Zn^{2+} onde se observou, por voltametria cíclica, que a detecção da redução deste ião é linear numa escala log-log na gama de 10^{-5}-10^{-2} M em 5 mM NaCl.

resumo (cont.)

Realizaram-se também estudos em sistemas de corrosão modelares, em que os microeléctrodos foram usados como sensores amperométricos para mapear a distribuição de oxigénio e Zn^{2+} sobre um par galvânico Zn-Fe, com recurso a um sistema SVET (Scanning Vibrating Electrode Technique). Foi possível detetar, com resolução lateral de 100 μm, um decréscimo da concentração de O_2 junto a ambos os metais e produção de catiões de zinco no ânodo. Contudo verificou-se uma significativa deposição de zinco metálico na superfície dos ME utilizados.

Os MEs com superfície modificada por plasma de CF_4 foram testados como sensores de oxigénio dissolvido. A calibração dos microeléctrodos foi efetuada simultaneamente por voltametria cíclica e medição óptica através de um sensor de oxigénio comercial. Determinou-se uma sensibilidade de ~0.1422 nA/μM, com um limite de deteção de 0.63 μM. Os MEs modificados com CF_4 foram também testados como sensores amperométricos com os quais se observou sensibilidade ao oxigénio dissolvido em solução, tendo sido igualmente utilizados durante a corrosão galvânica de pares Zn-Fe. Em alguns casos foi conseguida sensibilidade ao ião Zn^{2+} sem que o efeito da contaminação superficial com zinco metálico se fizesse sentir. Os microeléctrodos tratados em plasma de CF_4 permitem uma boa deteção da distribuição de oxigénio, exibindo uma resposta mais rápida que os não tratados além de maior estabilidade de medição e durabilidade.

Nos MEs em que a superfície foi modificada com plasma de O_2 foi possível detetar, por cronopotenciometria a corrente nula, uma sensibilidade ao pH de ~51 mV/pH numa gama de pH 2 a pH 12. Este comportamento foi associado à contribuição determinante de grupos C-O e C=O, observados por XPS com uma razão O/C de 0,16. Estes MEs foram igualmente testados durante a corrosão galvânica do par Zn-Fe onde foi possível mapear a distribuição de pH associada ao desenvolvimento de regiões alcalinas causadas pela redução do oxigénio, acima da região catódica, e de regiões ácidas decorrentes da dissolução anódica do ânodo de zinco. Com o par galvânico imerso em 50 mM NaCl registou-se uma variação de pH aproximadamente entre 4,8 acima do ânodo de zinco a 9,3 sobre o cátodo de ferro. A utilização pioneira destes MEs como sensores de pH é uma alternativa promissora aos elétrodos baseados em membranas seletivas.

keywords

abstract

This work was dedicated to the production, characterization and application of diamond microelectrodes (MEs) in corrosion systems as amperometric and potentiometric sensors in which the aggressive media and the presence of corrosion products can affect the performance, or even impede the use of other types of sensors.

The MEs are based in boron doped diamond (BDD) thin films grown by HFCVD (Hot Filament Chemical Vapor Deposition) on top of sharp tungsten filaments. The optimization of the various ME fabrication steps gave origin to a novel electrochemical etching technique for the production of sharp metal wires and to multiple options for the growth of diamond films and their insulation with resins in order to expose only the cylindrical tip.

The crystalline quality of the diamond films was evaluated with Raman spectroscopy. Complementary microstructural information was gathered by scanning electron microscopy (SEM), to identify the microcrystalline or nanocrystalline nature of the diamond coatings.

The BDD films were used in the as-grown form, with hydrogen terminated surface and also with surface modification, by RF-plasma, using CF_4 and O_2 for inducing different surface terminations, C-F bonds in the first case and C=O, C-O-C and C-OH in the second, as detected by XPS.

The electrochemical characterization of the MEs revealed a voltammetric response with high signal-to-noise ratio and low capacitive current. The potential range of water stability varied from 3 V to 4V, depending on the growth parameters and surface treatments. Heterogeneous electron transfer kinetics were measured using the $Fe(CN)_6^{3-/4-}$ and $FcOH^{0/+}$ redox couples and it was verified that the kinetic constant, k_0, is higher for the as-grown MEs than for the modified ones. The as-grown MEs were used for the detection of Zn^{2+} exhibiting a log-log linear response in the range of 10^{-5}-10^{-2} M in 5 mM NaCl, by cyclic voltammetry. Studies in model corrosion systems were also performed in which the MEs were used as amperometric sensors to map the distribution of oxygen and Zn^{2+} above a corroding galvanic Zn-Fe couple, by using a SVET (Scanning Vibrating Electrode Technique) system. It was possible to detect with a lateral resolution of 100 µm, a decrease in O_2 concentration above both metals and the release of zinc cations above the anode. However, a significant zinc deposition at the surface of the electrodes was observed.

abstract (cont.)

The MEs modified by CF_4 plasma were tested as dissolved oxygen sensors. The calibration of the microelectrodes was performed simultaneously by cyclic voltammetry and optical measurement with a commercial oxygen sensor. A sensitivity of ~0.1422 nA/µM was determined, with a detection limit of 0.63 µM. The fluorinated MEs were also tested during galvanic corrosion of Zn-Fe couples. In some cases sensitiveness to Zn^{2+} was also achieved without zinc contamination. The CF_4 plasma treated MEs allow a good oxygen mapping, showing a faster response than the as-grown MEs, as well as higher measurement stability and longer lifetime.

For the O_2 plasma treated MEs it was possible to detect, by zero-current chronopotentiometry, a pH sensitivity of ~51 mV/pH in a pH 2 to pH 12 range. This behavior was attributed to the contribution of the C-O and C=O groups, observed by XPS with an O/C ratio of 0.16. These MEs were also tested during the galvanic corrosion of a Zn-Fe couple where it was possible to map the pH distribution deriving from the development of alkaline regions caused by oxygen reduction, above the cathode, and of acidic regions resulting from the anodic dissolution of zinc. With the galvanic couple immersed in 50 mM NaCl a pH variation was registered from ca. 4.8 above the zinc anode to 9.3 above the cathode. The innovative use of these MEs as pH sensors is a promising alternative to the selective membrane based MEs.

Contents

List of Figures

viii

List of Tables

Roman Symbols

A – Area

A_a – anodic area

A_c – cathodic area

b, c, p, q – geometric factors

b_a – anodic Tafel slope

b_c – cathodic Tafel slope

C – analyte concentration

C_d – double-layer capacitance

C_d^0 - specific capacitance

C_j - concentration of species j

$C_j (r, t)$ - concentration of species j at radial distance r at time t

$C_j (x, t)$ - concentration of species j at distance x at time t

d_{CE} – counter electrode diameter

d_{fes} – diameter of the column of flowing electrolyte solution

d_W – wire diameter

e – electron charge

E – electrode potential

D – a) diffusion coefficient

    b) wire diameter

D_j - diffusion coefficient of species j

E_C – Conduction band minimum

E_F – Fermy level

E_G – gap energy

E_V – valence band maximum

E_{Vac} – vacuum level

F - the Faraday constant

H – aspect ratio

I_c – charging current

I_{corr} – corrosion current

I_p^{ox} – oxidation peak current

I_p^{red} – reduction peak current

i_{qss} – quasi steady-state current

i_{ss} – steady-state current

$i(\omega)$ – current density at frequency ω

J – current density

$J_j (x)$ - flux of species j at location x

K – charge mobility

k_0 – standard rate constant

l - distance

L – length of sharpened region of a metal wire

n - stoichiometric number of electrons involved in an electrode reaction

p - pressure

Q – charge density

r –   a) radial distance from the electrode center

    b) microelectrode radius

R – a) ideal gas constant

    b) tip radius

R_c – cell resistance

R_M – metal resistance

R_p – polarization resistance

R_S – solution resistance

R_u – uncompensated resistance

t – a) forward scanning time

    b) charging time

T – absolute temperature

$V(\omega)$ – potential at frequency ω

$Z(\omega)$ – impedance at frequency ω

z_j - charge on species j

Greek Symbols

α – anodic charge transfer coefficient

β – cathodic charge transfer coefficient

γ - tip aperture angle

δ - diffusion layer thickness

$\Delta\phi_a$ - difference of electric potential at the anodic site

$\Delta\phi_c$ – difference of electric potential at the cathodic site

$\Delta\phi_S$ – difference of electric potential in solution

ΔE – potential variation

ΔE_p – difference between anodic and cathodic peak potentials

ε – a) electrochemical potential

    b) permittivity

η_a – anodic overpotential

η_c – cathodic overpotential

κ – solution conductivity

μ - fluid viscosity

μ_{SHE} – electrochemical potential of the standard hydrogen electrode

ν - fluid velocity

ρ – fluid density

σ – charge density

$\phi(x)$ - electrostatic potential at distance x

$\phi_{M,a}$ – electric potential of the metal on an anodic site

$\phi_{M,c}$ – electric potential of the metal on a cathodic site

$\phi_{S,a}$ – electric potential of the solution on an anodic site

$\phi_{S,c}$ – electric potential of the solution on a cathodic site

χ – electron affinity

Standard Abbreviations

AC – Alternate Current

BDD – Boron Doped Diamond

BEN – Bias Enhanced Nucleation

B-MCD – Boron Doped Microcrystalline Diamond

B-NCD – Boron Doped Nanocrystalline Diamond

CBM – Conduction Band Minimum

CE – Counter Electrode

CNT – Carbon Nanotube

CV – Cyclic Voltammetry

CVD – Chemical Vapor Deposition

DC – Direct Current

EDS - Energy Dispersive X-ray Spectroscopy

EELS - Electron Energy Loss Spectroscopy

ET – Electron Transfer

F-BDD – Fluorinated Boron Doped Diamond

FE-SECM – Field Emission Scanning Electrochemical Microscopy

FIB – Focused Ion Beam

FWHM – Full Width Half Maximum

GDP – Gross Domestic Product

GSH - Reduced form of Glutathione

AFM – Atomic Force Microscopy

ATP – Adenosine Triphosphate

HER – Hydrogen Evolution Reaction

HFCVD – Hot Filament Chemical Vapor Deposition

HOPG – Highly Ordered Pyrolytic Graphite

IC-SECM – Intermittent Contact Scanning Electrochemical Microscopy

ISE – Ion-Selective Electrode

ISFET - Ion-Sensitive Field-Effect Transistor

LEIS - Local impedance electrochemical spectroscopy

MCD – Microcrystalline Diamond

ME - Microelectrode

MWCNT – Multi-Wall Carbon Nanotubes

NCD – Nanocrystalline Diamond

PAN – Polyacrylonitrile

PDEIS – Potentiodynamic Electrochemical Impedance Spectroscopy

RF – Radio Frequency

SCE – Standard Calomel Electrode

SECM – Scanning Electrochemical Microscopy

SEM – Scanning Electron Microscopy

SIET - Scanning Ion-selective Electrode Technique

SKP – Scanning Kelvin Probe

STM –Scanning Tunneling Microscopy

SVET – Scanning Vibrating Electrode Technique

SWCNT – Single-Wall Carbon Nanotubes

TEM – Transmission Electron Microscopy

TPA – Transpolyacetylene

UME - Ultramicroelectrode

UV – Ultraviolet

VBM – Valence Band Maximum

XPS - X-ray photoelectron spectroscopy

1. Introduction

The study of electrochemistry and its applications involves chemical processes in which there is electron transfer across an interface. This interface usually exists between an electrically conducting solid, the electrode, and a solution, the electrolyte.

The relevance of electrochemical science extends well into domains with large economic influence such as corrosion and common large-scale chemical processes such as electroplating, electrochemical sensors, batteries, fuel cells and electrochromic displays presenting electrochemical working mechanisms.

Estimates on worldwide market research point to a cost of 1.66 billion (10^{12}) euros due to corrosion alone in 2012 (over 3% of the world's GDP), including maintenance, prevention, replacement of parts and interruption of services due to maintenance [1]. Forecasts for the global fuel cells market indicate a fast growing tendency from 583 million euros in 2012 to 10.6 thousand million euros by 2022. Biosensors and chemical sensors are expected to present the most significant growth in the sensors market with an estimated value of 9.7 thousand million euros in 2011 growing to 15 800 million in 2016 [2].

The strong development of nanotechnology and biotechnology has created demand for research on novel sensors that can meet today's necessities but always regarding those of tomorrow. Electrochemical sensors can generally provide high sensitivity and accuracy at low cost. Adequate selection of an electrode material involves considering the nature of its working environment. Often these can be quite aggressive, exhibiting very high or very low pH, which requires chemical and microstructural stability along with robustness and corrosion resistance. In biological media electrodes may become easily unusable by adsorption of certain substances and compounds such as electrically insulating films or biomolecules. Amperometric sensors frequently struggle with the need to catalyze a particular redox process at a given potential, yielding a measurable and reproducible current without interference of background signals arising from unwanted capacitance in the circuit or competing electrochemical reactions.

Diamond, regarded for a long time only as a highly insulating material, has been reinvented by doping with elements such as boron, sulfur, nitrogen and phosphorus, to work as a semiconductor or quasi-metal, widening the span of applications. Thus, as an electrochemical sensor or electrode, research on doped diamond has been growing

significantly since the mid 90's, especially due the advantages of its use in comparison to traditional electrode materials such as glassy carbon or platinum. Good sensitivity, reproducibility, and both fast and easy-to-measure signal response are valued characteristics for an electrode. Diamond electrodes can meet these requirements and in some cases surpass the electrochemical behavior of metal electrodes or other carbon electrodes (glassy carbon, carbon fiber, etc.).

Electrodes of this material display minimal background response, enabling selective measurement of the pretended signal. This behavior origins from a low double-layer capacitance density (~10 $\mu F.cm^{-2}$), chemically inert surface comparing e.g. with other carbon electrodes which may present high concentration of redox active groups on the surface which translate into background peaks or pseudo-capacitive background in voltammetry data. Another very important feature is the range of electrical potential without decomposition of the solvent. Taking the universal example of water, hydrogen evolution starts at negative potentials whilst oxygen evolution occurs at positive potentials. The magnitude of these currents is variable but in most cases electroanalysis is restricted to the small potential window defined by the range for which such currents are insignificant and electrode operation is possible. For a platinum electrode this window is narrow, around 1.5 V. In contrast water decomposition tends to be very slow at diamond electrodes, enabling signal recording of redox processes to be widened to a 3-5 V potential window depending on the diamond synthesis parameters and surface conditioning.

Electrode fouling is common in electrodes displaying polar, hydrophilic surfaces (e.g. glassy carbon). In contrast, the diamond surface, normally hydrophobic, and with absence of reactive groups can provide a rather inert surface with fouling resistance, even in biological media. Hence, diamond electrodes are more predisposed to present both capability to work in harsh environments and a long term stability.

In the beginning a well-defined plan was established for this work. Diamond microelectrodes were planned to be produced on the basis of boron doped nanocrystalline diamond. The final electrode design would consist of bilayer all-diamond microelectrodes (Figure 1.1). After adequate characterization, these probes would be

used for studying the performance of corrosion protective coatings with self-healing character. Trials for bio-applications would be performed as well.

The real working course, however, was balanced by a logical sequence defined during the progress of the work, along with all the variables involved in the accomplishment of each task.
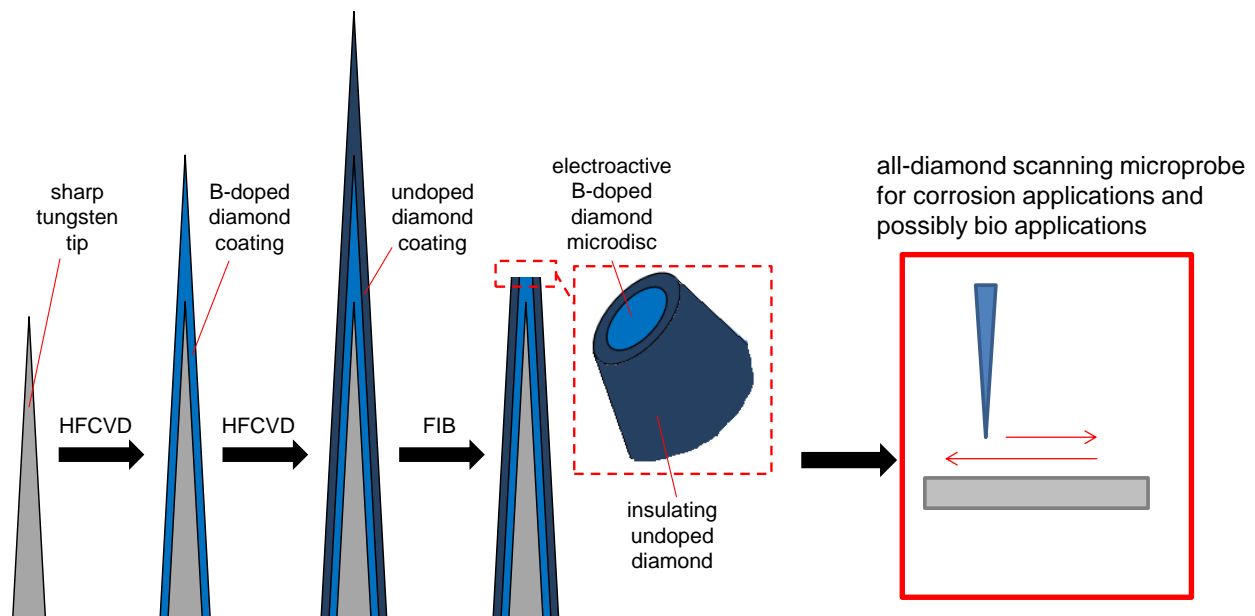
Figure 1.1 – Idealized diamond microelectrode fabrication sequence.

The diagram in Figure 1.2 provides a description of the author's line of thought and helps the reader to follow the mind map of this work. The course of action taken led to the fulfillment of much of the initial objectives, while expanding the range of applicability of diamond MEs.

The present document aggregates the most relevant information gathered during these past few years and is structured in three main chapters, besides this brief Introduction (Chapter 1) and the final ones regarding the main Conclusions (Chapter 5) and the immediate future work (Chapter 6). Chapter 2 gives a theoretical background of the most relevant topics that constitute the scope of this work. Chapter 3 is dedicated to all the fabrication procedures involving diamond microelectrodes, from substrate preparation to electrical insulation and, besides important information acquired from reference authors, it includes one submitted paper (Chapter 3.3), deriving from a patent

application submitted to INPI (Instituto Nacional de Propriedade Industrial) ("*ELECTROCHEMICAL ETCHING DEVICE, METHOD FOR ELECTROCHEMICAL ETCHING AND THEIR USE",* nº 106894) and one paper (Chapter 3.6) published during the early stages of the present development.
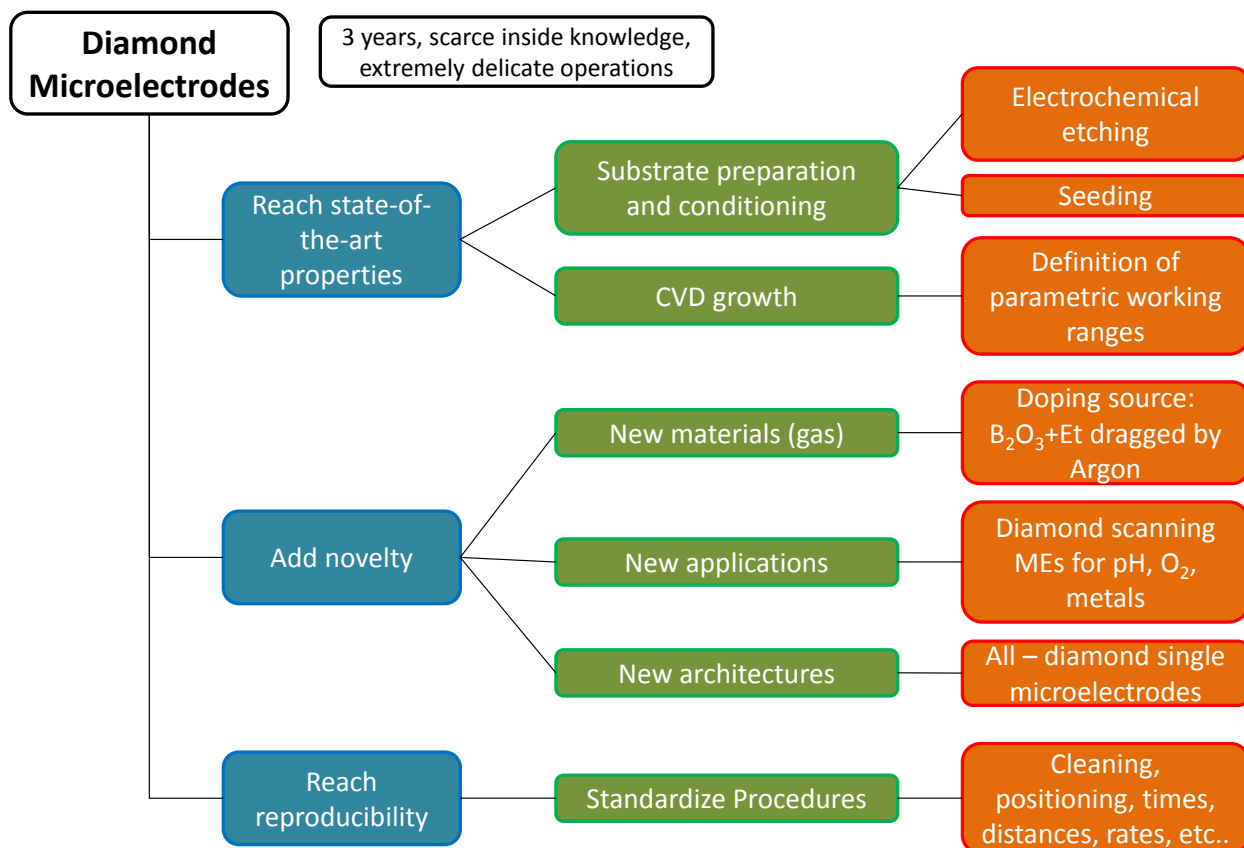
Figure 1.2 – Work sequence.

The practical application of diamond microelectrodes in corrosion systems is the main content of Chapter 4 where, apart from a theoretical background regarding aqueous corrosion and relevant localized electrochemical techniques, the main body corresponds to the full content of two published papers (Chapter 4.3 and Chapter 4.5) and another recently submitted (Chapter 4.4).

2. Bibliographic overview

2.1.   Microelectrodes

When the size of an electrode becomes close to the size of the electric Helmholtz double layer its behavior significantly deviates from conventionally sized electrodes, with some associated advantages. Until today there is not much agreement in what concerns the definition of a microelectrode (ME), probably because it has been changing over time [3]**.** Different terminologies can be found in the literature cataloguing microelectrodes in different size ranges from 10 nm - 100 µm. The theoretical considerations involving such small sensors are related to the mass transport regime and the kinetic parameters of an experiment. The official IUPAC definition [4] of a microelectrode states that:

"Microelectrode is any electrode whose characteristic dimension is, under the given experimental conditions, comparable to or smaller than the diffusion layer thickness, δ. Under these conditions, a steady state or a pseudo steady state (cylindrical electrodes) is attained".

Although one acknowledges the above mentioned to be true, it is a somewhat broad definition if a concise document is to be written. Thus, for the sake of simplicity and because a characteristic dimension of ≤ 25 µm has been considered by some reference authors [5], from hereon we will adopt this same dimension for defining a microelectrode.

By having such operation size, MEs display fast double-layer charging, reduced ohmic loss, and high diffusion limited mass-transport rates by working in the steady state regime. For diffusion-controlled processes, minimal ohmic drop is achieved at the steady-state limit [6].

2.1.1. Electrochemistry at microelectrodes

Oxidation and reduction of redox-active analytes at an electrode surface will generate a concentration gradient between the interfacial region and the bulk solution. These processes involve electron transfer across the interface and the rate at which it takes

place determines the heterogeneous electron-transfer (ET) rate constant, k^0. If this kinetic constant is large it means that ET is fast and mass transport is the limiting step of the reaction. Electrode reactions can be accompanied by three mass transport processes:

Diffusion – consists on the spontaneous movement of species due to the existence of a concentration gradient, normally from higher to lower concentration zones in order to establish equilibrium. It is a thermodynamically driven process that can be mathematically formalized by equating the chemical potential and the frictional force acting on the analyte species.

Convection – this process is due to the influence of external agents and can be naturally driven or forced. Natural convection can derive from, e.g., thermal agitation or density gradients, while stirring or flow movement are common forms of forced convection.

Migration – This type of transport is based on the movement of charged species by action of an electric field.

The Nernst-Plank equation relates the unidirectional diffusion of a species j to these three modes of mass transfer (Eq. 2.1)

$$J_j(x) = -D_j \frac{\partial C_j(x)}{\partial x} - \frac{z_j F}{RT} D_j C_j \frac{\partial \Phi(x)}{\partial x} + C_j v(x) \qquad \textbf{(}\text{Eq. 2.1}\textbf{)}$$

where $J_j(x)$ represents the one-dimensional flux for species j at distance x from the electrode, D_j is the diffusion coefficient, z_j is the charge, C_j is the concentration for the species $j, v(x)$ is the rate at which a volume element moves in solution, $\partial C_j(x)/\partial x$ is the concentration gradient, and $\partial \phi_j(x)/\partial x$ is the potential gradient.

Upon application of a potential step that can promote steady-state, diffusion controlled electrolysis, it is important to acknowledge the current dependence with time and electrode size. Taking a uniformly accessible spherical electrode in a solution in which only a redox-active species is present with a concentration, C_j, in an electrolytic

solution, the solution of Fick's second law in spherical coordinates (Eq. 2.2) describes the concentration gradient that can be found at the electrode surface [6, 7].

$$\frac{\partial C_j(r,t)}{\partial t} = D_j \left[\frac{\partial^2 C_j(r,t)}{\partial r^2} + \frac{2}{r} \frac{\partial C_j(r,t)}{\partial r} \right]$$

(Eq. 2.2)

Boundary conditions:

$\lim_{r \to \infty} C_j(r,t) = C_j^{\infty}$

$C_j(r,0) = C_j^{\infty}$

$C_j(r,t) = 0$ for $t > 0$

Where r is the radial distance from the electrode center. By applying Laplace transforms to this equation, one can obtain the following current-time dependence:

$$i(t) = \frac{nFADC^{\infty}}{r} + \frac{nFAD^{1/2}C^{\infty}}{\pi^{1/2}t^{1/2}}$$

(Eq. 2.3)

where n is the number of electrons transferred in the redox reaction, F is Faraday's constant, D is the diffusion coefficient, A is the geometric electrode area, C is the analyte concentration, r is the electrode radius and t is the forward scanning time [7]. This equation reveals a time dependent term and a time-independent one. Hence different mass transport regimes can be found for different time scales.

For short times (fast scan rates) (Eq. 2.4) the thickness of the diffusion layer without reactants is very small in comparison to the electrode that appears as an infinite plane (Fig. 2.1). Mass transport will occur by linear diffusion at such short times and the second term of equation (Eq. 2.4) will be much larger than the first one (Eq. 2.5).

$$i_t = \frac{nFAD^{1/2}C^{\infty}}{\pi^{1/2}t^{1/2}}$$

(Eq. 2.4)

$$i_{ss} = \frac{nFADC^{\infty}}{r}$$

(Eq. 2.5)

For longer times the contribution from the second term in Eq. 2.3 will lose its relevance on behalf of the first one (Eq. 2.5). At this time scale the thickness of the double layer will be larger and the shape of the microelectrode will become increasingly important, with radial diffusion occurring predominantly (Fig. 2.1). Under these conditions the current achieves a steady-state value, because the rate of electrolysis is equal to the rate at which the redox-active species diffuse through the double layer to the electrode surface. Dividing equation 2.4 by equation 2.5 yields a dimensionless parameter Dt/r_0^2 which indicates the time span at which the steady-state current contribution prevails over the transient response. Therein, it can be observed that achieving steady state with large scale electrodes is not impossible but becomes unpractical because of the long experimental time scale that would be necessary. Due to the enhanced mass transport to and from the microelectrode, a steady-state voltammetric experiment is characterized by a sigmoidal current-potential relationship [7]. Conversely to the peaked shape on conventional large scale electrodes, Figure 2.1a, which reflects the depletion of reactants near the electrode surface, a sigmoidal curve translates the attainment of a plateau current value that derives from the limiting rate of analyte that continuously reaches the electrode surface by diffusion through the double-layer (Figure 2.1b).
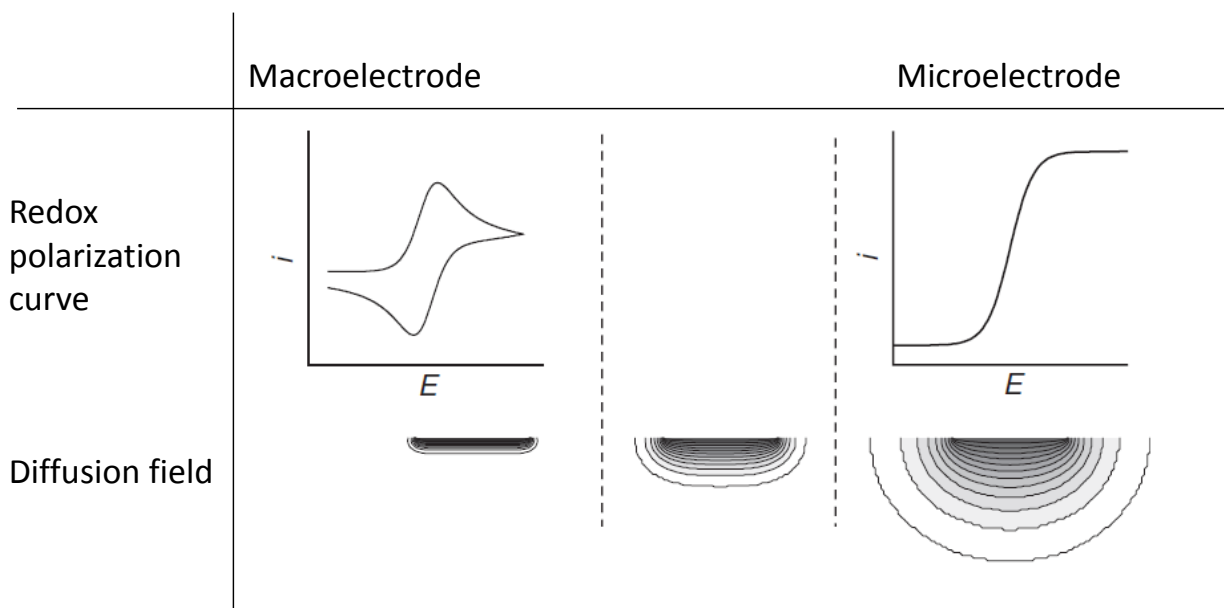
Figure 2.1 – Characteristic redox polarization curve shapes of macro and microelectrodes according to the type of established diffusion field (adapted from [6]).

2.1.1.1. Reduced Capacitance

In the interfacial region between an electrode and an electrolytic solution there is formation of a double layer composed of ions establishing the electric neutrality between the electrode surface and the bulk solution. Analogy can be made with an electric circuit in which the double layer behaves as a capacitor which is charged when potential is varied in the electrolytic cell. In consequence, there is a delay in applying the desired potential, which is only reached when the double layer is charged. Moreover for short time experiments the overall current will be a mixture of Faradaic and charging components (Eq. 2.6). Hence it is important to minimize the complicating influence of the capacitive current, I_c, by reducing its magnitude and lowering the charging time [7].

$$I_c = \frac{\Delta E}{R_c} e^{-t/R_c C_d} \qquad \text{(Eq. 2.6)}$$

C_d, double layer capacitance
R_c, cell resistance
t, charging time

Every double layer has a cell time constant, $R_u C_d$, where R_u is the uncompensated resistance and C_d is the double-layer capacitance. The cell time constant imposes a limit to the time scale that can be used in a given experiment. It is unreasonable to work on a time scale below $5R_u C_d$ and for full establishment of a potential step a value of at least $10R_u C_d$ must be considered [7]. The double layer capacitance is described by

$$C_d = \pi r^2 C_d^0 \qquad \text{(Eq. 2.7)}$$

C_d^0, specific capacitance

Hence, since the double layer capacitance varies with the square of the electrode radius, reducing the size of the electrode from the millimeter to the micrometer range implies reducing the capacitance a million times [6,8].

The electrode size also dictates the magnitude of the uncompensated resistance which is described by the following relation:

$$R_u = \frac{1}{4\pi\kappa r} \qquad \text{(Eq. 2.8)}$$

κ, solution conductivity

In this case the variation is inversely proportional to the electrode radius and the uncompensated resistance will increase the smaller is the electrode. However, considering that the double layer capacitance varies with r^2 the cell time constant R_uC_d will decrease proportionally to the electrode radius [8].

2.1.1.2. Ohmic Effects

The ohmic load of the electrochemical cell means that the potential applied is diminished by an amount, iR. Hence, depending on the current magnitude and the cell resistance, strong distortions can be observed experimentally. The low currents observed at microelectrodes come, therefore, as an advantage since they often are in the pA to nA range. Considering the time-scale and dependence of resistance with $1/r$, for short times the product iR will be directly proportional to the electrode radius, since the current varies with the electrode area, i.e. proportionally to r^2. According to eq. 2.5, for long times iR will be independent of the electrode radius. This means that by working with small microelectrode currents, ohmic effects will be always minored, although in this case the transient regime becomes even more advantageous than the steady-state one [7].

2.2. The importance of geometry and the origin of non-ideal responses

Shrinking the size of an electrode from millimeters to micrometers has important experimental implications. Reduced capacitance, negligible ohmic drop and working in the steady-state are more easily achievable with ME geometries in which all dimensions are small, instead of just one critical dimension, as is the case with cylinder and band MEs. Hence the most used ME geometries are disks, rings, ring-disks, hemispheres, spheres and cones (Figure 2.2) [9]. The ease of fabrication is even a more critical factor in the geometry selection. In fact, from the above, the disk geometry is among the most frequently used, but this shape is far from ideal because the enhanced mass transport at the circular edge of the disk tends to make the center less accessible to electroactive species. However, disk MEs have the enormous advantage of being easily made by simply sealing a metal wire in glass, which also makes them easy to clean by mechanical polishing [6,7].

Figure 2.1 shows the shape of the expected voltammetric waves and corresponding diffusion profiles that result from the transition of large scale to microscale electrodes. However even if the size of a microelectrode and the scan rate of the experiment are low enough, the typical sigmoidal polarization curve may not be observed. Deviations from the ideal behavior often originate from imperfect sealing, which leads to unexpected capacitance and ohmic effects.

Other cases include surface impurities or stray capacitance, which can be ignored with big electrodes or in low frequency measurements, but can contribute significantly when using microelectrodes because its magnitude is similar to that of the double-layer.
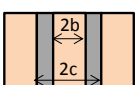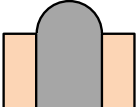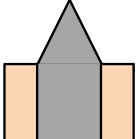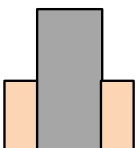
Microelectrode geometry	Difusion limited current equation
disk	$i_{ss} = 4nFDCr$
ring	$i_{ss} = nFDCl$
	$l = \frac{[\pi^2(b+c)]}{\ln[16(b+c)/(c-b)]}, c/b{<}1.25$
hemisphere	$i_{ss} = 2\pi nFDCr$
cone	$i_{ss} = 4nFDCr(1 + qH^p)$ H, aspect ratio q = 0.30661 p= 1.14466
cylinder	$i_{qss} = \frac{2nFADC}{r\ln\tau}$ t, forward scanning time
	$\tau = \frac{4Dt}{r^2}$

Figure 2.2 – Common microelectrode geometries and their steady-state current equations.

The study of electrochemistry comprises three main variables: potential, current and time. The interdependence between the three is the origin of the various existing techniques. Potentiometry gives the measurement of ion activity at zero current of the sensing electrode vs. an adequate reference electrode, although constant current can also be used. Chronopotentiometry refers to potential measured as a function of time. Fast response, high selectivity and low detection limit are desirable qualities of a potentiometric sensor.

Voltammetry deals with the measurement of current or potential by varying the potential or current, respectively, with time. Amperometry is the term applied if a fixed potential is used and if the measurement involves varying current with time, the technique is called chronoamperometry. These measurements require that the analyte is electroactive and it is desirable that the sensor exhibits a suitable potential range and that no decomposition is observed from the solvent. Coulometry and chronocoulometry can

also give valuable information as they consist on the measurement of transferred charge [10].

Considering their ambiguous definition throughout the years, there are a number of relevant milestones since the first use of microelectrodes, which can be dated back to some 70 years ago. After the introduction and success of the glass pH-selective electrodes by Cremer in 1906 [11], their miniaturization to microelectrodes has been propelled mainly by life scientists given the micrometer scale of cells, and the possibility of studying small volumes with minimum damage to the surrounding environment and resolved information [9]. Nowadays potentiometric microelectrodes are mainly based on liquid ionophore containing membranes that allow the measurement of more than fifty types of ions, in some cases with detection limits below 10^{-10} M [12]. Novel fabrication approaches are currently under research aiming at the substitution of liquid membranes by solid ones, promising simplified fabrication procedures and even lower limits of detection [12,13].

Novel materials for voltammetric microelectrodes have also been developed. The traditional use of metals such as platinum and gold has not ceased but their properties and assembling methods have taken a step further by using them in the form of nanoscale particles and as integrant parts of composite electrodes, particularly for taking advantage of their catalytic properties. New carbon materials have been discovered and reinvented, such is the case of carbon nanotubes (CNTs), graphene and diamond. Their use has given access to new mechanistic studies of biological processes and others. Besides the intrinsic characteristics of electrodes, a significant part of research on the development of electrodes is currently dedicated to electrode functionalization in order to detect complex molecules otherwise out of reach. Below is a brief summary of the characteristics of main state-of-the-art electrode types and an overview on new trends.

2.2.1. Potentiometric microelectrodes

Potentiometric probes are an acute analytical tool that provides quantitative chemical information on the activity of ions composing a sample solution. Cremer's discovery of the pH-sensitive glass membrane electrode launched the research concerning other

ions [14]. The first sodium selective glass electrode was introduced by Eisenman and co-workers [15]. Pungor et al. [16] were the first to prepare reliable electrodes with selectivity to different ions, nowadays termed ion selective electrodes (ISE). This was achieved by embedding soluble inorganic precipitates in hydrophobic membranes, which exhibited near-Nernstian response towards different ionic species. The developed membranes were based on a cold vulcanized silicon rubber matrix and these electrodes were produced and commercialized on large scale. A variety of works followed, among which Frant and Ross introduced fluoride and calcium selective electrodes, the first based on lanthanum fluoride crystal and the latter on a liquid ion-exchanger [17]. A milestone was achieved by Simon and co-workers [18] by showing that neutral organic molecules could behave as selective complex forming ligands, the birth of today's ionophores. The new neutral ionophore containing membranes excluded every ionic species except for the one compatible with host ligand chemistry, and was superior to the moderate selectivity of the existing ion-exchanger–based electrodes. The ionophores started by being dissolved in diphenyl ether and were later incorporated in plasticized PVC membranes [19,20]. In what regarded the preparation procedures, the work of Thomas describing the assembly of plasticized PVC membranes containing electrically charged and neutral ligands, was an important reference followed for many years [21]. Since then the main improvements have been related to selectivity and to the introduction of new ionophore cocktails for different ions. More than a decade ago, the identification of the factors restraining the detection limits for liquid membranes allowed a dramatic improvement in this area, of more than six orders of magnitude, allowing liquid membrane based ISEs to access the picomolar range [22]. Regardless, micropipette electrodes still suffer from complex fabrication, spontaneous leakage, fragility and short life time [23]. Consequently the current research trend on ISE development is related to finding electrodes with higher durability and requiring less maintenance. Simpler fabrication and higher levels of miniaturization are also on demand. Conducting polymers are currently the most promising materials for working as ion-to-electron transducers or even as the sensing membrane, which allows the fabrication of all-plastic ISEs [24,25].

2.2.2. Voltammetric/amperometric microelectrodes

The measurement of current strongly brings up the advantages of using microelectrodes. The only advantage of using potentiometric microprobes is the degree of resolution, since signal intensity is size independent. Conversely, the microelectrode additional properties such as enhanced signal-to-noise ratio and negligible ohmic drop only manifest at current measuring MEs. Since voltammetry and amperometry both deal with measuring oxidation and reduction currents, the rate at which reactions of interest can proceed at an electrode surface, i.e. electrode kinetics, are a matter of interest. Metal microelectrodes generally exhibit the highest electron transfer rates. Platinum and gold are the most commonly used solid metal electrodes because of their superior chemical stability among metals. Also, their use is often related to the ability to catalyze certain reactions such as hydrogen evolution on platinum or oxygen evolution on gold [26]. Besides these noble metals, there is a considerable range of electrochemically interesting metals such as silver, palladium, iridium, tungsten, etc, which are well described in specialized literature [27]. However, the formation of oxide films under certain potential-pH conditions is a limiting factor for the use of metals and their catalytic properties can be a problem because they restrain the working potential range. Furthermore they easily undergo fouling, which is a strong inconvenient in highly demanding applications such as biotechnology, particularly *in vivo*.

Carbon electrodes can attenuate the drawbacks of metals. Their window of stability in aqueous and non-aqueous media tends to be much larger than that of metal electrodes and passivation or electrode fouling are much less favorable. Their main drawback is the kinetics of electron transfer, which tends to be slower than in metals, although the use of nanocarbon forms such as graphene and carbon nanotubes can exhibit fast kinetics [28].

For the above mentioned reasons, glass insulated platinum or carbon fiber microelectrodes, which were two of the most widely used ME types, now inspire more elaborated fabrication approaches based on composite materials. Other approaches seek specificity towards reactions of interest and involve functionalization with ligand molecules and compounds that can promote immobilization of species of interest and/or bridge electron transfer between electrode and analyte. Broadly speaking the most

interesting routes of microprobe fabrication are based in either metallic or carbon probes modified with metallic nanoparticles, CNTs, polymeric films or even enzymes. The 80s brought the introduction of Nafion coatings [29,30], which are only permeable to cations and were since then widely used for modification of carbon electrodes for brain research. The use of self-assembled monolayers, consisting of well-ordered and densely packed layers of organic molecules also became popular for altering chemical and electrochemical behavior of surfaces with most studies being dedicated to alkanethiols on gold [31,32]. The main advantage of self-assembled monolayers is the possibility to easily acquire different chemical functionalities allowing to control interfacial properties of an electrode at the molecular level [33]. These layers can exhibit a variety of distinct properties allowing them to work as organic semiconductors, electrochromic materials, photocatalytic materials, or even as immobilizers for molecules of interest [34].

The popularization of nanomaterials evidenced the relevance of surface area in improving electron transfer and increasing limits of detection. Moreover they brought the possibility of easily assembling microelectrode or nanoelectrode arrays, which as individual MEs allow enhanced sensing ability [35–37]. Stabilized gold nanoparticles were the debut of nanosensors [38], with early on exceptional sensing performance. Another landmark was the appearance of carbon nanotubes which added outstanding electronic and mechanical properties to great surface area and possibility of functionalization [39]. The latest landmark on nanomaterials was the discovery of graphene, which like CNTs is a very promising carbon material [40].

Evermore complex material combinations are being put together for the fabrication of more sensitive microsensors, as the following examples might suggest. Xu and coworkers reported the fabrication of platinum microelectrodes modified with gold nanoparticles for the detection of Cu(II) with in situ microwave activation [41]. The group of R.G. Compton reported the use of a palladium nanoparticle array supported on boron doped diamond for the detection of hydrazine [42]. They used the catalytic properties of the metal to reduce the potential at which hydrazine oxidizes at carbon electrodes and showed improved limit of detection and sensitivity. Tsai et al. recently showed that platinum microelectrodes modified with gold nanoparticles and a self-assembled

monolayer of 3-mercaptopropionic acid are suitable for dopamine monitorization in the brain with higher sensitivity that Nafion coated MEs and limit of detection on the nanomolar range [43]. Ross and Venton recently published an improved version of Nafion coated carbon fibers by the addition of carbon nanotubes [44]. The resulting combination of the ion-selectivity of Nafion with the fast kinetics provided by CNTs was an improved microsensor for the detection of adenosine without the interference of adenosine triphosphate (ATP).

2.3. Common electrode materials

2.3.1. Platinum

Platinum is the most commonly used metallic electrode for voltammetric studies. It is a very ductile metal with the advantage of having a thermal expansion coefficient similar the soda-lime-silica glass which is commonly used for the insulation of Pt electrodes. This metal can provide an inert, stable electrode in both aqueous and nonaqueous solutions provided that complexing agents are not present in solution. However, because of its electrocatalytic activity towards hydrogen adsorption and evolution, the negative potential limit of platinum electrodes in protic solvents is very low. Towards positive potentials, in water or oxygen containing solvents there is formation of an oxide film yielding potentially interfering voltammetric waves. In fact, the true ideally polarizable electrode behavior is restricted to about 0.2-0.3 V according to the surface state and microstructure of the used metal [26,27].

2.3.2. Gold

Gold is another widely used electrode material. Of easy fabrication, these electrodes can exhibit a variety of geometries. One of the most interesting configurations is based on pure or transition metal-doped gold clusters. These assemblies of nanoparticles exhibit different properties from the bulk metal according to the particle size, geometry and/or added dopant. The use of gold, as well as platinum, is in part related to its electrocatalytic activity towards oxygen reduction.

Gold exhibits an overpotential for hydrogen evolution reaction between that of platinum and mercury. In alkaline media it has electrocatalytic activity towards oxidation of carbohidrates. However, at positive potentials, gold forms an oxide layer and will undergo dissolution in the presence of complexing anions such as chloride and cyanide [26,27] .

2.3.3. Mercury

Mercury is a liquid metal at room temperature which is convenient because it does not require any polishing or cleaning procedures. There are several configurations of mercury electrodes such as the hanging drop, the static drop or the controlled growth drop mercury electrodes. In opposition to platinum, mercury exhibits a large overpotential for hydrogen evolution and is therefore a very useful electrode for the study of cathodic processes. However, for positive potentials mercury is easily oxidized especially in the presence of complexing anions [26,27].

2.3.4. Carbon electrodes

2.3.4.1. Highly oriented pyrolytic graphite

Highly oriented pyrolytic graphite (HOPG) is a carbon material that is prepared by exposing pyrolytic graphite to conditions of high pressure and high temperature. Because of its smooth surface it is good for studying electrochemical reactions. In terms of electrical conductivity it is anisotropic presenting both metallic and semi-metallic conductivity depending on the direction. Its basal plane presents intrinsically low double-layer capacitance density of 1-5 $\mu F.cm^{-2}$ and consequently low background current. However, the more defective the basal plane is the more the double layer capacitance increases. Furthermore, the amount of exposed edge planes and carbon-oxygen functionalities also contribute for increasing the background current as well as the enabling of molecular adsorption. Hence, although it is a quite well known electrode material, its microstructure will define the overall electronic and electrochemical behavior [26,27].

2.3.4.2. Carbon fiber

Carbon fibers are commercially available in diameters from ca. 1 to 40 μm, which readily puts them in the microelectrode scale. They can be produced from several starting materials such as polyacrylonitrile (PAN) and pitch or from wood derivatives like rayon and lignin. Another route is by gas-phase deposition from a carbon precursor. As

microelectrodes they are usually given a cylinder or disk geometry with glass insulation. The variety of existing synthesis routes and heat treatment procedures yield fibers with different microstructure and consequently different properties. Likewise, HOPG, a more ordered graphitized fiber will tend to present lower capacitive current as well as lower content of surface oxygen groups which minimizes adsorption. Hence carbon fibers usually undergo surface pretreatments to optimize their properties, such as a few voltammetric cycles in 1 M HCl. After such conditioning procedures, background currents and adsorption effects are minimized, and electron transfer kinetics for most redox systems are enhanced [26,27].

2.3.4.3.   Carbon nanotubes

Carbon nanotubes are somewhat a maximization of basal planes order in carbon-related materials. As for carbon fibers, their high aspect ratio makes them easily suitable for producing microelectrodes. Of interest, CNTs generally present higher sensitivities, lower limits of detection, and faster electron transfer (ET) kinetics than more common carbon electrodes. The CNT detecting performance depends on the synthesis method and post-synthesis treatments. There are three main routes for CNT synthesis all advantageously assisted by metallic catalyst particles: arc discharge, laser ablation/vaporization, and chemical vapor deposition (CVD). By engineering the catalyst particles and regulating the growth conditions, single walled (SW) or multiwalled (MW) CNTs can be grown. The structure helicity (i.e. chirality) of SWCNTs will determine their electronic behavior from metallic to semiconducting. For MWCNTs, the metallic behavior of at least one of the layers makes the whole tube structure to behave as a metallic conductor. Besides their electronic properties, CNTs complement their potential as sensors by exhibiting high electrical conductivity, high chemical stability, high mechanical strength, and high appetence for surface functionalization [45,46].

However care must be taken as metals are used in their synthesis. Hence, after growth some harsh purification procedures are required, typically washing with acidic solutions, but still, it is not a totally efficient procedure with metal impurities remaining encapsulated inside the structures. Furthermore oxygen groups may be added to

exposed CNT edges or in-plane defects yielding the breakdown of the tubes and their shortening [45,46].

2.4. Diamond and boron doped diamond

2.4.1. The diamond structure

Diamond is one of the carbon allotropes, characterized by being bound to the orbitals of four other carbon atoms by means of strong covalent sp^3 bonds each with an energy of 370 kJ.mol^{-1}, forming a regular tetrahedron with equal angles of 109° 28' (Figure 2.3).

109° 28'
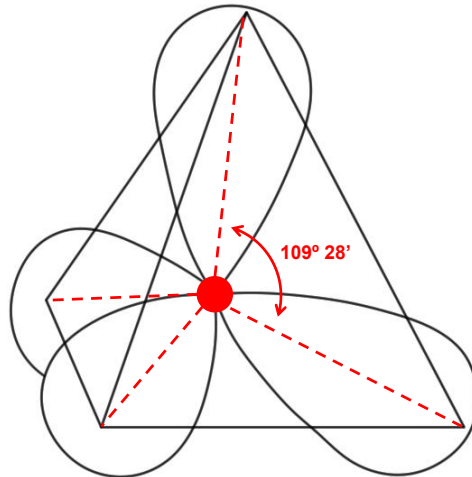
Figure 2.3 – The diamond tetrahedral structure. (adapted from [46])

The diamond crystal structure is the face centered cubic Bravais lattice with a lattice constant of a = 3.567 Å. Each lattice site is populated by two atoms in the positions [0, 0, 0] and [¼, ¼, ¼] within the cubic unit cell which altogether contains the equivalent to eight carbon atoms. The interatomic spacing is 1.54 Å, which is considerably small in comparison to other semiconducting materials (2.34 Å for Si). This close packing, optimum alignment and strong bonding make for the highest atomic density (1.76 x 10^{23} cm^{-3}) of any known solid [47].

This structure is among the stiffest, hardest and least compressible of all substances as well as one of the most chemically stable.

2.4.2. CVD diamond

Diamond obtained by chemical vapor deposition (CVD) is known as a very versatile material by exhibiting a combination of properties such as extreme hardness, highest thermal conductivity of any solid material as well highest dielectric strength (10^7 Vcm^{-1}), optical transparency from the UV to the far infrared, and extreme chemical inertness, among others [48]. Although owing most of these properties to the high stability and strength of its sp^3 bonded carbon tetrahedral coordination, CVD diamond is grown in metastable conditions, at sub-atmospheric pressures, by several techniques among which the hot filament chemical vapor deposition (HFCVD) is among the most commonly used ones [49]. By this technique, diamond films can be grown from thermally activated gas mixtures constituted of high hydrogen (~92-99.5%) and low carbon content hydrocarbons, usually methane (~0.5-20%) [50,51]. Besides methane and hydrogen, other gases such as O_2, CF_4, CCl_4, CO_2, Ar, etc. can be used [51–55]. The growth conditions for CVD diamond are confined to a very small region in the phase diagram of carbon (Figure 2.4).

Although graphite is thermodynamically the stable species, this growth process is kinetically controlled as hydrogen has the important role of etching away the graphite and other sp^2 bonded carbon phases, enabling the diamond deposition. Furthermore, hydrogen plays a fundamental role in the growth mechanism, being a central element in the so-called hydrogen abstraction reaction. This is the driving reaction behind diamond growth by HFCVD and consists basically on bonding of the methyl radicals, as building blocks to the formation of the C-C sp^3 bonded crystalline network (Figure 2.5) [56].
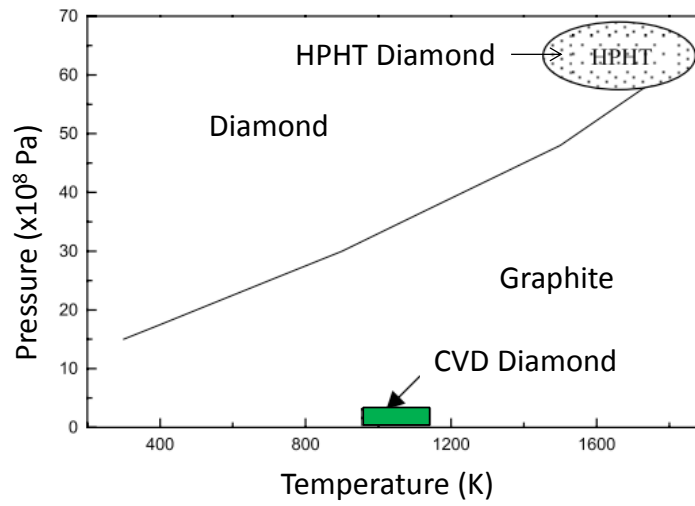
Figure 2.4 – Diamond phase diagram evidencing the CVD growth window (adapted from [57]).
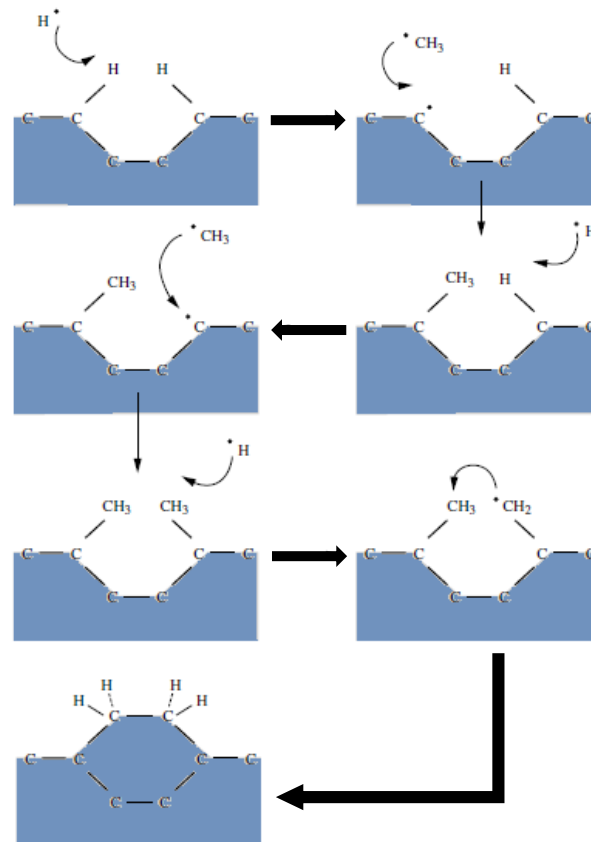
Figure 2.5 – CVD Diamond growth mechanism, evidencing the role of atomic hydrogen (adapted from [58]).

2.4.3. Diamond surfaces

In any electrochemical application, achieving a certain desired behavior is strongly connected with the surfaces and interfaces taking part in the process. Since these are end regions, in order to achieve energetic stability their structure and configuration are often different from that of the bulk material, giving rise to derivations from the intrinsic atomic arrangement of the material, a phenomenon called reconstruction. This truncation of the periodic arrangement of the crystal at the surface gives origin to distinct electronic states, the surface states. These are intrinsic to each material and specific to each crystallographic orientation [59].

The three main crystallographic orientations of diamond are (100) (110) and (111). For all three, the carbon dangling bonds consist of π-electron systems which induce different density of surface states, with topology dependence. Surface reconstruction on the (100) faces consists on the formation of symmetric dimers arranged in rows with a distance of 2.52 Å between them [60]. The dimmer orbits present a gap of 1.3 eV between occupied and unoccupied states, with the occupied states being energetically placed within the valence band. Therefore there is no charge exchange between surface states and the bulk, which implicates that no surface band bending occurs as well [60].

The (111) and (110) surfaces distinguish from (100) by the reconstruction arrangement of the dangling bounds, which form symmetric π-bonded chains but without dimerization. Therein (111) surfaces present a 2x1 reconstruction with a distance of 4.37 Å between the chains while (110) surfaces do not exhibit reconstruction and have a distance of 3.57 Å between chains [60].

2.4.4. Surface hydrogen terminations of diamond

As seen above, the surface atomic structure is normally observed in the form of a π-bonded array ensuring the normal valence. However, the reactivity of these unsaturated bonds together with the normally abundant atomic hydrogen used for CVD diamond growth, leads to the formation of strong C-H bonds and CVD diamond is normally terminated with chemisorbed hydrogen atoms, even though some residual and weakly

chemisorbed hydrocarbons can persist even after the full growth process is properly performed. Upon passivation with hydrogen the (111) and (110) surfaces suffer no reconstruction and present almost perfect bulk termination. For (100) faces single-bonded dimers are preserved forming the same geometry as for the clean reconstructed surface [59].

This surface character is quite stable, considering that temperatures of more than 800 °C in vacuum or inert atmosphere are needed if the hydrogen is to be desorbed and the reconstructed surface restored. In air or in solution there is a different situation. The H-terminated surface will remain relatively stable within a matter of a few days at room temperature, but increasing the timescale there is a clear tendency for surface oxidation in different forms such as ether and carbonyl groups or hydroxyl if there is significant moisture [61].

The same tendency can be verified during use. If diamond electrodes are submitted to strong polarization, i.e. near the anodic limit of the potential window, a replacement of hydrogen termination by oxygen functionalities is verified and the surface becomes much like as if it was submitted to an oxygen plasma [62,63].

2.4.4.1. Electron affinity and surface band bending

Surface band bending consists on a variation of the electrostatic potential which then involves all energy levels, the valence band maximum (VBM), conduction band maximum (CBM) and core level. This potential variation occurs in a direction perpendicular to the surface and originates from an exchange of free charge (electrons or electron holes) between the surface and the bulk motivated by the adjustment of the chemical potentials between the bulk material and the surface states (intrinsic surface states, defects, or adsorbates) [60]. The charge density profile is governed by the Fermi occupation function and charge neutrality condition described by Poisson's equation. For moderately doped diamond (10^{16} dopants/cm^3) the charge adjustment length corresponds to a fraction of a micrometer through which the space charge in the semiconductor is compensated by an equal amount of surface charge, which in turn depends on the two dimensional density of states (Figure 2.6).

31
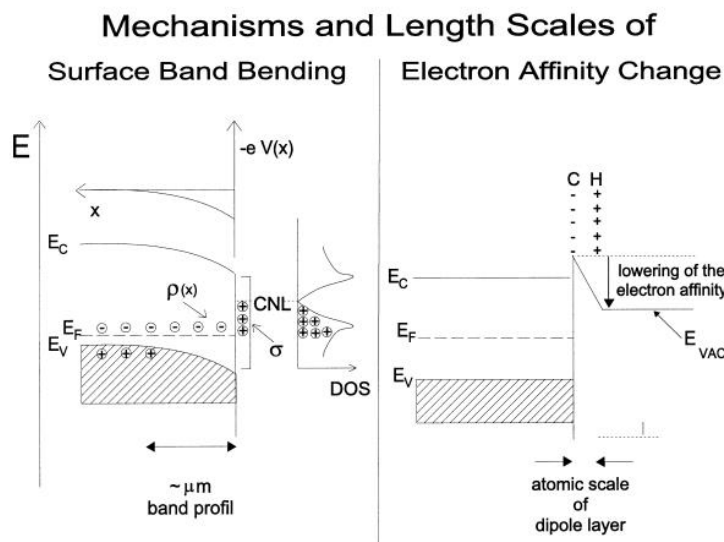
Figure 2.6 – Surface band bending of diamond (adapted from [60]).

2.4.4.2. Electron affinity

Chemisorption at terminating surface bonds commonly gives origin to heteropolar bonds. These will exhibit a dipole defined by the different electronegativities between the carbon atoms from the diamond lattice and the surface-terminating atoms [19]. Differently from typical semiconductor elements, the electronegativity of carbon is higher than that of hydrogen, its most common terminal species. This causes a reduction in electron affinity in comparison to clean surfaces making it effectively negative, as is schematically shown in Figure 2.7. The second most important diamond termination, oxygen, has the opposite effect since it exhibits larger electronegativity than carbon [61,64].
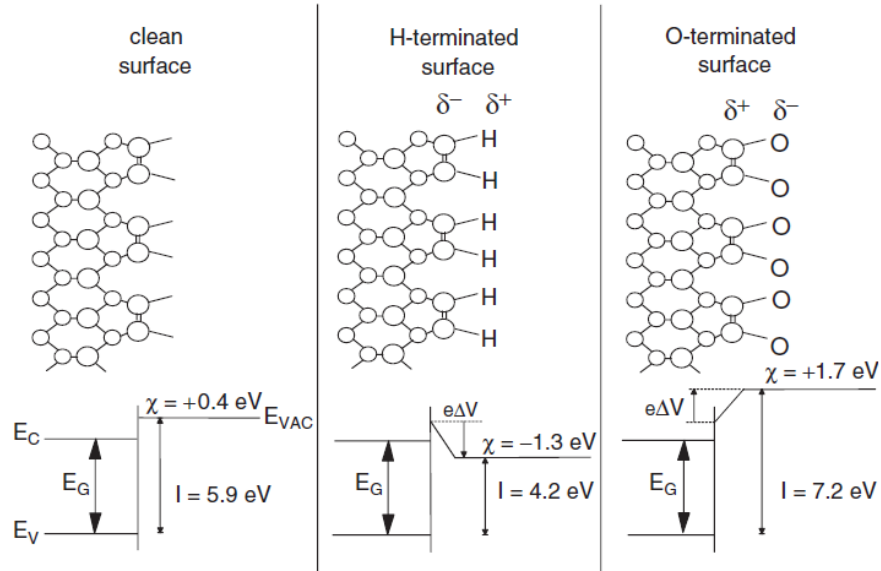
Figure 2.7 – Effect of varying the surface termination of diamond on the electron affinity. The energy diagrams originate from the different heteroatom terminations. The potential step eΔV reflects the variation imposed by the surface dipoles (adapted from [61]).

2.4.4.3. Surface conductivity of diamond

Given the wide band gap of diamond, this material would be expected to be a perfect insulator. However, in a work from 1989 Landstrass and Ravi [65] have observed that undoped diamond exhibits high conductance which progressively reduces upon annealing in vacuum. Although misinterpreted at the time, this phenomena was addressed by Maier et al. in 2000, who identified the importance of hydrogen surface termination and atmospheric adsorbates in the process [66]. Hydrogen termination of diamond has a double role. As carbon has higher electronegativity than hydrogen a surface dipole is generated upon hydrogen chemisorption leading to a negative electron affinity of -1.3 eV. In consequence, the usual large bandgap of 5.5 eV is lowered to 4.2 eV. A thin atmospheric adsorbate layer, as it forms naturally on all surfaces exposed to atmosphere, provides a system that can extract electrons from diamond as long as the electron affinity of the physisorbed species approaches the referred 4.2 eV ionization energy. This is precisely the case considering typical atmospheric conditions with a pH of between 5 and 7, yielding a chemical potential for the atmospheric layer of -4.2 to -4.3 eV, thus slightly lower than the valence band maximum (VBM) [61].

The trigger mechanism for charge transfer is the redox reaction of hydronium conversion to hydrogen. After reaching chemical equilibrium between diamond and the adsorbate system, an upward band bending is caused by the energy leveling between the positive layer of holes and an equal amount of anions from the atmospheric layer (HCO_3^-), confining the holes close to the surface and pinning the Fermi level below the valence band maximum explaining the surface conductivity of diamond [61].

Accounting for partial surface oxidation and the effect of water dipoles in the ionization energy, different couples other than H_3O^+/H_2 have been considered that can sustain the airborne surface conductivity such as $O_3/O_2 + OH^-$ and O_2/OH^-. Given the limited thermal stability of these species, other molecules were studied such as fullerene (C_{60}) and fluorofullerenes, which provided clearer understanding on how surface conductivity depends only upon the energy difference between the VBM of hydrogen-terminated diamond, and the lowest unoccupied molecular orbit (LUMO) of the molecular adlayer. Hence, the properties of the diamond surface can be totally commuted by hydrogen chemisorption, presenting the lowest ionization potential among all semiconductors in spite of its large band-gap (Figure 2.8) [61].
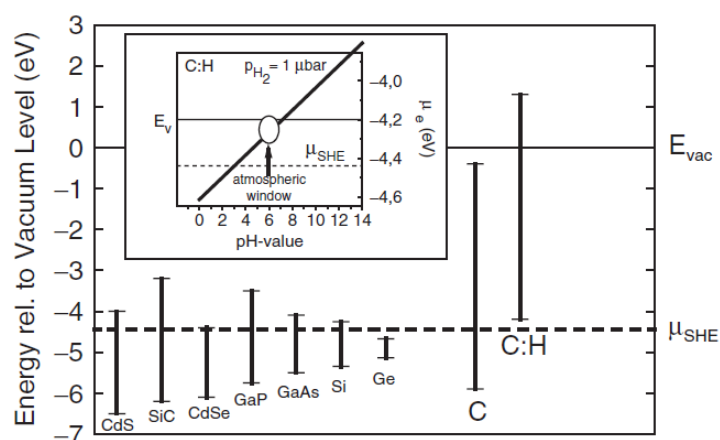
Figure 2.8 – Comparison between band gaps and edge energies of different semiconductor materials including bare and H-terminated diamond. The valence band maximum of H-terminated diamond is located within the chemical potential window of the hydronium-redox couple (inset), enabling electron transfer to occur. μ_{SHE} is the electrochemical potential of the standard hydrogen electrode and E_V is the valence band edge of hydrogenated diamond (adapted from [61]).

In fact, hydrogen is an example of what comes to be one of the most important characteristics of this material, the multiple application possibilities only by means of adequate functionalization. If displaying oxygen terminations instead of hydrogen, diamond will present a positive electron affinity of 1.7 eV, meaning a remarkable 3 eV shift in electron affinity, along with loss of surface conductivity and gain of hydrophilic character, just by using a different heteroatom. Others such as -F, -OH, -NH, -Cl have been reported [67–69].

2.4.5. Doping of diamond

The usual insulating character of diamond can be inverted by doping the carbon network with other atomic species enabling the growth of CVD diamond films with controlled properties, from p- or n- type semiconductivity to metallic conduction. The main efforts in this area have been made towards doping diamond with elements such as boron, nitrogen, phosphorus and sulfur, even though attempts with other less suitable species have been reported [70].

While p-type doping of diamond is well established, n-type doping of diamond is hard to achieve [71]. From group V elements, many options have been attempted, mainly with nitrogen and phosphorus. Nitrogen has an atomic radius close to carbon and can be easily integrated as a substitutional donor in the diamond lattice. It is however a deep donor with an energy of 1.7 eV below the conduction band making it unsuitable for semiconductor devices. Phosphorus is also a deep donor but with a much lower energy than nitrogen, 0.6 eV. Yet it has a large covalent radius in comparison to carbon and its uptake in diamond is in a highly non-equilibrium state, with very low doping efficiency, especially in the tight (100) lattice. For the (111) orientation, doping levels between 10^{16} and 10^{20} have been achieved [61,72,73]. Furthermore hydrogen passivation is a further complication, as it is for other dopants. Although not fully understood or sufficiently consistent, doping by phosphorus is currently the most valid and successful route for gathering n-type semiconductivity of diamond [74].

More complex solutions have been considered as are the cases of sulfur and a boron–deuterium complex, which yield n-type conduction with shallow donor levels of 0.38 eV and 0.23 eV, respectively, but there is a lack of reproducibility [61].

Conversely p-type diamond is well studied and applied. Boron, with a covalent radius of 0.88 Å, similar to carbon with its 0.77 Å is easily incorporated in substitutional sites of the diamond lattice. It has a shallow acceptor level of 0.37 eV above the valence band (Figure 2.9), although this energy becomes lower with impurity band formation at higher boron concentrations [75,76]. There are a number of boron containing precursors such as diborane, trimethylborane, triethylborane, boron trioxide, boric acid and others [50,77].

Besides the role as boron source, the impact of adding boron compounds to the normal C/H gas compostion of diamond has been studied, although the observations are strictly dependent on the deposition method and the composition of the doping compounds [78].

Theoretical studies and experimental studies indicate that the growth rate of boron doped diamond can vary in function of the type of boron precursor and its concentration, which is also true for the doping efficiency. The formation of boron-hydrogen compounds like BH_3, BH_2, and BH induces a variation in the concentration of important radicals for diamond formation such as atomic hydrogen and CH_3, thereby usually diminishing the deposition rate [78–80]. There are also consequences for the crystalline quality of the films, which have been reported to exhibit considerable amorphization with increasing fractions of sp^2 carbon associated [77]. In contrast, other authors disagree reporting improved crystalline quality for boron doped diamond films [81].

The relationship between the B/C ratio of the gas phase and that of the crystalline network of the diamond films is, again, not straightforward. The variation is usually not linear and relationships of the boron concentration in the films varying with the square of the boron concentration in the gas phase have been measured by reference authors [78]. Other relationships include maximum doping effectiveness at a B/C ratio of about 10000 ppm in the gas phase [82,83].

The contradictory findings concerning some observations related to boron doping can be sustained by some of the variables involving the growth of boron doped CVD

diamond: (i) HFCVD and microwave plasma assisted CVD (MPCVD) are the most common growth techniques and the carbon radicals leading to diamond growth are partially different for both [49,84]: (ii) the reactor geometry (e.g. disposition of gas inlets and outlets) determines the gas distribution profile and ultimately the homogeneity of the diamond films [85–87] (iii) diborane gas (B_2H_6) is without doubt the simplest, most efficient boron precursor available (only B and H), but it is also extremely toxic and explosive, which leads to different precursor choices for many laboratories [88]; (iv) the other available precursors frequently contain oxygen, which has a strong influence in the CVD process and in the final properties of the diamond films [89,90].

Although a general trend can be reached, the above mentioned factors will dictate the reproducibility of observations between research groups and the probability of success of a given diamond based device.

2.4.5.1.   Conductivity mechanisms in boron doped diamond

The conductivity of boron doped diamond has been ascribed to two different models. One model describes electron transfer as occurring via impurity states within the band gap of diamond. These are associated to overlapping wave functions of neighboring boron atoms. Hence, with a high enough density of states impurity bands will form (Figure 2.9). The rate of electron transfer will depend on the density of states with a corresponding energy in relation to the potential of the redox couple of interest. Lattice hydrogen is also believed to contribute to the impurity bands. This is because surface states are considered to be defects or impurity spots at the surface or near surface. Therein, boron, hydrogen, oxygen or carbon inclusions may be responsible for mediating electron transfer between the valence band and the target redox system. The mechanism *per se* is believed to consist on multiple electron hopping and the heterogeneous kinetics are dependent on the rate of tunneling of electrons and holes to the redox species. The available density of states will depend on the dopant concentration, which controls the rate of carrier migration and, consequently, the rate of electron transfer is also directly related with it. Excessive impurity concentration can lead to carrier scattering and therefore lower the mobility [91].
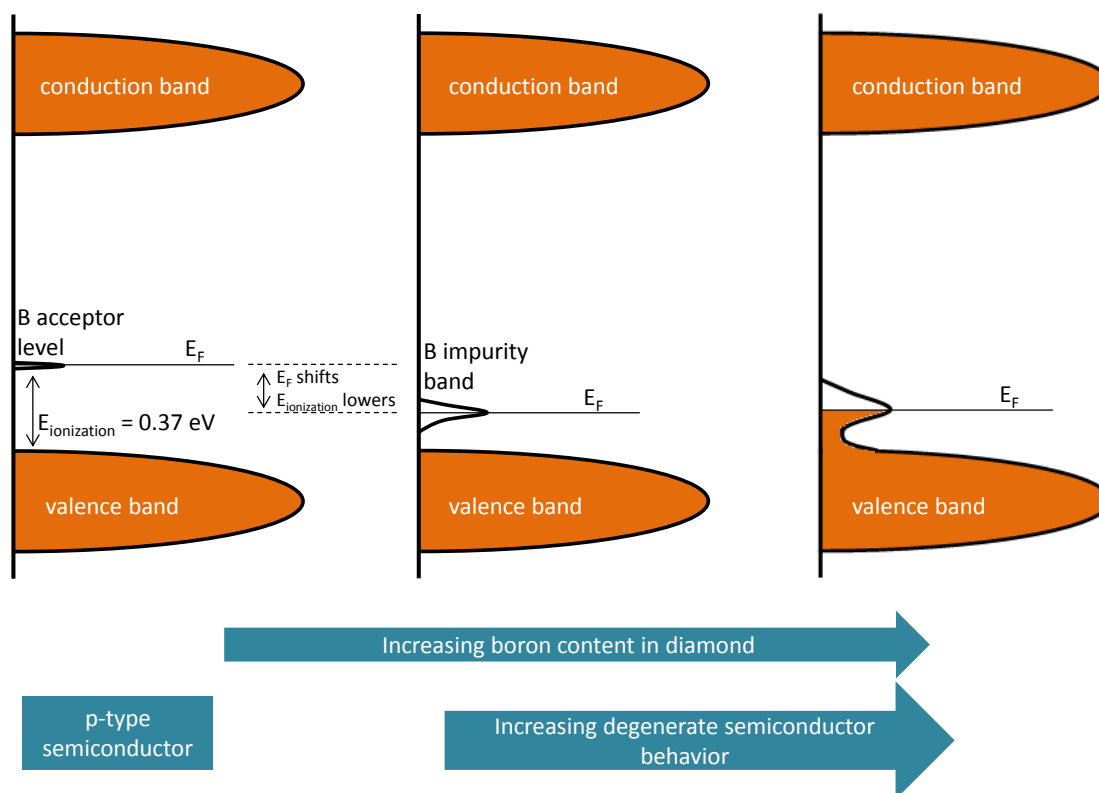
Figure 2.9 - Boron acceptor level in the diamond bandgap and effect of boron concentration. (adapted from [92])

A second model adopts a perspective which describes the boron doped diamond surface as having non-uniform boron dopant distribution. Hence there will be sites exhibiting fast heterogeneous electron transfer and others exhibiting slow transfer, depending on the dopant concentration. This is in agreement with the different capability for boron uptake of each crystal orientation: the (111) and (110) planes can accommodate about five to ten times more boron than the (100) (this topic is further discussed in section 2.5.2). Discontinuity sites like grain boundaries and edges are also believed to uptake high dopant concentrations that do not contribute for conductivity. The result of this is that electron transfer rate will be heterogeneously distributed along the surface and its magnitude given by the average of the whole surface.

Hence, this alternative model is focused on the availability of active sites with sufficient dopant concentration providing for electron transfer, rather than on carrier migration [91].

The seemingly simple substitution of an atom with valence of 4 by an atom of valence of 3, with generation of an electronic hole that enables charge mobility can, however, be quite complex. The interaction of boron, carbon and hydrogen in a polycrystalline matrix has been studied both in theory and practice. The thermodynamic stability of boron in diamond, the formation of complexes besides simple C-B bonding, as well as compensating effects are central issues in understanding boron doped diamond [93–95].

Compensation arises from the presence of defects and residual impurities. It consists on the trapping of electrons or holes by those impurities, thereby reducing the free carrier concentration. Minimization of compensating defects is therefore a major issue concerning the achievement of reasonable carrier densities, especially when considering that only a fraction of the dopant is thermally activated at room temperature [96]. Other important consequence of high impurity concentration is the reduction of carrier mobility by ionized-impurity scattering [97].

2.5. Diamond electrochemistry

The application of diamond films for electrochemical purposes dates back to 1987 by Pleskov and co-workers [98]. By heavily doping this material it can become a degenerate semiconductor and exhibit a metal-like behavior [99]. Perhaps the most remarkable property of diamond electrodes is the extremely wide potential window of water stability, of 3 V or more, which is larger than for any other material [70] (Figure 2.10). Its background current is also remarkable being lower than that of other well established and widely used carbon electrodes (HOPG, glassy carbon, etc.) [100].

The amplitude of its potential window is intimately related with its normal hydrogen surface termination. Hydrogen and oxygen evolution resulting from the decomposition of water are known to depend on the adsorption of intermediates, which is not favorable to occur on diamond surfaces. Hence, very high overvoltages are required to drive the water electrolysis, which is quite useful for studying reactions occurring at potentials within this potential window [101].
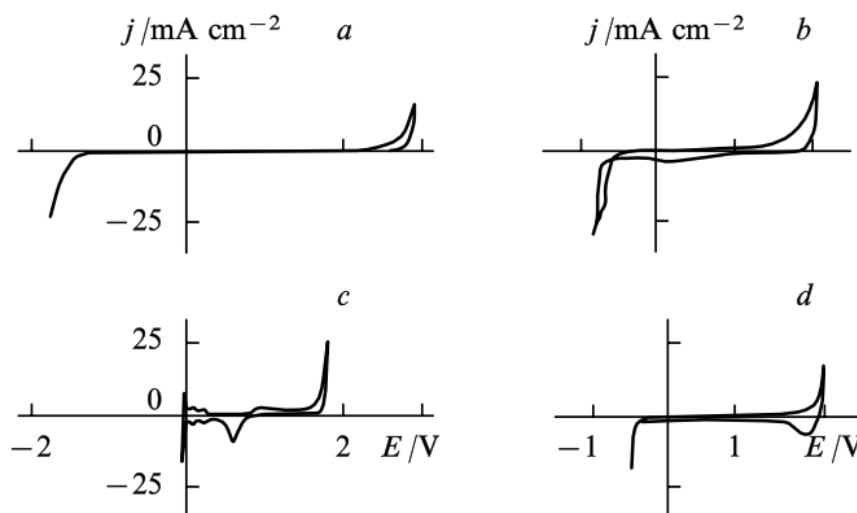
Figure 2.10 – Polarization curves of a) good quality diamond; b) low quality diamond; c) platinum; and d) HOPG in 0.5 M H_2SO_4. (adapted from [102])

Like for water electrolysis, the surface termination will dictate, as well, the electrode kinetics for driving other reactions. Oxygen terminations, among many others, are also

possible in diamond and have a dramatic impact on the behavior of diamond electrodes, especially because the surface becomes hydrophilic.

Another feature of diamond is its high resistance to corrosion, even in polarization for extensive periods in solutions of 1 M HNO_3+0.1 M HF or 1 M HNO_3+2 M NaCl, between the potentials of hydrogen and oxygen evolution, showing absence of microstructural degradation. The same is not true for other carbon electrodes under the same conditions [101].

2.5.1. The influence of diamond semiconductor nature

Considering an "ideal" semiconductor electrode, the potential drop observed in the Helmholtz layer at interfaces is smaller than that observed in the space-charge layer of the bulk material. This means that the valence band maximum and conduction band minimum energy edges are "pinned" at the surface and the surface free carrier concentration is independent of the doping level. In the same way the electron transfer kinetics are also independent of doping [101]. This effect is not observed in diamond. The potential distribution at the diamond/electrolyte interface depends on the doping level, and in the same way the rate of electron transfer is also proportional to the dopant concentration.

The redox kinetics are also dependent on the equilibrium potentials of redox couples, and it was observed that the higher their energy in the gap, the more irreversible the reaction becomes on diamond electrodes. The correspondence between physical electronic energies and electrode potential is given by $eE = 4.44 + \varepsilon$, where e is the electron charge, E is the electrode potential in V vs the standard hydrogen electrode (SHE), and ε is the electrochemical potential in eV. This is the equivalent to saying that redox couples with more negative potentials have higher energies at which there is a lack of charge carriers in diamond, and the corresponding redox reactions will behave more irreversibly. This effect is more pronounced the lower the doping level of diamond [83,101].

2.5.2. The influence of the crystallographic orientation and surface morphology

The incorporation of impurities, such as boron atoms by doping, does not proceed equally for each of the three main crystallographic orientations of diamond. It has been demonstrated, by growing diamond films with specific orientation that the reversibility of redox reactions is strongly conditioned by the crystallographic nature. The (111) and (110) planes can accommodate boron more easily and, thus (100) planes grown and doped in the same conditions tend to exhibit boron concentrations one order of magnitude lower. In a study performed by Pleskov et al. [103], with the $[Ru(NH_3)_6]^{2+/3+}$ and $[Fe(CN)_6]^{3-/4-}$ redox couples, shown in Figure 2.11 it can be observed that for the (111) and (110) diamond orientations, although the oxidation and reduction reactions proceed irreversibly, the anodic and cathodic peaks are well distinguishable and mirror each other, whereas for the (100) diamond the peaks are barely observable. Comparing the charge transfer coefficients for the anodic and cathodic reactions, α and β, respectively (recalling that they correlate the variation in barrier height for electron transfer with the variation in potential), it was verified that the (111) planes exhibit values of 0.40 for α and 0.44 for β, similarly to a metal, whereas the coefficients for (110) planes were closer to that of a semiconductor (0.2 and 0.23). This means that both redox reactions will proceed with decreasing delay by the following diamond crystal orientation order: (111)>(110)>(100) [101].

The same trend was observed for single crystal deposition, which confirms that the diamond growth habit is determinant in the incorporation of boron into substitutional carbon sites, consequently influencing the overall electrochemical behavior of single and polycrystalline diamond.

The same group presented a study [104] on the influence of the surface roughness of diamond, and showed that it is also influential on the progress of redox reactions. Experimentally, the study was performed by growing diamond on top of titanium substrates with different roughness, which yielded the corresponding roughness for the diamond films on top. It was shown that for polycrystalline diamond films with higher roughness, the charge transfer when using the $[Fe(CN)_6]^{3-/4-}$ couple is improved and the

43

redox reaction will consequently proceed with lower ΔE_p (anodic to cathodic peak separation), i.e. more reversibly. Furthermore the films grown with higher roughness showed increased mechanical stability and lower background current [101].
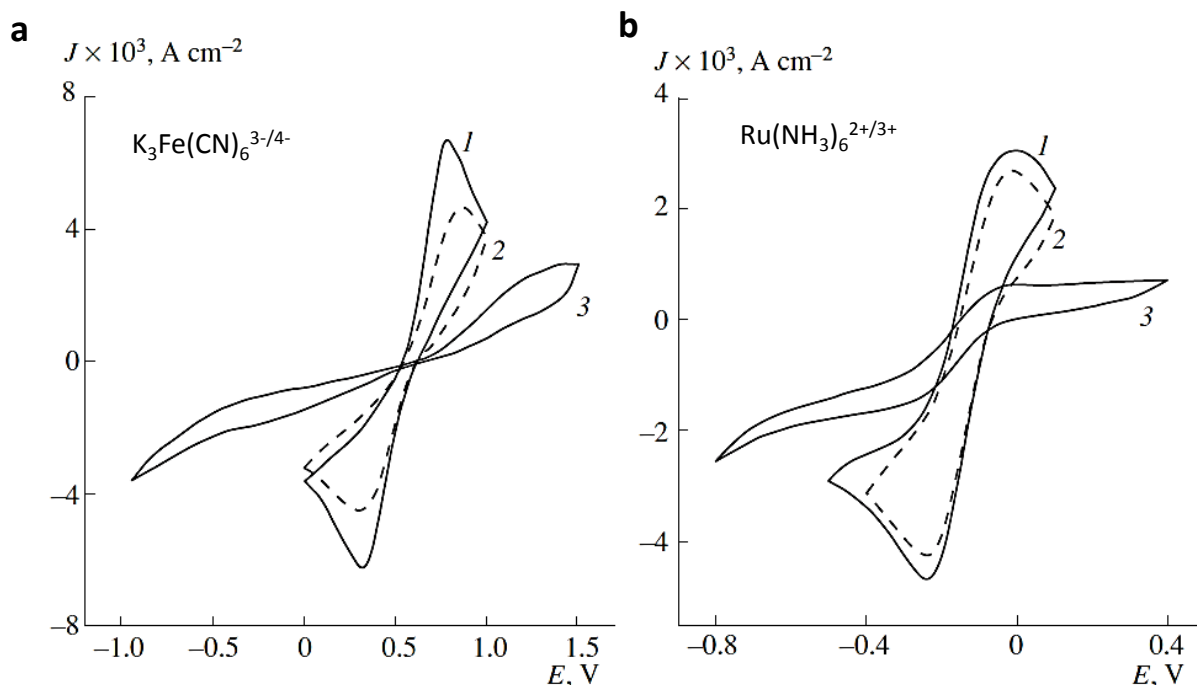
Figure 2.11 – Cyclic voltammetry with single crystal diamond grown with different orientations in a) 10 mM $K_3Fe(CN)_6$ + 10 mM $K_4Fe(CN)_6$ in 2.5 M H_2SO_4 and b) 5 mM $Ru(NH_3)_6Cl_2$ + 5 mM $Ru(NH_3)_6Cl_3$ in 100 mM NaCl. (adapted from [103]).

2.5.3. The influence of film thickness, grain size and sp^2 content

It has been suggested that the electrochemical behavior of diamond thin films is different for films with varying grain size and thickness. The reason for this is, simultaneously related to the amount of exposed sp^2 carbon material, which tends to be higher for smaller grain size and thinner diamond films. In solutions containing the $[Fe(CN)_6]^{3-/4-}$ couple, higher transfer coefficients were determined for films smaller crystallite size and lower thickness. Higher differential capacitance was also observed [71].

Similar results have been demonstrated by Duo et al. [105], by testing diamond-graphite composite electrodes with sp^2 impurity dispersions on top of polycrystalline diamond

films. The redox couples 1,4-benzoquinone/hydroquinone and $[Fe(CN)_6]^{3-/4-}$ were used to show that in cyclic voltammetry experiments, the electrodes with higher sp^2 content showed a more reversible behavior, indicating sp^2 phases as a major path for charge transfer [105].

Contrasting information was gathered in a recent study using field emission scanning electron microscopy (FE-SEM) and intermittent contact scanning electrochemical microscopy (IC)-SECM to study the electrochemical behavior of polycrystalline boron doped diamond films towards the redox couples $FcTMA^{2+/+}$ (ferrocenylmethyl trimethyl-ammonium) and $Ru(NH_3)_6^{3+/2+}$. In this study it was demonstrated that the electron transfer coefficient, k_0, is related to the local density of states in the diamond crystals, which is regulated by the boron concentration. Furthermore it was clarified that heterogeneous electron transfer activity does not depend on excess boron or sp^2 carbon in the grain boundaries [106].

2.5.4. The influence of surface termination

2.5.4.1. Oxygen terminated diamond

After hydrogen termination, carbon-oxygen groups are the most commonly found in diamond films, most probably because they are very stable and are the outcome of exposure to atmospheric oxidizing conditions.

Structurally speaking, the divalence of oxygen can make two C-O covalent bonds with half the atomic density of hydrogen at (100) the faces. This minimizes the steric restraints and no reconstruction is necessary, although at high temperatures with strongly oxidizing conditions the surface becomes unstable and disordered. Two bonding configurations have been proposed: (i) the top-site model with one oxygen double bonded to each surface carbon, and (ii) the bridge-site model with two single oxygen bonds connecting adjacent surface carbon atoms [59].

At the (111) surfaces oxygen can chemisorb both the clean and hydrogenated configuration and bonding occurs maintaining the geometry of the clean surface.

In order to correctly interpret electrochemical results, an overall balance regarding the surface condition prior to oxygen bonding, and also of the used oxidation method is

needed [59]. The electronic structure of oxidized diamond differs considerably from the hydrogenated one. Its positive electron affinity of 1.7 eV yields an ionization potential of 7.2 eV suppressing the surface conductivity observed at hydrogenated diamond. Conversely the surface becomes hydrophilic which represents a significant impact in the electrochemical behavior although with dependence upon the oxidation method [61].

The most common approaches for diamond oxidation are anodic polarization in strong acid and exposure to oxygen plasma. Both can yield differently bonded oxygenated structures affecting mainly selectivity and the kinetic constant towards certain redox species [68,107,108]. Surface oxidation influences the heterogeneous electron transfer kinetics, making it more sluggish for some redox species, whereas for others it is enhanced. A fair example comes from the detection of dopamine in the presence of excess ascorbic acid, for which the oxidation wave for dopamine is less than 100 mV below that of ascorbic acid when using H-terminated diamond [109]. Upon anodic oxidation of the surface, it is found that the ascorbic-acid signal is shifted to much higher positive potentials than dopamine, evidencing an enhancement in selectivity that can arise from surface oxidation treatment [107,109]. Sensitivity to pH is another characteristic that will be discussed in this document and was only verified after plasma oxidation of H-terminated diamond in the present work.

2.5.4.2. Fluorine terminated diamond

Fluorine presents the highest electronegativity among all elements. Upon submitting diamond to fluorination treatments its electrochemical behavior is substantially different from hydrogenated or oxygen terminated diamond. For example it opens the possibility of extending the working potential window from 3 to 5 V [110]. Contrary to hydrophilic oxygenated diamond surfaces, the chemical bonding and rearrangement induced by fluorine on the diamond network determines that it becomes strongly hydrophobic [110–112].

An early work by Freedman [113] on fluorine chemisorption on diamond by the use of an atomic beam reports it causes opening of carbon dimer bonds and surface reconstruction. Furthermore, the tight (100) diamond lattice surface would be disordered upon fluorination. Such hindrance was predicted not to be present in (111) surfaces

which would be partially reconstructed to the bulk-like arrangement. Also reported was a coverage lower than for hydrogen on both (100) and (111) surfaces and lack of thermal stability [113].

Different conclusions were drawn in later simulation studies by Tiwari et al. who determined that fluorine can provide a 100% coverage being energetically stable for the main diamond surface orientations with thermal stability at high temperatures [114]. Hadenfeldt et al. [115] have confirmed these predictions experimentally along with the enhancement of halogen chemisorption to hydrogenated diamond surfaces in comparison to the clean state. In their detailed study from 2001 [116] Kealey et al., accounted for the diverse microstructural sites of polycrystalline diamond putting in evidence the steric limitations of fluorine bonding to diamond carbon and determined that in discontinuity regions like edges and boundaries the formation of CF_2, and possibly CF_3 surface groups is more favorable, while C-F bonds have higher thermodynamic stability at diamond crystal faces.

Ferro et al. [117] verified that boron doped diamond films submitted to CF_4 plasma exhibit both a surface and sub-surface fluorinated structure and hypothesized that surface layer rearrangement can follow the initial chemical modification. They achieved the same results even from direct growth of fluorinated diamond, with even further in depth fluorine penetration, of tenths on nm, elucidating that this can provide higher stability in comparison to purely surface modified films. Although available information is somewhat inconsistent this probably derives from the various fluorination methods available. Fluorinated diamond can inclusively be grown directly by CF_4 introduction in the gas chemistry.

Electrochemically speaking, an extension of the already great quasi-ideal polarization window is consistently the main reported effect of diamond fluorination, which was attributed to the poor interaction between adsorbed intermediates at the fluorinated diamond interface. An evaluation of the extent of this hydrophobic nature was presented by Karlsson et al. [112] by submitting textured micro- and nanocrystalline diamond films to a C_4F_8/SF_6/Ar plasma treatment. They measured contact angles of the order of 160º, confirming the possibility of producing superhydrophobic diamond surfaces.

Another so far universal observation on fluorinated diamond electrodes is their slow kinetic response. In comparison to as-grown, H- terminated diamond, the kinetic constant, k_0, is lower by one order of magnitude for the Eu^{3+}/Eu^{2+} and Fe^{3+}/Fe^{2+} redox couples and by three orders of magnitude for the more surface sensitive $Fe[CN]_6^{3-}/Fe[CN]_6^{4-}$ [117]. Given its hydrophobicity and poor interaction of F-terminated diamond towards hydrogen and hydroxyl radicals, a scarce interaction with water is obviously implied.

This repulsion from the surface probably results in more compact arrangement of the solvation layer around the species of interest leading to a decrease in electron transfer rates, further determined by the molecular structure of each redox analyte.

The stability of C-F bond and the sub-surface depth profile of fluorinated diamond support the idea that it can present long term stability, longer life service under extreme polarization, possibly showing adequacy for processes such as electrosynthesis [67].

2.6.　　Applications of diamond microelectrodes

Although the use of diamond electrodes for electrochemical applications has become increasingly attractive in the last two decades, their first use in the form of microelectrodes dates to 1998 by Cooper and co-workers [118]. Back then, diamond was grown by microwave plasma assisted chemical vapor deposition (MPCVD) on top of tungsten wires. After insulation in glass capillary the microelectrodes where tested by cyclic voltammetry with 1 mM ferrocene in acetonitrile, showing a steady state current behavior with a scan rate of 10 mV/s and good reversibility. The water stability window was held from -1.8 to 1.4 V.

This pioneer work was followed by others of greater complexity, mainly focused on biological research. By these days, a search under the title words "diamond" and "microelectrode" done on one of the largest scientific search engines will retrieve 62 results. This is an average of less than 4 papers per year from 1998 until 2014. The most probable reason for this is the difficulty and skill required to fabricate and manipulate microelectrodes. Indeed, there are not many groups around the world reporting work on the subject.

The group of G.M. Swain is probably the leader in this area, with an extensive work on the detection of catecholamines, such as norepinephrine or epinephrine, important neurotransmitters and regulators of other physiological processes [119]. Their monitoring in tissues and body fluids can be very important in fighting Parkinson's disease and requires equipment of high sensitiveness and the use of reliable analytical techniques [120]. By continuous amperometry this group has reported the detection of substances such as: norepinephrine (NE), the principal neurotransmitter released from sympathetic nerves; serotonin (5-HT), a signaling molecule in the gastrointestinal tract; nitric oxide (NO), a gaseous signaling molecule and an inhibitory neurotransmitter responsible for the relaxation of muscles in the gut; histamine, a biogenic amine involved in immune responses and regulation of physiological functions in the gut, which acts as a neurotransmitter. By using fast scan voltammetry with diamond microelectrodes this group has also reported the detection of adenosine and serotonin (5-HT) [121]. Other reports include the detection of chlorinated phenols (water

pollutants) by capillary electrophoresis [122]. Good performance was shown by a diamond microelectrode without electrode fouling.

A recent review by Luong et al. [123], includes a compilation of the many analytes detected by diamond macro and microelectrodes. Ions such as sulfide [124] and arseneite (III) [125] have been analyzed with detection limits of 23 μM and 0.5 ppb, respectively. In the former case an array was used, while for As(III) the diamond microelectrode was modified with platinum nanoparticles. The identification of adenosine was reported by Martin et al. with a detection limit of 10 nM [126]. Measurements in vivo have been reported with diamond microelectrodes being used for detecting histamine [127] and dopamine [128] with sensitive and stable response. Application of these probes has also been done in scanning electrochemical microscopy (SECM) measurements for imaging the activity of the bacteria *E. coli* [129].

A very recent report from Fierro et al. [130] demonstrates in vitro and in vivo detection of the reduced form of glutathione (GSH) by cyclic voltammetry and amperometry measurements. GSH is an indicator of oxidative stress in cells and exists in high concentration in cancerous tissues.

Other interesting approaches to the use of diamond microelectrodes include the fabrication of diamond AFM-SECM probes for electrochemical studies and local imaging [131].

In our group research is being conducted to develop new diamond based solutions that allow the study of corrosion related processes. Good results have been gathered for the measurement of oxygen and pH with diamond microprobes, and the results are part of this work. The detection of metal ions such as Zn^{2+} has been achieved, although without enough reproducibility. Nevertheless they were also included in this document as a promising topic for future development.

3. Fabrication of diamond microelectrodes

3.1. Microelectrode fabrication

The use of microelectrodes was pioneered by plant physiologists more than 60 years ago [5]. Only later, in the 1980's, they were adopted by electrochemists mostly by the hands of Wightman [132] and Fleischmann [133]. Increased mass transport rates, reduced double layer capacitance, minimal ohmic losses and the possibility of measurements in high resistivity media are some of the reasons that motivated increasing numbers of fabrication techniques of both single microelectrodes and arrays. Furthermore their small dimension allows working in the steady-state, i.e., the electrolysis rate and the rate at which molecules diffuse to the electrode are equal. Consequently the steady-state limiting current is directly proportional to the analyte concentration, which simplifies the theoretical treatment for a number of electrode geometries, above such as the spherical, hemispherical, inlaid disks, inlaid rings, inlaid ring-disks and conical probes, as seen in Chapter 2.2 (Figure 2.2) [9]. Several other geometries have been used but either they only allow reaching a quasi-steady state or they have only one small dimension as can be the case with band microelectrodes [134].

The fabrication of individual microelectrodes can follow different routes, which usually require skilled operators and it is frequent to find simpler methods for producing an entire array than a single probe. The following examples describe some of the most commonly used procedures for microelectrode fabrication.

3.1.1. Practical aspects of fabrication

When the size of a wire or fiber drops below 10 µm, the sealing step becomes less straightforward and the quality of the bond between electrode and insulator becomes crucial. One hundred percent success rate for ME fabrication is usually never expected or achieved whether using traditional fabrication methods or more high-tech devoted ones such as micro and nanolithography patterning [135].

The construction of a microelectrode and the choice for its geometry depends on its intended use. This in turn will define: i) the size tolerable for application; ii) the electrode material; iii) the compatibility of the insulating shroud or support with respect to the

electrode material and the stability of the insulator in the electrolyte; iv) the necessity or ability to reproducibly clean the electrode surface; v) the possibility of obtaining rigorous theoretical treatment of current potential curves for a given electrode geometry; vi) the molecular turnover required; vii) the need or desire for a technically simple method of construction [135].

The actual size of a ME can be important simply because not all MEs as assembled are small. A disk of 1 µm in diameter can be surrounded by 1-2 mm of glass or epoxy shroud. A band or line electrode may have a submicrometer width, yet be centimeters long and surrounded by several square centimeters of insulator. Specifying a characteristic dimension of the ME clarifies this point. The characteristic dimension refers to the width of exposed electrode material and typically is used in quantitative or approximate treatments of the current response of the ME [135].

3.1.2. Fabrication approaches for some common microelectrode geometries

3.1.2.1. Hemispherical and spherical MEs

The hemispherical geometry is generally achieved by using mercury drops as the electroactive material. Mercury cannot, however, be deposited on every type of surface and iridium is generally the best available substrate for wetting. Platinum and carbon are alternatives, although not as good. Hence, mercury is reduced on the disk shaped tip of a wire, and the size of the growing hemisphere can be calculated by monitoring current and time or by direct observation on the optical microscope [9].

Spherical MEs usually consist of particle agglomerates. A common procedure is to promote the self-assembly of gold nanoparticles agglomerates. The process is mediated by the crosslinking agent, 1,9- nonanedithiol, at the tip of a glass micropipette coated with conductive carbon on the inside. Upon immersing the micropipette in the solution containing the gold particles, the cross-linking agent induces the formation of smooth agglomerates with the same properties of metallic gold [9].

3.1.2.2. Ring microelectrodes

Assemblies with this geometry are among the simplest to fabricate. Usually the idea is to coat an insulating rod with a conductive layer and an insulating layer on top. Or inversely, to coat the inside of a capillary or other hollow structure with a conductive layer and filling the remaining volume in the center with an insulating material such as a resin. In both cases the final ring microelectrode can easily be exposed by a polishing or cutting procedure [9].

3.1.2.3. Conical microelectrodes

The fabrication of conical microelectrodes has usually its root in electrochemical etching of a metal wire. It roughly consists in immersing the wire (anode) in an electrolyte solution along with a counter-electrode, and applying a sufficiently high potential to the cell causing the desired wire to anodically dissolve and thus acquire a pointed shape. Metals like Pt, Ir, Pt-Ir, Au, Ag and tungsten (W) are usually elected for sharpening. Different electrolytic solutions such as concentrated $NaNO_2$, NaCN and NaOH can be used depending on the used metal wire [136,137]. The most widespread procedure can be described by centering a tungsten wire (anode) inside a platinum ring (cathode) [138]. The apparatus can be inside an electrolytic bath or can solely present a thin lamellae of etching solution supported by the platinum ring, usually of NaOH or KOH. By applying a few volts during some minutes the tungsten wire will be sharpened dropping off the portion of wire bellow the plane of the platinum ring containing the solution.

3.1.3. Insulation methods

After choosing the geometry of an electrode material the conductor must be transformed into a working representation of the geometry. To be useful the very small must be connected to the macroscopic world for ease of handling and to make electrical contact. So, almost all electrode MEs are supported on, or shrouded within an insulating material. Interfacial problems often arise between the conductor and the insulator that must be minimized for successful electrode performance. While this is true for shrouded

or supported electrodes of any size, compatibility between electrode and insulator is also critical [135]. The insulation step tends to be a bit more complicated. One approach is to insulate excluding a portion at the rear-end of the electrode structure, i.e., by dragging the electrode body basis-to-tip through a portion of molten glass, polymeric resin, wax, etc. [139]. Other, alternatives can even involve the use of torches both for etching, which is common for carbon fiber electrodes, and for insulating procedures [135].

The fabrication of diamond microelectrodes is normally followed by the establishment of the necessary electrical connection, ensuring ohmic contacts. Several methods have been used for insulating the microelectrodes afterwards with most common sealings being made of various polymers including epoxy and nail varnish, glass, electrophoretic paint, etc. For metals, glass is very common, but for diamond microelectrodes, the surface roughness and the difference in thermal expansion difficult the task, even though it has been accomplished [101].

Polymers have been used to insulate diamond microelectrodes quite more extensively. A reliable, but skill demanding method consists in covering the whole surface and exposing the tip by touching it gently with paper soaked in a suitable solvent. The main drawback might be related with the chemical stability of the polymer given the extreme polarization potentials that are within the working range of diamond MEs. An alternative is the use of electrophoretic paint. The method consists on polarizing the ME so that the change in pH around it will cause the paint (polymer) to precipitate. Cathodic and anodic paints are commercially available. Although these organic coatings have the advantage of shrinking after cure, leaving a small diamond tip exposed, if the film is too rough, the coating will also shrink throughout the whole electrode body resulting in incomplete insulation. The process can be repeated but in the end, the diamond tip might remain covered. Since the coating tends to be very chemically resistant, it becomes difficult to remove it afterwards by using paper embedded in solvents as in the previous examples. The best solution so far has been to cut the coated diamond tip by FIB, which yields a disk shaped microelectrode, suitable for application, e.g. in SECM [101].

3.1.3.1.   The conductor-glass interface

Conducting wires or fibers heat sealed in glass are sensitive to the mismatch between the coefficients of thermal expansion of the electrode material and insulator. Most metals and glasses are poorly matched in thermal expansion; this mismatch leads to cracks on the interface that constitute a source of nonlinear diffusion (or edge effects) and leakage at macroscopic wires heat sealed in glass. An ME is all edge, i.e. the perimeter to area ratio is large. Microcracks at the junction provide an apparent area which dwarfs the electrode area. This is one of the reasons for the popularity of soft glass-insulated platinum, they have very similar equivalent linear coefficients of expansion [135].

3.1.3.2.   The conductor-epoxy interface

To avoid the interfacial problems arising from heat sealing metal in glass, many users of MEs simply cast the metal in an epoxy resin or use epoxy to bond the electrode material to a shrouding or support material. This can be far less technically demanding during preparation, but the use of an epoxy as a sealant or as a sheath raises other concerns. The epoxy must adhere well to the electrode material or the seal will leak and render the ME useless. Adequate adhesion to the primary support or shrouding material is also required. The stability of the epoxy in the electrolyte needs to be assessed, especially with regard when switching between aqueous and nonaqeuous media. While the metal-epoxy seal may not leak, species leached from the epoxy may degrade the quality of the voltammetric response and lead to an aged epoxy with microscopic defects. This is especially important when working in nontraditional, nonpolar solvents.

Adhesion is also an important factor when the electrode material is painted, sputtered, evaporated, or melted onto an insulating support. Noble metals especially will not adhere well to glass due to a low value of the work of adhesion. Undercoatings are used to prevent the metal from floating off the support during experiments. Cr, Ti or Ta underlayers are routinely applied to glass before thin gold or platinum films are sputtered or evaporated on [135].

3.2. Substrate preparation

3.2.1. Tungsten as substrate material for diamond growth

Tungsten is a hard, refractory metal (melting point = 3422 $^{\circ}$C) with electrical resistivity of 5.28×10^{-8} Ω.m and high chemical stability [140]. According to the E-pH diagram at 25 $^{\circ}$C, it is not attacked by most acid solutions, except complexing acids such as phosphoric or oxalic acid, undergoing passivation if anodically polarized [141]. WO_2 and WO_3 are the two most stable tungsten oxides, with the latter being the most thermodynamically stale at normal temperature and pressure conditions. In alkaline media the metal is slightly more unstable with a tendency to dissolve in tungstic ions WO_4^{2-} with hydrogen evolution. Upon anodic polarization it starts to corrode actively [141].

Hence, being a chemically and mechanically resistant material which can withstand the diamond growth temperatures by HFCVD (~600-950 °C), it is suitable to use as substrate for growing diamond. However, carbon, the raw material for diamond growth, is very soluble in tungsten. At CVD growth temperatures tungsten will transform into W_2C and WC, the latter being the most stable form [142]. Consequently diamond does not nucleate on tungsten, but on tungsten carbide.

Tungsten carbide (WC) is a very hard material with high melting temperature (although lower than tungsten, 2870 $^{\circ}$C), and metal-like electrical resistivity 2.2×10^{-7} Ω.m [143]. Although higher than that of CVD diamond, its thermal expansion at room temperature is of the same magnitude (WC= 5.2 to 7.3×10^{-6} $^{\circ}C^{-1}$, diamond = 2×10^{-6} $^{\circ}C^{-1}$) [123,143]. Tungsten carbide tends to increasingly oxidize as air humidity increases [144]. However, in aqueous solution the oxide layer becomes unstable and is removed [145]. Under anodic polarization WC can be progressively oxidized to different W_xO_y stoichiometries, exhibiting clear oxidation peaks at low positive potentials [146]. Considering the wide water stability window of diamond this oxidation of tungsten carbide is quite useful for evaluating the presence of porosity in the diamond films or even of surface contamination with tungsten from the heating filaments.

3.2.2. Tungsten wires

In order to effectively use tungsten as a microelectrode material whether as a raw metal or as a base metal for coating with other materials it has to be shaped adequately to fulfill the target application in terms of size, shape, mechanical strength, chemical and microstructural compatibility with the coating material, as is the case in this work. Shaping tungsten with the purpose of assembling single microelectrodes is best achieved with tungsten wire. This is because of the geometrical proximity between the wire form and common microelectrode geometries (disk, hemisphere, cone, cylinder, etc.), which allows it to be more easily transformed into those desired shapes.

In the following section, a method for fabrication of nanosharp wires of W, developed in the scope of this thesis, is described.

3.3.   Electrochemical etching fabrication of nanowires made simple, fast and cheap

E.L. Silva[1], R.F. Silva[1], M. Zheludkevich[1,2], F.J. Oliveira[1]

1-CICECO – Department of Materials and Ceramics Engineering, University of Aveiro, Portugal

2- MagIC, Institute of Materials Research, Helmholtz-Zentrum Geesthacht, Max-Planck Str. 1, 21502 Geesthacht, Germany

Abstract

A novel electrochemical wire etching method of fabrication of ultrasharp nanoelectrodes is reported. Tungsten wires can be sharpened to less than 10 nm tip radius in a reproducible way in less than 1 minute by using controllable hydrodynamic electrolyte flow combined with optimized electrochemical etching parameters. The method relies on the variations of the electric field at the surface of a metal wire, while the electrolyte solution is in motion, rather than on the ionic gradient generated in a static solution.

Keywords: Wire etching; Nanoelectrode; Tungsten; Hydrodynamic.

3.3.1. Introduction

Microprobes constitute very important tools when it is imperative to perform electrical or electrochemical operations in confined volumes of the microscale with minimum or no damage to the surrounding environment.

The fabrication of micro/nano probes has revolutionized the way research is done in various fields such as electroanalysis, biotechnology, medicine, imaging technology, etc. The downsizing of metal wires to dimensions close to the atomic scale has enabled

scientists to study micro- or even nano-scale volumes and greatly improve the ability to characterize such confined systems, whether the wires are used in their pure state or coated with another material [147–151]. Microelectrodes are the key elements that made possible the development of relatively new electrochemical techniques such as SECM (Scanning Electrochemical Microscopy) and SVET (Scanning Vibrating Electrode Technique) or imaging ones such as STM (Scanning Tunneling Microscopy). Through the use of microelectrode based techniques it has been possible to acknowledge fast reactions of the order of microseconds or less or even detect species in concentrations as low as a few ppb [7,24,152–154].

From all the different fabricating methods for microelectrodes, the electrochemical etching of a metal wire is widely used for single microelectrodes. Although the fabrication of micro and nanoelectrodes has been reported by many research groups, the method by which they are produced is generally quite similar: a metal wire is immersed in an electrolyte solution, centered in a ring, coil or tube, which work as the counter electrode (CE). Alternatively the wire is passed through a lamellae of electrolyte solution held by surface tension to the surrounding CE ring. Upon applying a certain voltage, the ionic concentration gradient at the meniscus in contact with the wire leads to its sharpening [136,137,155–163], according to the equations 3.1 and 3.2 for the case of tungsten.

Cathode reaction: $\quad 6H_2O + 6e^- \rightarrow 3H_2(g) + 6OH^-$ $\qquad$ (Eq. 3.1)

Anode reaction: $\quad W(s) + 8OH^- \rightarrow WO_4^{2-} + 4H_2O + 6e^-$ $\quad$ (Eq. 3.2)

Overall: $\qquad W(s) + 2OH^- + 2H_2O \rightarrow WO_4^{2-} + 3H_2(g)$
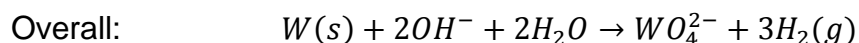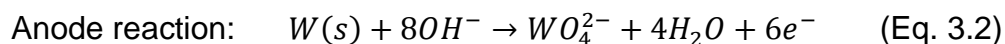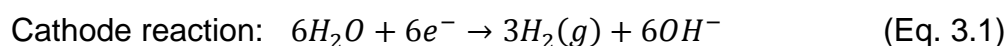
Even though nanometric tip curvature radiuses and high aspect ratios can be obtained by such a procedure, it can be rather complex [136] and the success rate for producing usable tips can be quite low in consequence of the many variables involved [164].

Although the meniscus allows etching the wire to a pointed shape, many problems arise from using this configuration if extremely sharp tips are to be obtained in a reproducible

manner. In a static configuration, the weight of the portion of wire below the etching zone strongly conditions the tip curvature radius. Moreover, if the system power is not turned off at the exact moment of the drop-of the sharp tip will become blunt due to over-etching [163,165,166]. Furthermore the positioning of the wire during the etching is critical and has a determinant influence in the shape, size and quality of the sharp tip. In fact, even slight vibrations, like sound vibrations will affect the quality of the tips [166]. Avoiding these drawbacks might require a skilled operator and frequently the controlling systems are complex, because the current cut-off time strongly marks the difference between a good tip and a blunt tip [136,167]. Hence, although the existing electropolishing methods can provide metal tips with high quality, suitable for applications such as STM (Scanning Tunneling Microscopy) or AFM (Atomic Force Microscopy), the fabrication procedures tend to be highly sensitive to small modifications.

Here we report an alternative method in which the quality of the final tip depends exclusively on the parametric adjustment of all the components involved in the etching process, does not require a fast or dedicated current cut-off circuit and allows the production of sharp metal nanotips in less than 1 minute, in a reproducible manner.

3.3.2. Experimental

A simple method for the fabrication of a sharp micro/nanotip is described. This can be accomplished by the assembly of a wire etching device comprising 3 main elements: i) a DC power source for generating an etching voltage for metallic material removal from the wire and consequent wire sharpening; ii) an etching unit constituted by the wire to be etched, a counter electrode and an electrolytic fluid which closes the circuit between the wire and the electrode, providing the necessary chemical species to react with the wire to be electropolished and the physical mean to transport the etched material; iii) a pump and a flow circuit where the electrolyte fluid is made to flow in order to close the circuit on the etching unit (Figure 3.1).

In this work, tungsten wires were used for demonstrating the performance of this novel electrochemical etching method. The counter electrode was also made of tungsten. Aqueous electrolyte solutions with various concentrations of NaOH from 0.5 to 4 M were

used as etching fluid. A commercial pump (Boyu SP-700, China) with a flow capacity of 230l/h was used to provide the closed-circuit motion of the electrolyte solution. The constant flow of the electrolyte in a closed circuit, has several advantages. The metal wire is not immersed in a static liquid, instead it is positioned in the center of a column of flowing electrolyte. By this system the electrochemical etching apparatus is greatly simplified and the shape, size and quality of the metallic tips will be almost exclusively dependent on the electropolishing parameters and not on thorough operation details. The metal wire to be etched requires only to be aligned vertically at the center of the column of flowing electrolyte.
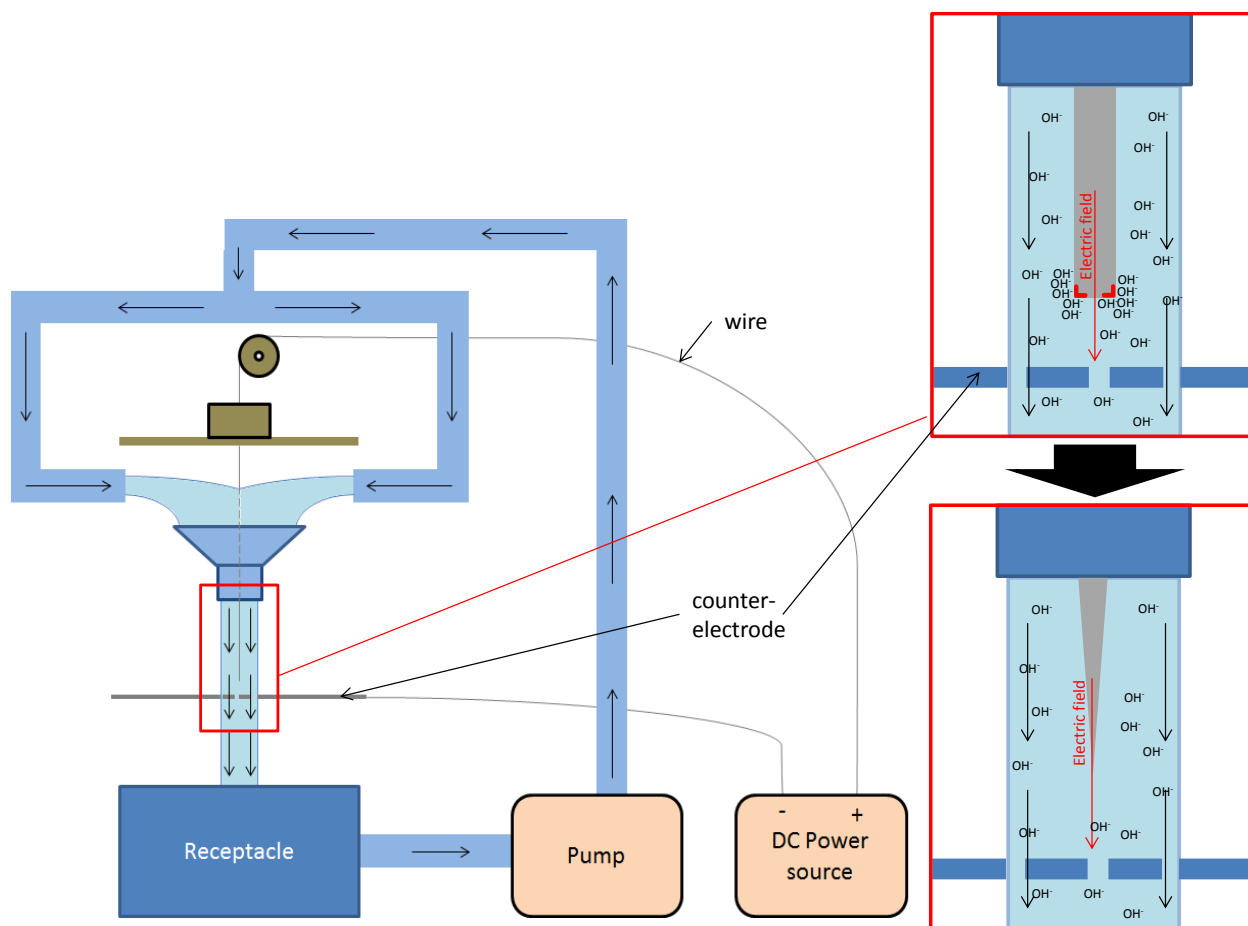
Figure 3.1 - Electrochemical etching assembly, evidencing the etching mechanism (inset).

3.3.3. Results and discussion

A device integrating this new electrochemical etching method is depicted in Figure 3.1. The essence of the method is the absence of meniscus formation. In this traditional approach the electrochemical etching occurs due to the OH^- ionic gradient that is formed at the meniscus between the metal wire and the electrolytic solution.

Instead, the suggested method is based on a reverse gradient compared to that observed at a meniscus. The etching procedure occurs in hydrodynamic conditions under an applied electric field. The ionic gradient driving the electrochemical etching occurs when voltage is applied to the system, as a consequence of the shape of the wire.

Taking a tungsten wire of 125 µm diameter and optimized parameters, this method can reproducibly deliver nanoelectrodes as sharp as 10 nm tip curvature radius or less with aspect ratio up to 15:1 (Figure 3.2a, b) in less than 60 seconds (Figure 3.2c). Accomplishing the fabrication of sharp tungsten wires of the micrometer or the nanometer scale by the following uncomplicated procedure: **1)** alignment of the metal wire until it is well centered with the collecting funnel and with the counter electrode bellow; **2)** adjustment of the distance between the wire and the counter electrode; **3)** turning on the pump to activate the flow motion of the electrolyte solution; **4)** turning on the DC power source previously set to the desired voltage (say 30V), during the desired amount of time (say 50 s); **5)** turning off the power source; **6)** cutting the needed part of the wire to be used as an ultrasharp electrode; **8)** restarting from 1) for another electrode.
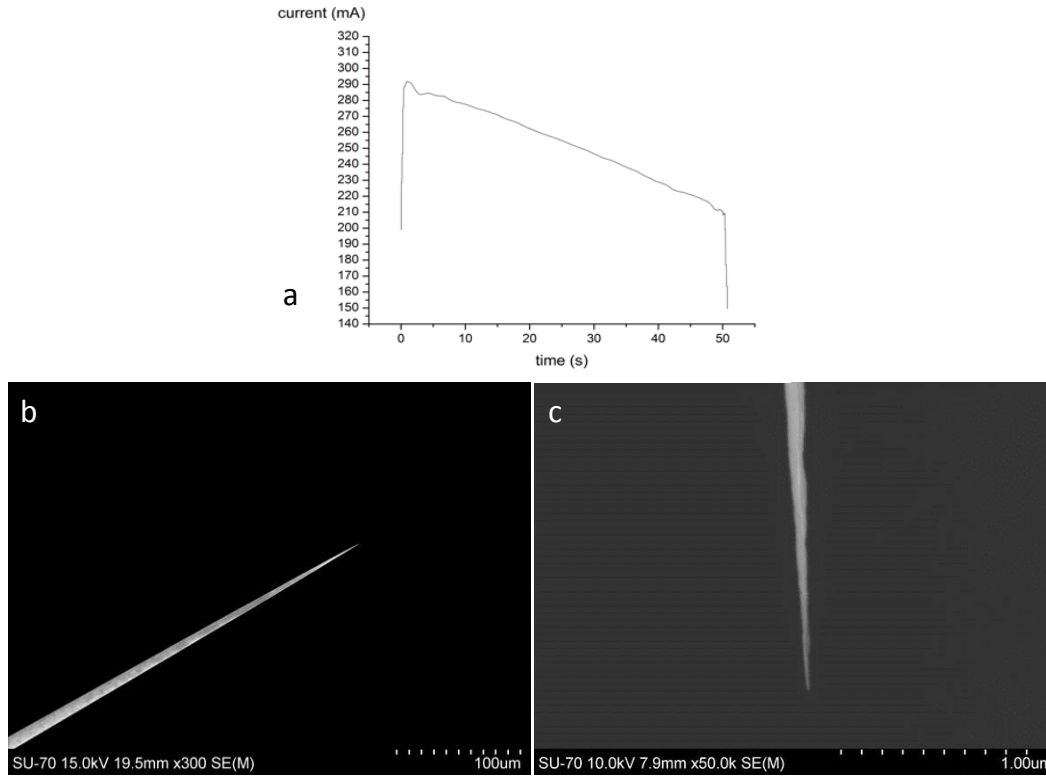
Figure 3.2 – Electrochemical etching process showing a) Current-time dependence using 1M NaOH and 30V applied on the DC power source, and electrochemically etched tungsten nanowire in b) low magnification and c) high magnification.

Given that the method is based on a fluid in motion under the influence of an electric field, electrohydrodynamics must be considered. According to the Ohmic model, in the presence of a monovalent binary electrolyte which is fully dissociated with constant properties, the current density in a flowing electrolyte solution can be described by:

$$J = QKE - D\nabla Q + Qv$$ (Eq. 3.3)

Where Q is the charge density, K is the charge mobility, E is the electric field, D is the diffusion coefficient, ∇ is the gradient operator, and V is the fluid velocity [168].

The first term on the right side of the equation is the drift current of the free charges which move with a velocity $K\vec{E}$ relative to the fluid. The second term is the molecular diffusion, which can be considered negligible in comparison to the externally applied

voltage (the thermal voltage is 25 mV at room temperature), and the third term is due to convection, which makes the charge to move with the fluid [168].

Considering the Coulomb force alone, the equations describing the electrohydrodynamic movement result from the combination of fluid dynamics (Eqs. 3.4 and 3.5) and electrodynamics (Eqs. 3.6, 3.7 and 3.8):

$$\nabla \cdot v = 0 \qquad \text{(Eq. 3.4)}$$

$$\frac{\partial v}{\partial t} + (\vec{v} \cdot \nabla)v = -\frac{1}{\rho}\nabla p + \frac{\mu}{\rho}\nabla^2 v + \frac{QE}{\rho} \qquad \text{(Eq. 3.5)}$$

$$\nabla \cdot E = \frac{Q}{\varepsilon} \qquad \text{(Eq. 3.6)}$$

$$E = -\nabla \phi \qquad \text{(Eq. 3.7)}$$

$$\frac{\partial Q}{\partial t} + (KE + v) \cdot \nabla Q = -\frac{KQ^2}{\varepsilon} \qquad \text{(Eq. 3.8)}$$

Where E is the electric field, Q is the charge density, ε is the permittivity, Φ is the electric potential, $\vec{v}$ is the fluid velocity, ρ is the density, p is the pressure, μ is the viscosity, K is the charge mobility, t is the time and ∇ is the gradient operator.

Equations 4 and 5 ignore the compressibility of the fluid and describe its movement taking into account the viscosity and the electric field. Equations 3.6, 3.7 and 3.8 are the Maxwell equations accounting for the electrodynamics of charged molecules in the fluid [168].

For perfect conductors (mercury, water) or perfect dielectrics (nonpolar liquids like benzene), the electric stress is balanced by changes in the shape of the interface, and the Coulomb force is in the direction of the electric field [169]. Because low angle regions (e.g. edges, apexes) exhibit a higher density of electric field lines, they will be etched preferentially in relation to high angle regions. An auxiliary electrode positioned

perpendicularly below the wire being electropolished, causes the shape of the resulting tip to be concordant with the vertical direction of the electric field.

Since there is a broad range of possible parametric combinations, a study was conducted based on the variation of each relevant parameter, regarding the device depicted in Figure 3.1 (Table 3.1).

Table 3.1 - Range of studied parameters used for electrochemical etching.

Electrolyte concentration (mol.dm^{-3})	Applied voltage (V)	Distance wire-electrode (mm)	Wire diameter (µm)	Counter - electrode diameter (µm)	Etching time (s)
0.5	5	2	125	125	10
1	10	4	250	250	20
2	20	6		300	30
3	25	8		1000	40
4	30	10			50
	40	12			60
		14			70

3.3.3.1. Effect of electrolyte concentration, applied voltage and wire-CE distance

Considering NaOH as a well suited electrolyte for the electropolishing of tungsten wires, the effect of its concentration was studied in the range of 0.5-4 M [170–172]. The concentration of 1 M was considered to be optimal because it ensures a good balance between tip curvature radius and surface roughness. Lower concentrations contributed to a higher tip curvature radius and lower aspect ratio, while stronger electrolytes tend to yield higher surface roughness (Figure 3.3).

15.0kV ×1.00K 30.0μm   15.0kV ×20.0K 1.50μm
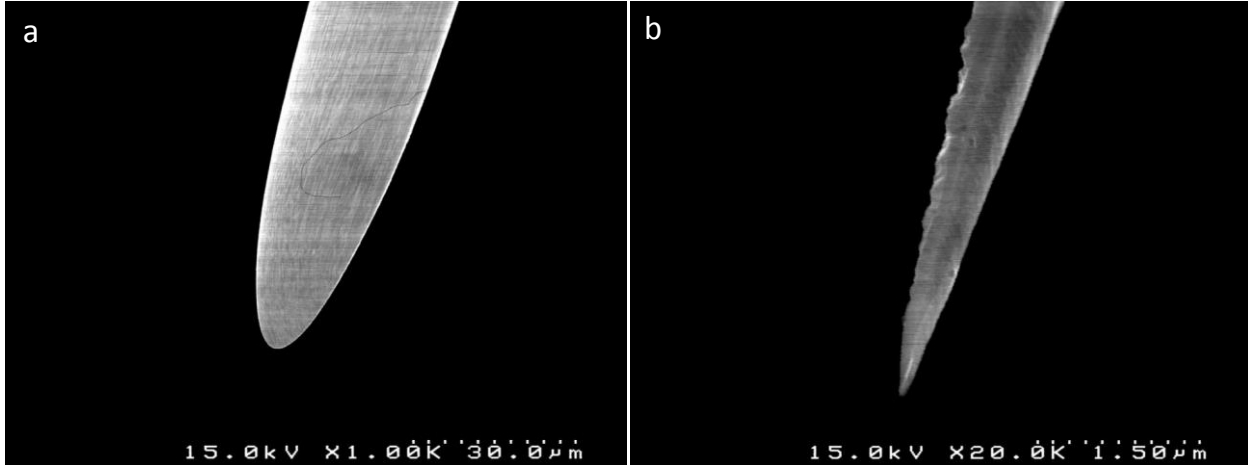
Figure 3.3 – Effect of electrolyte solution concentration on the shape and surface morphology of the etched tungsten wires, evidencing large tip curvature and low aspect ratio with a) 0.5 M NaOH and high surface roughness with b) 4 M NaOH.

Similar effects were found for the voltage applied between the wire and the counter electrode. A voltage of 30 V in the DC power source was considered to be optimal for the etching process. With lower voltage there is a tendency for the curvature radius of the tip to be larger, whereas with higher voltage the surface of the etched wire tends to exhibit higher roughness and higher number of imperfections (Figure 3.4).

The potential gradient determining the electric field (Eq. 3.7) depended on the distance between the wire and the counter electrode. Distances of 2-14 mm between both were tested. A distance of ~4 mm was found to provide the best results. Lower distances yield tips with larger curvature radius and higher distances will promote the appearance of a less smooth surface with possibly compromising defects (Figure 3.5).

This balance between sharpness and roughness can be linked to surface interactions occurring during the etching procedure. Depending on the current density metal removal from the surface of the wire can occur more selectively or more uniformly, for which the nomenclatures of etching and polishing have been ascribed, respectively. The selection of an adequate current regime is important in order to ensure that metal removal occurs homogeneously, avoiding the high energy regions (defects, grain boundaries) to be excessively attacked [173].
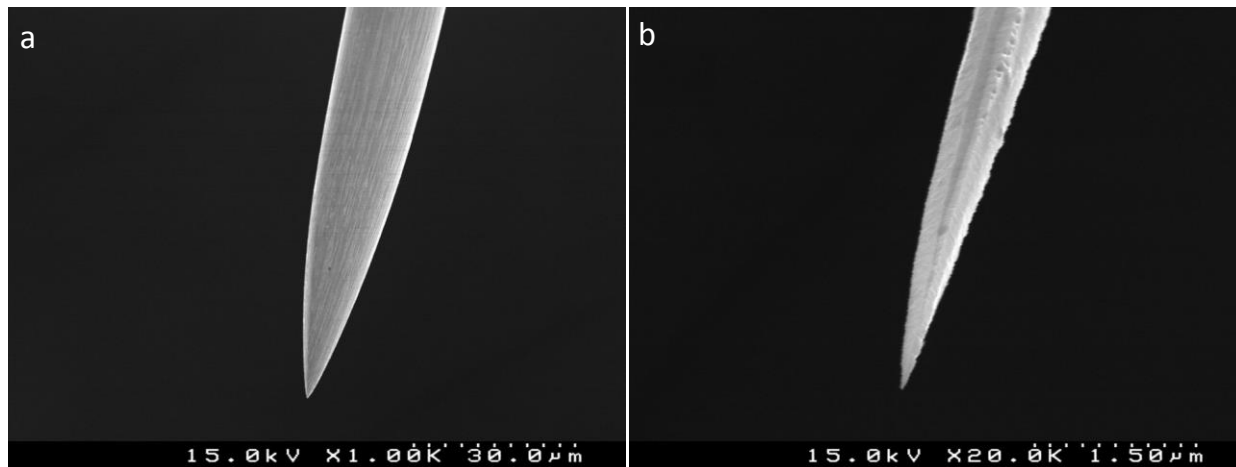
Figure 3.4 - Effect of applied voltage on the shape and surface morphology of the etched tungsten wires for a) 5 V and b) 40 V.
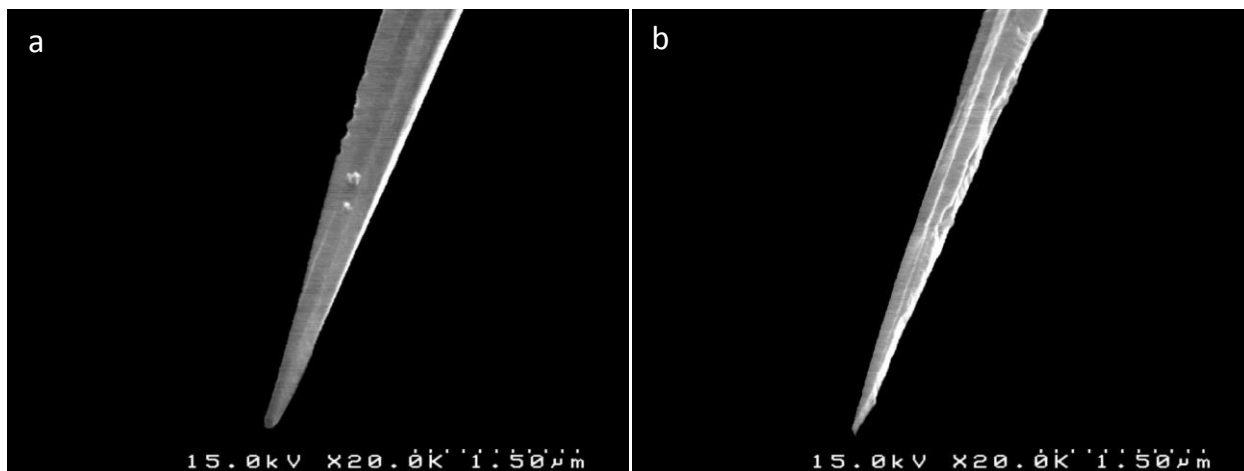
Figure 3.5 - Effect of the wire-counter electrode distance on the shape and morphology of the electrochemically etched tungsten wires for a) 2mm and b) 14mm.

3.3.3.2. Effect of etching time

Etching periods of 5 to 70 seconds were studied keeping the remaining conditions constant. Time is a very important variable because the electrochemical etching is preceded by the non-electrochemical dissolution of tungsten trioxide (WO_3) (Eqs. 3.8, 3.9) [167], which is the most stable tungsten oxide and is always present in a thin layer at the metal surface.

$$WO_3(s) + OH^- \rightarrow HWO_4^-(aq) \qquad\qquad \text{(Eq. 3.8)}$$

$$HWO_4^-(aq) + OH^- \rightarrow WO_4^{2-}(aq) + H_2O \qquad\qquad \text{(Eq. 3.9)}$$
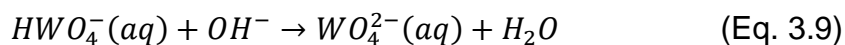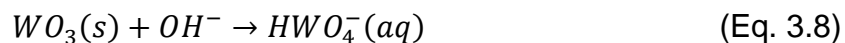
The progression of this reaction can be seen in Figure 3.6a and Figure 3.6b, showing tungsten wires etched for 30 and 40 seconds, respectively, keeping all other parameters constant. In Figure 3.4a, after 30 seconds of etching the surface of the wire still presents a visible pattern resulting from the remaining oxide at the surface. After a few seconds, no oxide remains as it can be seen by the difference in the surface morphology shown in Figure 3.6b and Figure 3.6a. Hence, after removal of most of the oxide at the surface of the wire the etching rate will be faster, as will be reduction in the wire length. The necessary etching time will also depend on the electrolyte concentration and the flow rate of the pump because they determine the instant concentration of OH⁻ available at the surface of the wire. From the third term of equation 3.3 it can be seen that higher fluid velocity will also yield higher current density. Considering a constancy of parameters during etching, varying these two parameters will also influence the quality and size of the tip. With 50s etching time, according to the conditions in Table 3.2, the wire can be reproducibly sharpened down to a tip radius of less than 50 nm. Longer electropolishing periods do not implicate compromising the tip radius and tend to yield higher aspect ratio. An electropolishing time of 50 seconds was found to be optimal, considering that the rate of tips per hour is also important.
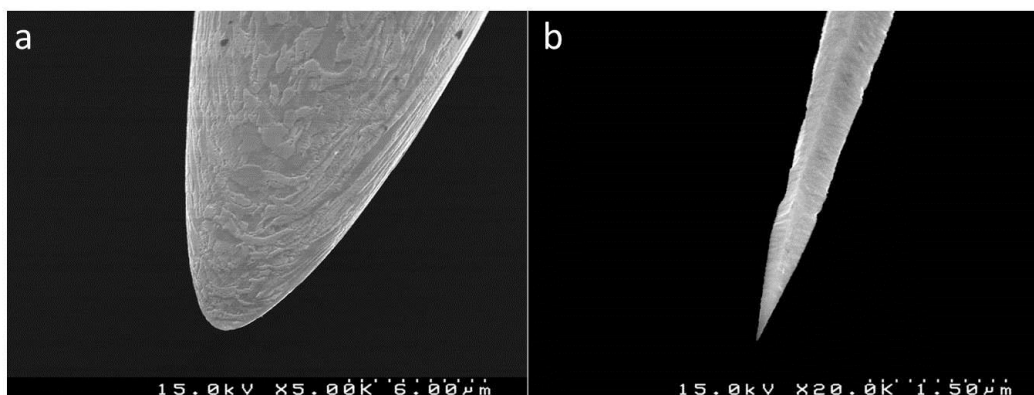
Figure 3.6 - Tungsten wires during etching in 1M NaOH with 30 V applied voltage showing a) oxide still present on the surface of the wire after 30 s; b) wire without oxide after 10 extra-seconds of etching.

Table 3.2 - Optimized wire etching conditions, adequate for producing nanowires.

Electrolyte concentration (mol.dm⁻³)	Applied voltage (V)	Distance wire-electrode (mm)	Wire diameter (µm)	Counter - electrode diameter (µm)	Etching time (s)
1	30	4	125	250	50
				300	
				1000	

3.3.3.3. Effect of the auxiliary electrode diameters

The diameter of the auxiliary electrode was found to be perhaps the most critical parameter if tips of the nanoscale are to be produced reproducibly. The smaller the ratio between the diameters of the wire to be etched, d_w, and the counter-electrode, d_{ce}, the more reproducible becomes the fabrication of nanotips. We verified that by using a ratio $d_w/d_{ce} < 0.5$, more than 60% of the tips would exhibit a curvature radius with less than 50 nm. This is because the electric field becomes more stable. As the electrolyte solution flows, the wire will tend to oscillate, which causes instability of the electric field and the hydrodynamic regime. Considering a sufficiently wide column of flowing electrolyte, smaller d_w/d_{ce} ratios will reduce the probability of the wire oscillating outside the zone of action of the vertical electric field (Figure 3.7).

The ratio between the diameter of the column of flowing electrolyte solution, d_{fes}, and the diameter of the counter electrode was found to be also important in the presented device configuration since as d_{ce} approaches d_{fes} the electrolyte solution will tend to increasingly splash to the sides as it hits the counter electrode causing significant turbulences.

By adopting the conditions indicated in Table 3.2 we have produced the nanosharp wires shown in Figure 3.8, Figure 3.9 and Figure 3.10 with counter electrode diameters of 250, 300 and 1000 µm, respectively.
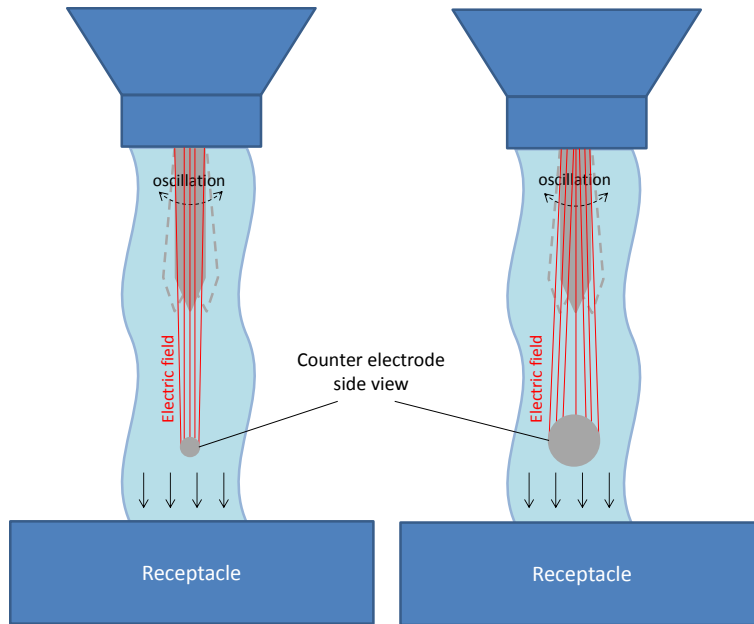
Figure 3.7 - Effect of counter electrode diameter: the electrical field between the wire and the counter electrode becomes increasingly more stable for larger CE diameters.
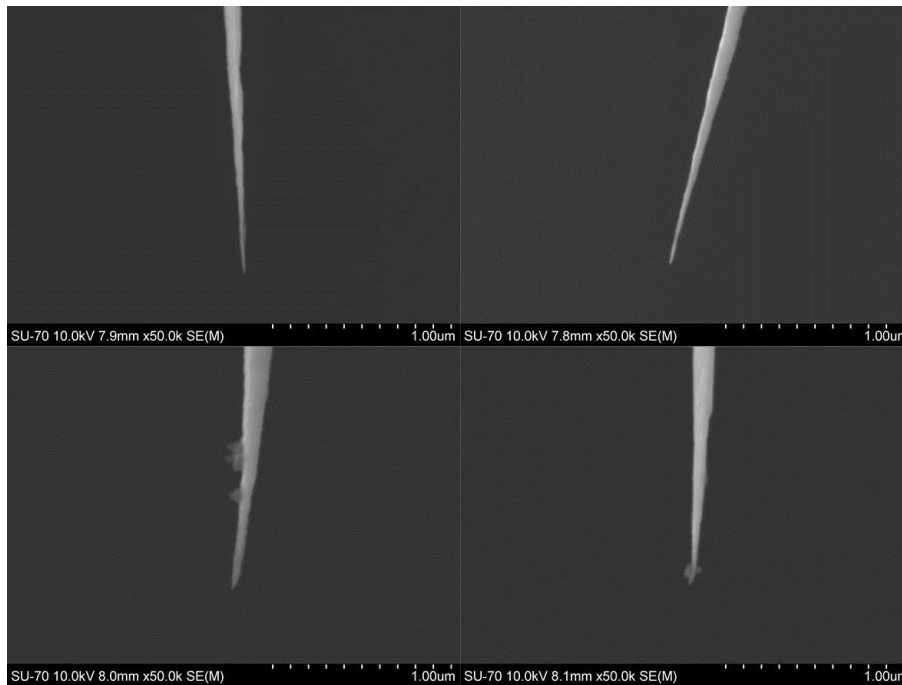
Figure 3.8 - W tips electrochemically etched following the conditions from Table 3.2, with a CE diameter of 250 μm.
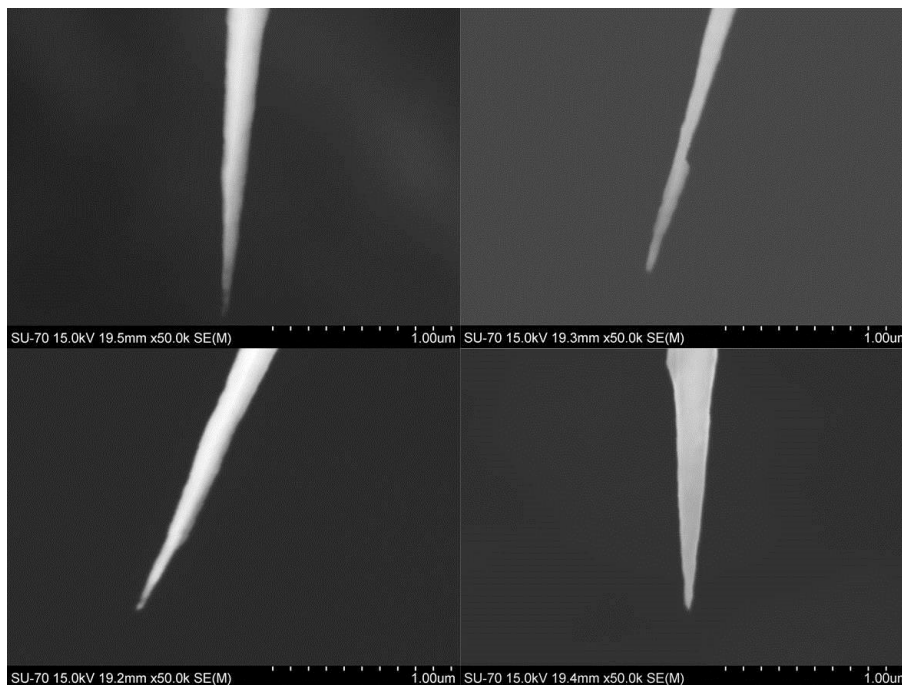
Figure 3.9 - W tips electrochemically etched following the conditions from Table 3.2, with a CE diameter of 300 μm.
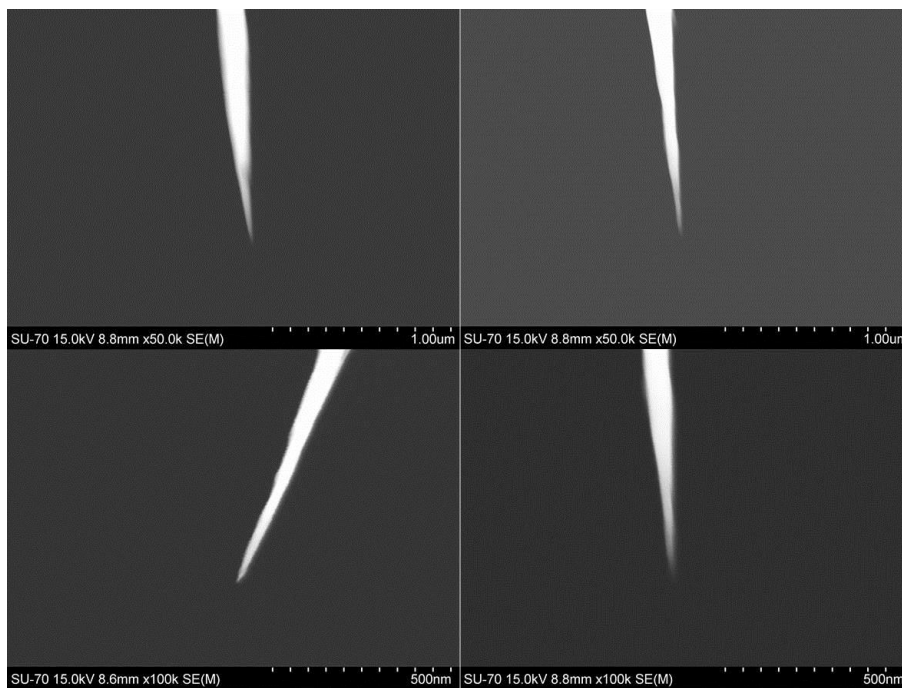
Figure 3.10 - W tips electrochemically etched following the conditions from Table 3.2, with a CE diameter of 1000 μm.

Perhaps the best part of the method is depicted in Figure 3.11, where a collection of bad quality etched wires is shown, still exhibiting high aspect ratio and tip curvature in the 50-100 nm range.

Although this work was focused on the etching of tungsten wires, further applicability of this method may be found for metals forming a passive film, using electrolytes which lead to partial dissolution of this layer. As demonstrated this method can be implemented with very basic instrumentation and with either manual or automatic control. The applicability of sharp tungsten wires produced in this way has been demonstrated with CVD diamond coatings for scanning probe electrochemical measurements [149,174].
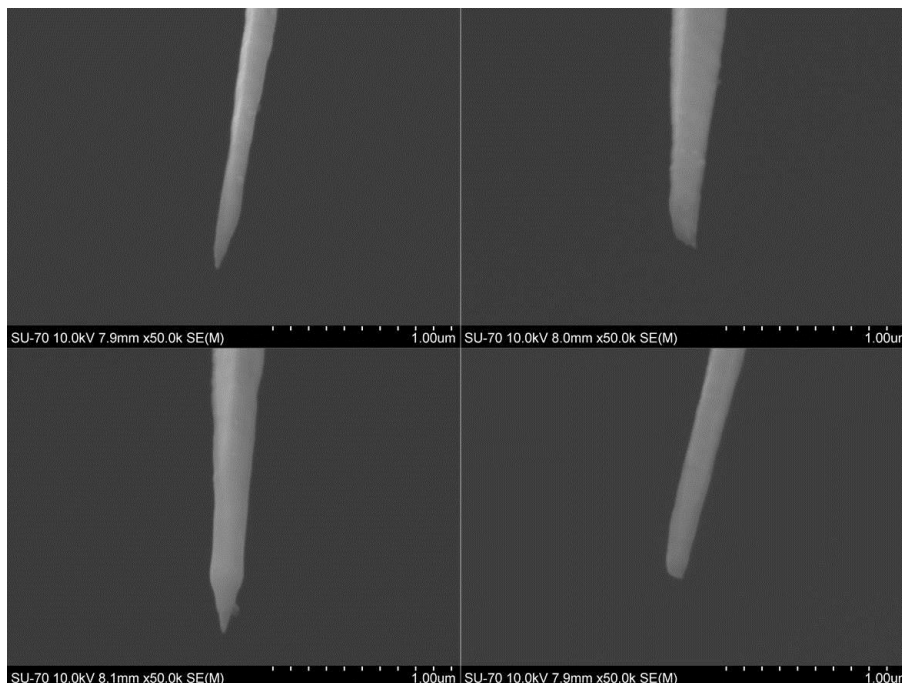
Figure 3.11 - W etched tips with bad quality, still showing adequate surface morphology and near-nanoscale dimensions.

3.3.4. Conclusions

A new, simple, electrochemical etching method was successfully developed without requiring any complex apparatus or electronic/mechanical system. By using a power source, an etching unit and a flowing circuit we are able to fabricate high quality

tungsten tips suitable for using in application were a needle-type probe is needed to perform an electrical, electrochemical or mechanical action. Besides the bare wire application, the easily achievable nanoscale miniaturization that this method provides, also simplifies the testing of already existing or newly found materials at the small scale, provided that they can be grown as suitable thin films.

Tungsten wires were easily etched to acquire a pointed shape with sub-micrometric or nanometric tip curvature radius, in less than 60 seconds, by following simplistic manual procedures. Needle shaped wires with <10 nm radius and high aspect ratio were fabricated in short etching periods of 50 s.

Acknowledgements

3.4.　　Substrate pre-conditioning

Another crucial step before the growth of polycrystalline CVD diamond is adequate substrate conditioning, the so called seeding. Substrate seeding can be made by a variety of ways. The choice of method relies on the growth technique and the desired microstructure. The use of diamond powders has always been the prime choice, when crystal orientation is not very important. It provides the best results with highest nucleation density. Besides diamond powder other abrasive powders like silicon carbide or cubic boron nitride have been used, although the results are not as good. Alternatively, surfaces coated with different forms of carbon such as graphite, amorphous carbon, diamond-like carbon, C60, and even mechanical oil have been used [175–178].

The seeding procedure is generally based on sonication of the substrate immersed in a diamond powder suspension, although mechanical scratching can provide higher nucleation density, but with lower reproducibility. Scratching procedures change the surface morphology, by creation of all sorts of surface defects, which exhibit higher surface energy, i.e., less stability. Therein these sites can promote adsorption of diamond forming gas species and enhanced bonding.

When chemical vapor deposition is assisted by microwave plasma, another popular seeding method consists on the use of bias, an electric field that allows the formation of diamond nuclei when charged species are involved, as it happens in the plasma. Biased growth can also be used with HFCVD although a more precise adjustment of growth conditions is required. The main advantages of biasing are the enhanced seeding density and the possibility of growing oriented crystals on mirror polished surfaces.

The grade of diamond powder used for seeding can be determinant for the resulting microstructure. Particularly, if nanocrystalline diamond is to be grown, the use of nanometer size diamond powder (nanopowder) greatly facilitates the process, because it can provide much higher nucleation density than micrometer size diamond powder.

Since the present work is based on the development of microelectrodes, from the beginning it made sense to use nanopowder. Regardless of the final result, nanoparticles are not easy to work with. The formation of considerable agglomerates is

hard to avoid and removal of the excess powder from substrates can be even harder. If diamond is grown for mechanical and abrasive purposes on large substrates this removal is somewhat irrelevant. In the case of electrochemical probes, when nanometer dimensions are pretended and a few micrometers is the maximum dimension, if the probe is to be of any use, powder removal becomes a very important issue. Adding to this, for quantification of electrochemical species of interest a well-defined geometric area is also very important.

Hence a study on substrate seeding was performed using nanodiamond powder suspensions with different concentration and sharp tungsten wires, the substrate for the microelectrodes in this work.

3.4.1. Experimental

A diamond nanopowder (3-5 nm) suspension in water was used with fixed concentration of 0.9 g/l for seeding sharp tungsten wires by sonication. Different sonication periods of 30, 20, 10, 5, 3 and 1 minute were used, with cleaning times of 30 minutes to 1 h by sonication in distilled water, ethanol or acetone (all were tried both isolated or combined during longer periods). Each tungsten wire was suspended with only the tip dipped into the diamond suspension or cleaning fluid.

3.4.2. Results and discussion

The SEM micrographs in Figure 3.12 show the surface of seeded tungsten wires after the cleaning procedure showing that the diamond nanoparticles may adhere to their surface and can be almost impossible to remove by sonication. For seeding times of 20 and 30 minutes, nearly full coverage of the tungsten wire with diamond nanoparticles was observed regardless of the cleaning time. For the wire seeded during 10 minutes considerable amounts of residual powder were still found on the surface. For the shortest surface scratching time of 1 min, nearly all diamond nanoparticles were removed with only a few particles being observed on the tungsten wires. However, after CVD diamond growth on tips seeded for such short times the diamond films were not closed, showing large amounts of porosity. Porous films would sometimes be observed

as well for the 3 minute seeding. For 5 min seeding, very few powder particles remained on the tungsten wires and the resulting films were consistently non-porous. At this stage the sharp tungsten wires were fabricated with tip diameter between 100-300 nm.

The improvement of the electrochemical etching system and its optimization allowed the fabrication of sharp tungsten tips with tip radius reproducibly between 5-50 nm radius and higher aspect ratio than the ones used for the seeding study. When trying to reproduce the same seeding procedure with these nanosharp wires, it was observed that the tips were many times damaged after 5 min seeding and that the powder was increasingly more difficult to remove. The remaining useful tips would exhibit consistent porosity after CVD diamond deposition. The reason for this is probably linked to the inertial momentum of the sharp wires. The firstly used W wires had tips that are big in comparison to the diamond nanopowder suspension. As the wire tip was decreased it probably started to vibrate with an amplitude similar to that of the diamond nanoparticles, i.e., the particles (3-5 nm) were not causing significant mechanical damage to the wire anymore, the wire would just move along with the particles.

Hence another strategy was adopted for these smaller tips. The concentration of the nanopowder suspension was optimized to a value of 1.25 g/l, well dispersed in distilled water. After that, the sharp wires were simply dipped first in the suspension and then in a goblet with clean distilled water. This dip coating method ensured that full-coverage by CVD diamond was readily achieved during the diamond growth process (Figure 3.13).
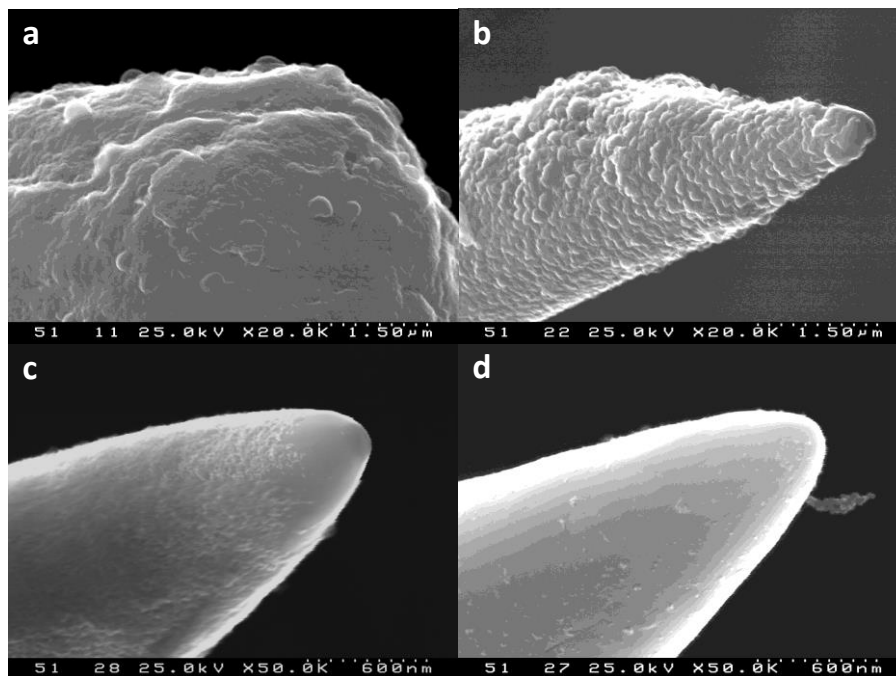
Figure 3.12 – Tungsten wires after sonication in nanodiamond powder suspension during a) 30 min; b) 20 min; c) 10 min; and d) 5 min, and cleaning afterwards in distilled water during 30 min.
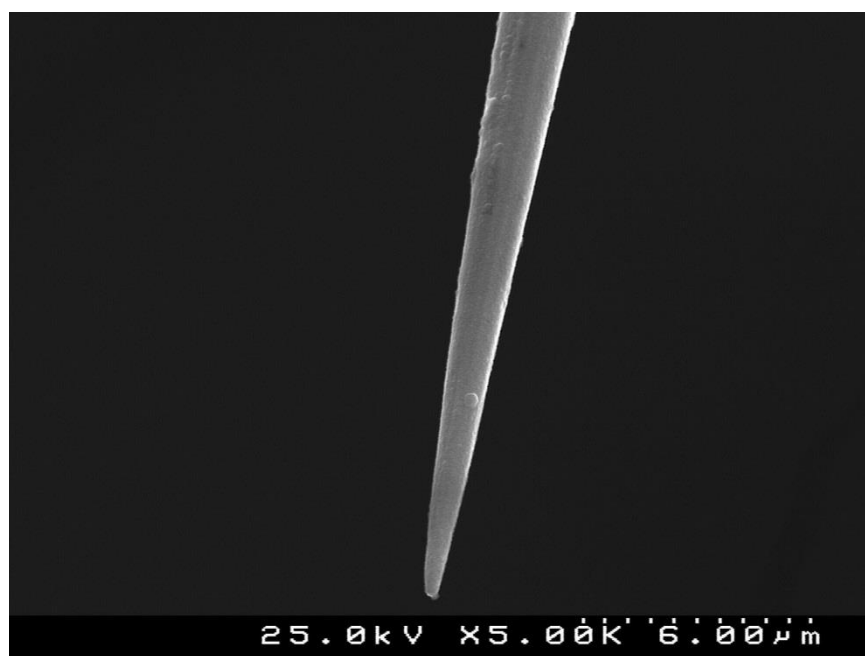
Figure 3.13 – Tungsten wire coated with a CVD diamond film (30 min. growth) after seeding by dip coating in a nanodiamond powder suspension.

3.5. CVD diamond growth

3.5.1. Practical considerations

CVD diamond thin films can be grown on top of a wide range of ceramic (silicon carbide, silicon nitride, etc.), metallic (silicon, tungsten, molybdenum, etc.) or composite (e.g. hardmetal) substrates. Because of the differences in the crystalline structure of each material, a substrate conditioning is normally required for diamond films to grow heteroepitaxialy. This preparation commonly consists on seeding the substrate with diamond powder by mechanical or ultrasonic means, as seen above, to create nucleation sites from which the growth process begins. The substrate conditioning largely influences the type of microstructure of the diamond films as the growth of microcrystalline or nanocrystalline diamond strongly depends on the nucleation density (Figure 3.14) [179].

Besides the seeding procedure, the microstructure of the films is further adjusted by the growth parameters: filament temperature, substrate temperature, CH_4/H_2 ratio, total pressure and total gas flow. Among these, the CH_4/H_2 ratio is probably the most important growth parameter. Low CH_4/H_2 ratios tend to promote the growth of microcrystalline diamond (MCD) whilst higher ones enhance a secondary nucleation phenomena favoring the growth of nanocrystalline diamond films (NCD). The filament temperature determines the amount of activated gas species and the substrate temperature essentially affects the atomic diffusion, the diamond grain size and the etching rate of sp^2 bonded carbon [180]. The effects of the total pressure and gas flow tend to depend on the other growth parameters and on the geometries of the substrate and reaction chamber [181]. Furthermore, by adding other gas species containing boron, nitrogen, phosphorus or sulfur, it is possible to obtain doped diamond with distinct electrical properties. Figure 3.15 is a schematic drawing of the modified HFVCD system used in this work for producing boron doped diamond coatings on sharp tungsten wires.

	Low nucleation density thin films	Low nucleation density thick films	High nucleation density
Low rate of secondary nucleation			
High rate of secondary nucleation			
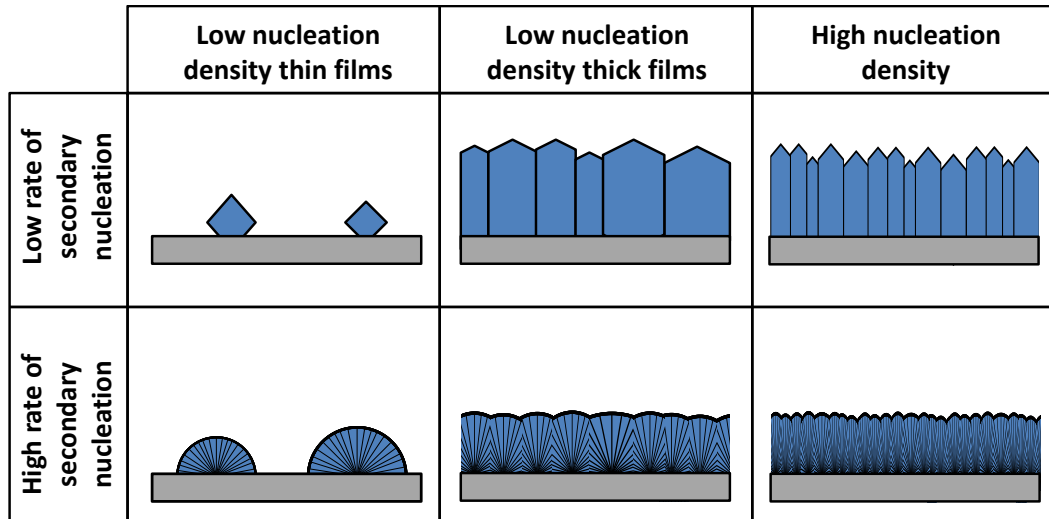
Figure 3.14 - Dependence of the diamond film type with nucleation density and secondary nucleation rate (adapted from [179]).
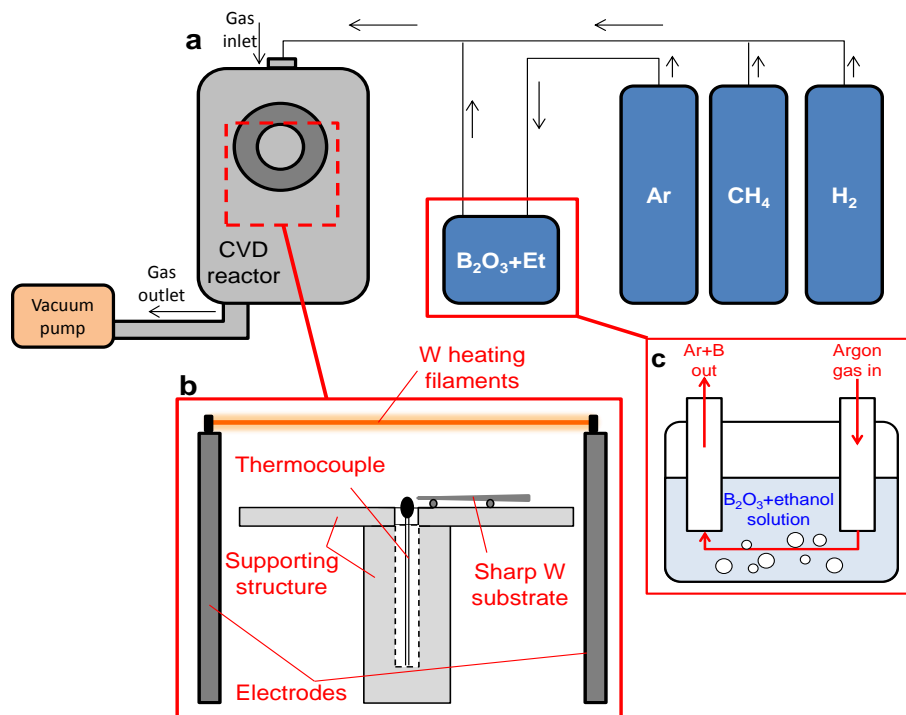
Figure 3.15 – HFCVD system showing a) reactor and gas circuit; b) CVD components inside the reactor; c) gas washing bottle containing solution for boron doping.

3.5.2. Selection of diamond growth conditions

Because CVD diamond is a polycrystalline material the main source of impurities and imperfections is mostly at the grain boundaries. The importance of growing high quality diamond films is directly related with the achievement of the impressive electrochemical behavior discussed in section 2.6 and reviewed several times by other authors [50,70,182]. This goal is normally better reached for larger diamond crystallite size, the so called microcrystalline diamond (MCD). However, for attaining higher levels of miniaturization it is important to keep the grain size as small as possible, without compromising the electrochemical properties. Regarding this perspective, growing nanocrystalline diamond (NCD) is by far a better choice, although there are some inherent limitations to the process. High quality NCD normally requires a gas phase chemistry different than that of MCD. Normally high concentrations of argon are used and the growth rate tends to be extremely slow, generally requiring several hours to grow the desired coating.

The following work in section 3.6 describes the development of fast coating sharp tungsten wires with boron doped nanocrystalline diamond, the first breakthrough of the present work that resulted in a scientific publication in a SCI journal. At this early stage a significant improvement on the fabrication process was achieved, with the sharp tungsten wires being fully coated after only 30 minutes growth, when periods of 5-10 h growth were the standard for other authors, sometimes even with bias enhancement [183]. The electrochemical behavior of these films was not the best obtained here, but their improvement was achieved afterwards, as described below in section 3.8.

Section 3.7 was dedicated to the study of the interfacial region between the diamond coatings and the tungsten substrates. A combination of microscopy techniques was used to acknowledge the microstructural character of this transitory region and to gather evidence of the presence and distribution of boron in the diamond films.

3.6. Fast coating of ultramicroelectrodes with boron doped nanocrystalline diamond

E. L. Silva[1], M. A. Neto[1], A. J. S. Fernandes[2], A. C. Bastos[1], R. F. Silva[1], M. L. Zheludkevich[1], F. J. Oliveira[1]

[1] CICECO- Dept. of Ceramics & Glass Engineering, University of Aveiro, 3810-193 Aveiro, Portugal

[2] Physics Department, University of Aveiro, 3810-193 Aveiro, Portugal

Abstract

The present work is focused on the deposition of thin boron doped nanocrystalline diamond (B-NCD) films on electrochemically etched tungsten wires by the hot filament assisted CVD method. The goal is the manufacturing of robust inert ultramicroelectrodes (UMEs) with a superior performance to be used for localised electrochemical analysis. The conductive diamond films can confer high stability of chemical and physical properties as well as low background current.

Filament and substrate temperatures were kept constant at 2350ºC and 670ºC, respectively. The total system pressure was equal to 50 mbar and the CH_4/H_2 gas flow ratio was 0.07. Boron was the used doping agent by solving B_2O_3 in ethanol, with a B/C content of 15000 ppm, and the solution was then dragged with argon gas flowing through a bubbler. The $(Ar+B)/H_2$ ratio values varied within the range of 0.06-0.21. The film growth rate decreases with the boron content increasing, but larger $(Ar+B)/H_2$ ratios result in smoother surfaces. UMEs insulation was carried out with epoxy resin in a home built device.

The production of very sharp tungsten tips fully coated with B-NCD after just 30 min, for a $(Ar+B)/H_2$ ratio of 0.21, is one of the main outcomes of this work. The cyclic voltammetry showed a stable behavior with a wide electrochemical window of ~2.25 V in a 0.05 M NaCl solution proving applicability of the developed UME for localized electroanalytical studies in biomedical and corrosion applications.

Keywords: Nanocrystalline diamond; Boron doping; Ultramicroelectrodes; Hot Filament CVD; Electroanalysis

3.6.1. Introduction

The extreme hardness and thermal conductivity of CVD diamond determines its main application in cutting and anti-wear parts, as also in heat sinks for electronic and optical components. However, by doping this material, the range of applications can be appreciably widened, as it becomes electrically conductive. For a given film thickness, the conductivity of CVD diamond films can be tuned from 1×10^{-9} $\Omega^{-1}\text{cm}^{-1}$, for lightly doped films, to 100 $\Omega^{-1}\text{cm}^{-1}$, for heavily doped ones [97,184–186]. The conductivity value depends on the doping agent and its concentration, and also on the temperature and light exposure. Boron doping yields p-type semiconduction by introducing an acceptor energy level 0.37 eV above the valence band, while nitrogen or phosphorus doping yield n-type semiconduction [70].

Although the latter elements have been reported to successfully dope CVD diamond films [5, 6], boron is by far the most efficient doping agent due to its low charge carrier activation energy [77]. When heavily doped ([B] $>1 \times 10^{20}$ atoms/cm^3), CVD diamond becomes a conducting material or even superconducting if the temperature is low enough (~2 K) [97,184,187].

In 1987, Pleskov et al. [98] started to explore the electrochemical properties of doped CVD diamond, revealing the good electrochemical performance of the material. It can surpass other carbon and metallic electrode materials, in terms of electrochemical window and low background currents allowing the analysis of hard-to-detect analytes like nucleic acids [188,189]. In aqueous media, these are often not feasible to detect with noble metal electrodes due to the high background Faradaic currents originated from the oxygen and hydrogen evolution reactions (HER) [71,123]. The superior electrochemical performance of CVD diamond is enabled by good responsiveness for many redox analytes without pretreatment, very good microstructural stability at extreme cathodic and anodic potentials and high current densities, as well as by resistance to fouling due to the weak adsorption of polar analytes on its non-polar hydrogen-terminated surface [120,189,190].

Although macroelectrodes based on boron doped diamond confer all these properties, many applications request a significantly smaller size of the electrode to be used for localized measurements. The spatially resolved microanalysis can provide essential information in such areas as plant physiology, biotechnology, medicine and corrosion studies. Ultramicroelectrodes (UMEs), which are defined for having at least one dimension <25 µm, can be efficiently used for these purposes [8]. Employment of UMEs enables hemispherical diffusion which alows: i) high current density, ensuring a higher signal to noise ratio; ii) low dependence on hydrodynamic conditions, because sensing is done within the diffusion layer; iii) a short equilibration time after applying a potential step; iv) the possibility to work in high resistive media, due to the limited ohmic drop within a small area close to the electrode [191]. The disadvantage is the small total current which can be a problem particularly for trace detection [8]. UMEs also exhibit sigmoidal voltammetric curves, which is possible due to the steady-state hemispherical diffusion to the microscopic area of the microelectrode [8].

Although boron doped microcrystalline diamond (B-MCD) may seem more appropriate for electrochemical applications due to its higher phase purity, the use of boron doped nanocrystalline diamond (B-NCD) is more adequate since nonporous very thin films can be grown. This ensures two important features at once: the smallest possible size for the UME and the necessary insulation that avoids the analytes from reacting with the substrate material, as it may happen with B-MCD coatings [183].

The research concerning CVD diamond UMEs began only about one decade ago with the work of Cooper et al. [118], by growing single diamond crystallites and B-MCD films on tungsten tips. Since then, several works based on doped microcrystalline diamond as an electrode material have been carried on [126,192], but the first work concerning the use of B-NCD on UMEs as a suitable material for electrochemical applications appeared only on 2004, by Soh et al. [193], who used a microwave plasma enhanced CVD reactor to grow B-NCD on microelectrode arrays and sharpened tungsten microprobes. A reversible behavior and high sensitivity as well as a large potential window of 3 V for the detection of $Fe(CN)_6^{4-/3-}$ in KCl was revealed.

Diamond UMEs are possible solutions in a variety of ways. Due to the biocompatibility of diamond, these microprobes can be used in biological systems for *in vivo* detection,

such as to clarify intimate details of mechanisms of the processes occurred in living cells with micro-resolution, or for neurotransmitter monitoring in the brain [120,128,194]. They can also be used for measurements on fast electron transfer reactions in high resistive media, and as amperometric detectors in scanning electrochemical microscopy (SECM) and capillary electrophoresis [119,195,196].

The main goal of the present work is manufacturing robust inert amperometric UMEs based on tungsten micro-tip coated with boron-doped nanocrystalline diamond film as a working surface.

3.6.2. Experimental Details

3.6.2.1. Tip preparation

Sharp tungsten tips were obtained through the use of the lamellae drop-off technique [172,197–199]. Tungsten wires with 150 µm radius where electrochemically etched in a 3 M NaOH solution under a potentiostatic polarization (Figure 3.16). The typical current for an applied voltage of 3 V was ~2 mA with a mean sharpening time of 10 minutes.

The electrochemically assisted dissolution causes the tungsten wire to form a successively thinner neck, until the lower part of the wire falls off, leaving a sharpened tip behind [200]. The obtained tungsten tip was then ultrasonically seeded in a nanodiamond (3-5 nm) powder suspension for 1h, and ultrasonically cleaned in ethanol afterwards to release the residual diamond powder from the W tip.
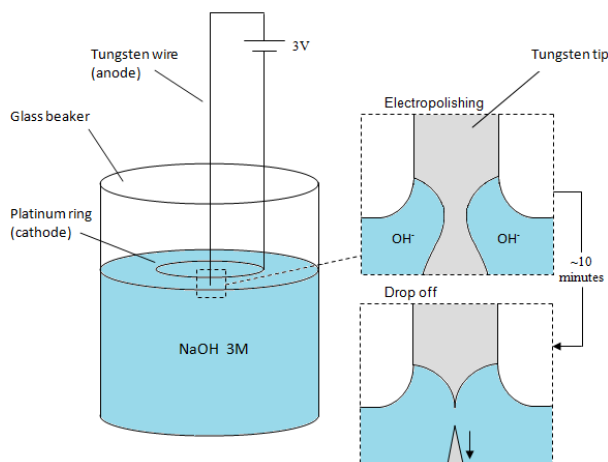
Figure 3.16 - Experimental setup for electrochemically etching the tungsten wires.

3.6.2.2. Growth of CVD nanocrystalline diamond on the sharpened W tips

The deposition of B-NCD films was performed in a hot filament chemical vapour deposition (HFCVD) reactor. The growth of CVD boron doped nanocrystalline diamond (B-NCD) on the W tips was attained by using 4 tungsten filaments (125 μm radius) previously carburized at 2300 ºC for 15 minutes in a methane+hydrogen atmosphere with a CH_4/H_2 ratio of 0.04 under a pressure of 100 mbar in the reaction chamber. During the growth period the CH_4/H_2 ratio was the same. The boron doping was performed by dragging a B_2O_3+ethanol (15000 ppm B/C) solution with argon gas through a bubbler. The W tips were positioned vertically 5 mm below the filaments. No mask was used, and the B-NCD films typically covered an extension that starts on the tip apex and ends a little below (~400 μm) the conical-like region. The filament and the CH_4/H_2 gas flow ratio were maintained constant and equal to 2350 ºC and 0.07, respectively, while the $(Ar+B)/H_2$ ratio varied within the range of 0.06-0.21. The wire temperature was kept constant at 670º C, thermocouple controlled, at a distance of about 500 μm from the tip. The total system pressure in the reaction chamber was 50 mbar and the deposition varied between 30 minutes and 3 hours.

3.6.2.3. Tip insulation

The formed microelectrode must have open only the active surface of micro-tip. The rest of the surface of tungsten wire should be electrically insulated avoiding contact of the metal with the analyte. The insulation of the CVD diamond covered tips was carried out using epoxy resin which wrapped the whole body of the tip leaving just the final apex exposed. The application of the insulator was performed using a manual micrometric controlling device, and was observed by means of an optical microscope, which allowed a precise dragging of the wire trough the epoxy resin. In this way it was ensured that the uncovered apex had the desired geometry and adequate size for the electrode to be considered an UME (Figure 3.17). The assembly allowed a precise coating with the epoxy resin, therefore avoiding the risk of damaging the B-NCD

deposited tip. After the insulation process, the resin was cured for several hours at room temperature.
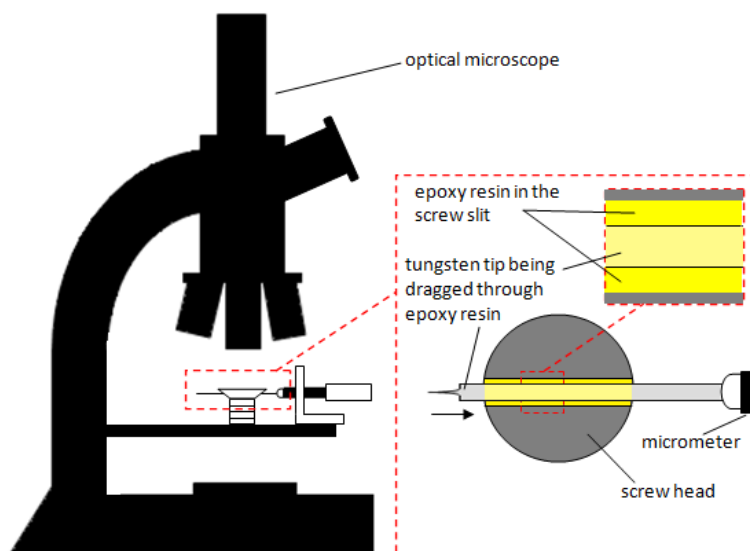
Figure 3.17 - Homemade UME insulating device.

3.6.2.4. Morphological, chemical and electrochemical characterization

The morphological and microstructural characterization as well as the measuring of the film thickness after breaking the tips was carried out using scanning electron microscopy (Hitachi S4100, Hitachi SU70). The detection of diamond, graphitic phases and residual stress estimation was performed by micro-Raman spectroscopy using a 50 mW laser of 325 nm wavelength. For the electrochemical characterization, cyclic voltammetry tests were performed to evaluate the chemical inertness and the electrochemical potential window of the electrode, by using an electrochemical cell in a Faraday cage. The cell consisted of a three electrode arrangement with the UME as working electrode, a platinum auxiliary electrode and a SCE reference electrode. The electrolyte was a 0.05 M NaCl (Merck) solution and the measuring equipment consisted of a potentiostat Autolab PGSTAT302N (EcoChemie, Netherlands). During the cyclic voltammetry, a potential range between -1.5 V and 2 V (vs. SCE) was used with a sweep rate of 100 mVs^{-1}.

3.6.3. Results and discussion

3.6.3.1. Preparation of the tungsten tips

In order to obtain a basis for amperometric UMEs with the desired shape and size it is essential to customize the electropolishing of tungsten wires. There are 3 geometric factors that determine the UME shape: aperture angle (γ), tip radius (R) and length of the sharpened region (L) (Figure 3.18a). These parameters can be tuned by controlling the positioning of the W filament in the electrolyte solution, the threshold current value and the cutoff current value. A proper adjustment of the above referred factors allows the production of nanosized and well-shaped tips like the one demonstrated in Figure 3.18b. The average dimensions of the tungsten tips after the electropolishing process are indicated in Figure 3.18c. An example of an as-prepared electropolished tungsten tip is shown if Figure 3.19a-c.

Average tip dimensions			
R (nm)	γ (°)	L (μm)	D (μm)
50	15	270	250
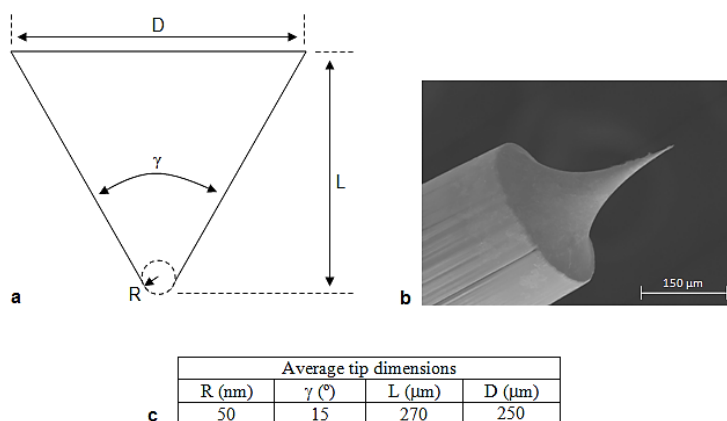
Figure 3.18 - a: relevant geometric parameters; b: average sized tungsten tip sharpened electrochemically in a 3 M NaOH solution; c: average dimensions of the tips after electropolishing.
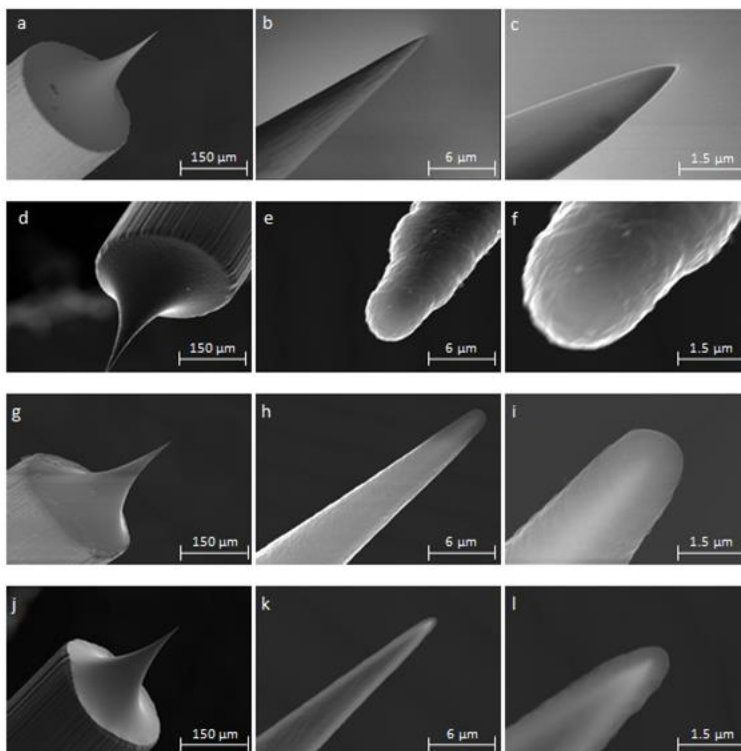
Figure 3.19 - As-prepared and B-NCD coated tungsten tips; a-c: uncoated sample; d-f: sample W1 coated with the thickest B-NCD film, (Ar+B)/H_2 = 0.06; g-i: sample W2, (Ar+B)/H_2 = 0.21; j-l: sample W3 coated with the thinnest B-NCD film, (Ar+B)/H_2 = 0.36.

3.6.3.2.   B-NCD deposition

The second step of creating the electrode is the deposition of a conductive diamond based coating on top of the W tip. Continuous, electrically conductive, B-NCD films with thicknesses of ~250 nm were grown on sharpened tungsten wires during 30 minutes of deposition time. Recent works in this area report growth periods of less than 3 hours to grow conducting B-NCD continuous films with similar film thicknesses, on tungsten tips [129,183]. However these deposition times are possible only by making use of bias enhanced nucleation (BEN) systems that improve the growth rate. For unbiased depositions, like in this study, the same works report growth periods of 7-10 hours.

The use of Ar as dragging gas for boron is another novelty of the present work. The study of the effect of the (Ar+B)/H_2 ratio on the microstructure and thickness of the B-NCD films grown on sharpened tungsten filaments started with large deposition times that where progressively shortened, as it became clear that the nucleation period on the

W tips was very short. Therefore the film thickness was excessive for the purpose of nanometric UME tip radiuses. The first B-NCD films grown on tungsten tips had a growth time of 180 minutes, yielding films as thick as the one of sample W1 (~1.3 µm) (Figure 3.19d-f). This diamond layer was grown with an (Ar+B)/H_2 ratio of 0.06 and despite its nanocrystalline morphology, the film reveals a rather rough surface. Raising the (Ar+B)/H_2 ratio to 0.11 for sample W2 (Figure 3.19g-i) and 0.21 for sample W3 (Figure 3.19j-l) enabled a considerable smoothening of the surface, as it can be seen by the total absence of bulges and other irregularities. This might be a consequence of the dilution of the hydrogen gas by argon, enhancing the secondary nucleation phenomena on the growing surface and therefore the deposition of NCD [56,201]. Increasing the (Ar+B)/H_2 ratios also implicates a larger amount of boron in the reaction chamber and supposedly in the B-NCD films. In consequence, a larger number of defects is introduced in the film, what may also enhance the growth of NCD over microcrystalline diamond (MCD) [202]. Additionally, diluting the hydrogen gas in the reaction chamber with (Ar+B), has an inverse effect on the deposition rate of B-NCD. Hydrogen is the main agent responsible for promoting a high deposition rate in the system, as it creates active growth sites on the growing surface, where the addition of CH_3 radicals occurs. Therefore the growth rate decreases as the hydrogen dilution increases. Actually, the slower rate is an advantage since it leads to the growth of very thin nonporous electrically conductive films. This was evidenced by raising the (Ar+B)/H_2 ratio progressively from W1-W3, which resulted in a corresponding growth rate lowering from ~450 nm/h for W1 to ~320 nm/h for W2 and to ~230 nm/h for W3. The latter had a deposition time of only 90 minutes, and still, the film grew to a final thickness of about 350 nm. In practice, this means that even with this short deposition time the exposed apex of the UME has a diameter of about 700 nm, due to the hemispherical geometry. Therefore the deposition time was even further reduced to 30 minutes, maintaining the (Ar+B)/H_2 ratio of 0.21, which yielded B-NCD films with thicknesses of about 250 nm.

Another noticeable effect of varying the (Ar+B)/H_2 ratio is on the structural quality. For undoped NCD the Raman spectrum shows the diamond peak at 1332 cm^{-1}, and four extra features at 1150, 1350, 1480 and 1550 cm^{-1}. The 1350 and 1550 cm^{-1} peaks are the D and G bands of amorphous carbon, while the peaks at 1150 and 1480 cm^{-1} have

been attributed to transpolyacetylene (TPA) present in the NCD grain boundaries [203,204]. With the increase of the (Ar+B)/H_2 ratio, the diamond peak at 1332 cm^{-1} on the Raman spectrum became broader and less intense (Figure 3.20). Also worth mentioning is the shifting of the 1332 cm^{-1} peak from its original position to lower wave numbers, when the boron content is increased, which has been observed several times [205–208]. This is attributed to the intrinsic tensile stress that the electronic holes introduced by boron defects induce in the B-NCD film [209]. However, in our work there was a slight shifting towards higher wave numbers. Since diamond films usually present residual stresses extrinsically induced by the difference in the coefficients of thermal expansion between the substrate and the film [202], this upper shift of the diamond peak may result from the fact that the extrinsic stress was greater than the intrinsic stress caused by the boron impurities.
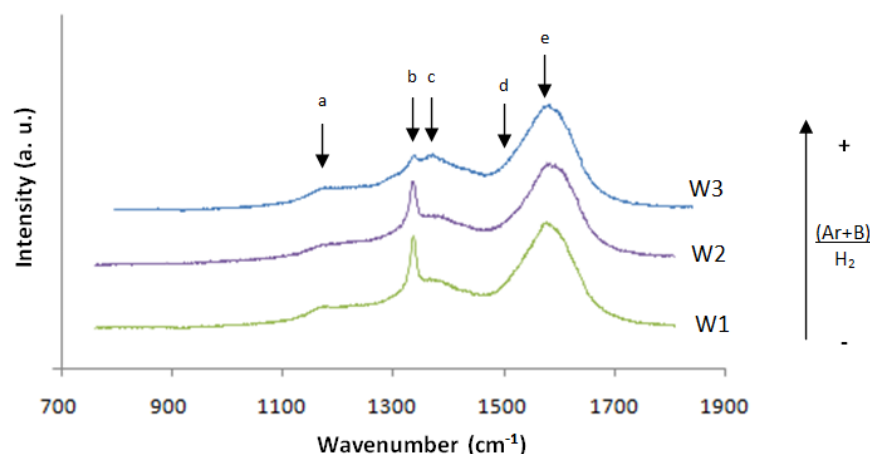
Figure 3.20 - Raman spectra of the boron doped nanocrystalline diamond coated samples revealing the influence of boron doping on the intensity of the 1332 cm^{-1} diamond related peak. a, d:1150 and 1480 cm^{-1} bands attributed to transpolyacetylene; c: 1350 cm^{-1} band attributed to the disordered carbon; e: 1550 cm^{-1} band attributed to graphite.

3.6.3.3.   Fabrication of UME

The final step towards the UME assembly is the insulation of the B-NCD deposited tungsten wire leaving only the sharp apex exposed. Several methods were tried including a two-step full tip coverage with nail varnish and afterwards removal with

acetone [18]. In our case it did not offer a very good control of the exposed tip geometry and caused the damage of various B-NCD coated tungsten tips. Another insulation method consisted of a B-NCD coated tip passing through a drop of epoxy resin. Improving this method allowed us to have a very good control over the extension of the insulation coat, with the aid of an optical microscope and a micrometer, as described in Figure 3.17. Insulating the B-NCD coated tungsten tips through this method avoids the damaging of the tips and also allows a very well defined geometry for the exposed extremity of the probes, which ensures that the UME's apex is the only electroactive area.

3.6.3.4. Electrochemical characterization

The electrochemical response of the UMEs was tested by cyclic voltammetry in a 0.05 M NaCl solution using a coated tip grown in conditions similar to those of sample W3. The first sweep demonstrates only one oxidation peak starting at about 1 V (Figure 3.21). The polarization to this potential range is accompanied with the evolution of gas bubbles on the tip of the electrode as it can be seen in Figure 3.22a. Thus the only oxidation process, which is related to the water oxidation and evolution of oxygen, occurs on the diamond coated tip at relatively high polarization. This fact confirms a wide electrochemical window of the electrode in direction of positive potentials. In the reverse scan one response at low potential can be observed (Figure 3.21). It becomes visible at about 0 V and is associated with the reduction of oxygen dissolved in the electrolyte. However the kinetics of this process is quite slow showing low currents close to the background level. The second reduction process appears at higher polarizations at about -1.25 V and can be ascribed to the hydrogen evolution. Thus the potential window of water stability on the developed electrode is about 2.25 V that is 1 V higher than the thermodynamic stability range of water.
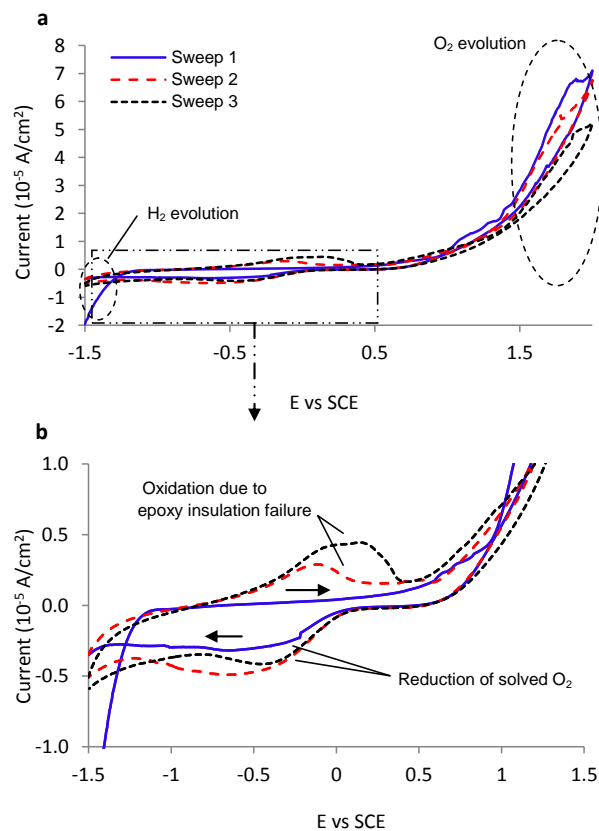
Figure 3.21 – Cyclic voltammograms performed in a NaCl 0.05M solution; a: first 3 sweeps, revealing the early fouling of the epoxy insulation; b: box detail, showing the tungsten oxi-redox reaction with the electrolyte solution.

On the following sweeps, an additional anodic peak arises at about 0 V. One possibility to consider for the origin of this feature would be the interaction of the electrolyte with some remaining sp^2 carbon on the electrode surface. It can be also related to electrochemical activity on the tungsten surface out of the area covered with the B-NCD film. However, the latter possibility seems more probable considering that there is no bubble formation on the diamond coated area, which starts from the tip apex and ends a little below the conical-like region, as it can be seen in Figure 3.22. This interaction between the metal and the analyte was probably caused by weak barrier properties of the epoxy coating used as insulation. This suggestion can be confirmed by the fact that the formation of bubbles on the following scans is observed only out of the active tip (Figure 3.22b), on the tungsten wire which was not coated with diamond and was presumably protected by the epoxy. Therefore it is quite probable that the additional

oxidation peak originated from the electrochemical reaction on the tungsten substrate not covered with diamond film.
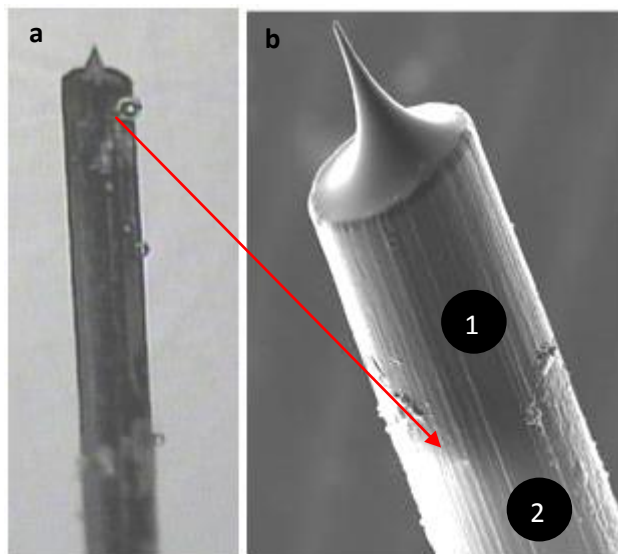
Figure 3.22 - UME before and during the cyclic voltammetry; a: polarized UME after some sweeps, showing a large electrochemical activity, starting to occur on the edge of the B-NCD coat and beyond, where the W substrate becomes visible; b: SEM image with detail of the transition between the B-NCD coated (1) and uncoated (2) regions.

3.6.4. Conclusions

In the present work the amperometric ultramicroelectrode based on the conductive nanostructured boron-doped diamond film was fabricated. Electropolished tungsten tips where coated with non-porous B-NCD films in very short time periods (30 min) by using the hot filament CVD method. The newly tested boron doping process using Ar as dragging proved to be effective to grow such thin non porous conducting B-NCD films. The highest deposition rate achieved was 450 nm/h for a $(Ar+B)/H_2$ ratio of 0.06 and the lowest rate was obtained for a ratio of 0.21 maintaining all the other parameters constant. $(Ar+B)/H_2$ ratios greater than 0.11 yielded smooth films with no superficial irregularities. The Raman spectrum revealed a crystallinity reduction of the B-NCD films with increasing boron content and a slight shifting to higher wavenumbers due to the extrinsic stress of the films. The fabricated UME provides a wide electrochemical

window of 2.25V in water-based electrolyte. However the insulation of the tungsten wire must be improved in order to provide long service life of the developed electrodes. Further research is being carried out, involving effective boron concentration measurement by Secondary Ion Mass Spectrometry (SIMS) and alternative improved insulation methods.

Acknowledgements

3.7. Microscopic studies on the interface between a tungsten substrate and boron doped diamond film on the nucleation stage

CVD polycrystalline diamond can be grown with diverse morphologies from microcrystalline (>1 μm) to ultrananocrystalline (<10 nm). For electrochemical purposes boron doped microcrystalline diamond (B-MCD) is more adequate because of its easily-accomplished high phase purity. However, the use of boron doped nanocrystalline diamond (B-NCD) also has advantages, since nonporous very thin films can be grown. This ensures two important features at once: the smallest possible size for the ME and the necessary insulation that avoids the analytes from reacting with the substrate material, as it may happen with B-MCD coatings [183].

The size of diamond MEs is limited by two factors: the dimensions of the substrate – usually an electropolished metallic wire –, and the thickness of the B-NCD film. For the former case, it is possible to obtain metallic tip radiuses with less than 10 nm, but for the latter it is not that simple, as was seen in the previous section. The deposition of NCD films on substrates other than diamond itself implies the formation of an interfacial region between the substrate and the diamond film. In a study about the nucleation of diamond on silicon substrates Lin et al. have reported the formation of an interfacial region constituted by a β-SiC/amorphous carbon layer grown directly on a silicon substrate [210]. For deposition on carbide forming transition metals, like tungsten, Das and Singh have reported that the nucleation of diamond films occurs on the carbide layer, which is formed after the activated carbon gas source saturates the metal [211]. Besides being a size limiting factor, this interfacial region can also be property limiting since it mediates charge transfer between the substrate and the NCD coating. This evidences the relevance of characterizing this region and also the need to reduce its thickness as far as possible. Therefore, the deposition parameters have to be adequately adjusted to ensure that good quality NCD films are grown. By optimizing these size-limiting conditions, diamond MEs gain enhanced ability for electroanalysis in small volumes. The following work was aimed at solving these unknowns, and thin flat

substrates were used instead of the sharp W tips for the sake of easiness in handling the specimens for microstructural characterization.

3.7.1. Experimental

3.7.1.1. Substrate preparation

A tungsten sheet (0.05 mm thick, ABCR) was the substrate for B-NCD film deposition instead of the W wires. Such a choice relied on the properties of this metal. Tungsten has a good electrical conductivity, it is compatible with the gas phase chemistry used for the chemical vapour deposition and it can withstand the used temperature range (2100-2700ºC). An additional factor is that the tungsten carbide interface, which is formed between the tungsten from the substrate and the carbon from the gas phase, presents also a good electrical conductivity avoiding the existence of a resistive barrier between the diamond and the electrode core. The W sheet was polished with SiC sandpaper to remove the oxide layer and other impurities from its surface. Afterwards it was ultrasonically seeded in a nanodiamond powder aqueous suspension (grain size 3-5 nm) for 5 minutes and subsequently rinsed in water and ethanol during 30 minutes.

3.7.1.2. Film growth

A B-NCD thin film was grown on the tungsten sheet substrate, in a hot filament chemical vapor deposition (HFCVD) system with 6 tungsten filaments ($\varnothing$=250 μm, Goodfellow) as the heating source. The film was grown during a 15 min period with a filament temperature of 2300 ºC, substrate temperature of 700 ºC, CH_4/H_2 ratio of 0.05 and system pressure of 50 mbar. The boron doping was performed by dragging a B_2O_3+ethanol 3×10^{-3} M solution with argon gas through a bubbler, into the reaction chamber. The mass flows were 100 ml/min for H_2, 5 ml/min for CH_4 4 ml/min for the B dragging gas, argon.

3.7.1.3. Characterization

The microstructural characterization of the films was performed by SEM (Hitachi SU-70) and TEM (Hitachi 9000). The crystalline quality and structure were evaluated by UV μ-Raman spectroscopy (HORIBA JOBIN YVON HR800UV), using the line 325 nm from a He-Cd laser (KIMMON IK series) for surface excitation, to identify the different carbon sp^2/sp^3 phases incorporated in the coatings and to assess any residual stresses. Electron diffraction was used for lattice spacing determination. Furthermore, the elemental composition was mapped by Energy Dispersive X-ray Spectroscopy (EDS) and Electron Energy Loss Spectroscopy (EELS).

3.7.1.4. Sample preparation for TEM

After film growth the sample was immersed in a hydrogen peroxide (H_2O_2) P.A. 30% solution during several hours in order to dissolve the tungsten substrate. After this process the film was left floating in the solution and captured to a copper grid, where it stood still due to surface tension (Figure 3.23).
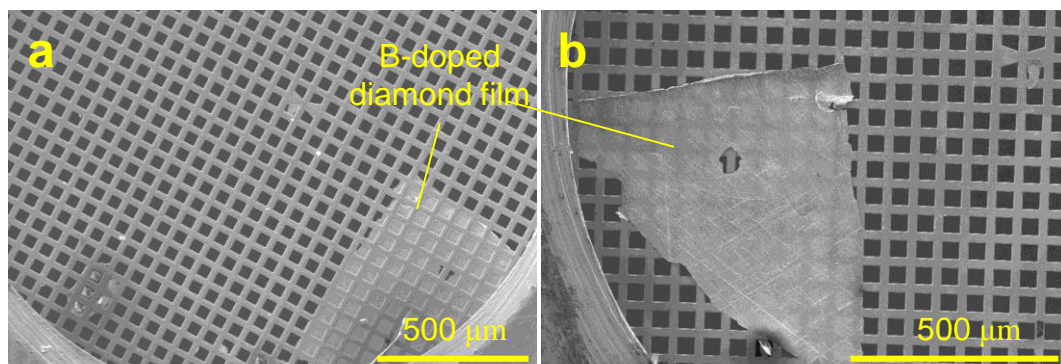
Figure 3.23 - Diamond thin film specimen after being captured by a SEM copper grid. a: growth side of the film; b: substrate side of the film.

3.7.2. Results and discussion

The attempt to grow a continuous B-NCD film grown on top of a tungsten sheet with a deposition time of only 15 min was successful. Despite its versatility, the HFCVD method is not suitable when high deposition rates are needed. For this work in

particular, this limitation was very useful since it allowed synthesizing a B-NCD film in the initial stage of growth. The morphology of the film is not of typical NCD (Figure 3.24a), which consists of agglomerates of diamond nanocrystallites, the so-called cauliflower structure (Figure 3.25). The observed morphology is faceted and is probably associated to a low nucleation density due to the short substrate seeding period. Nevertheless, this was considered to be necessary to reduce the presence of nanodiamond powder impurities. Furthermore, this slightly coarsened microstructure (medium grain size of ~70 nm) facilitates the characterization by TEM.
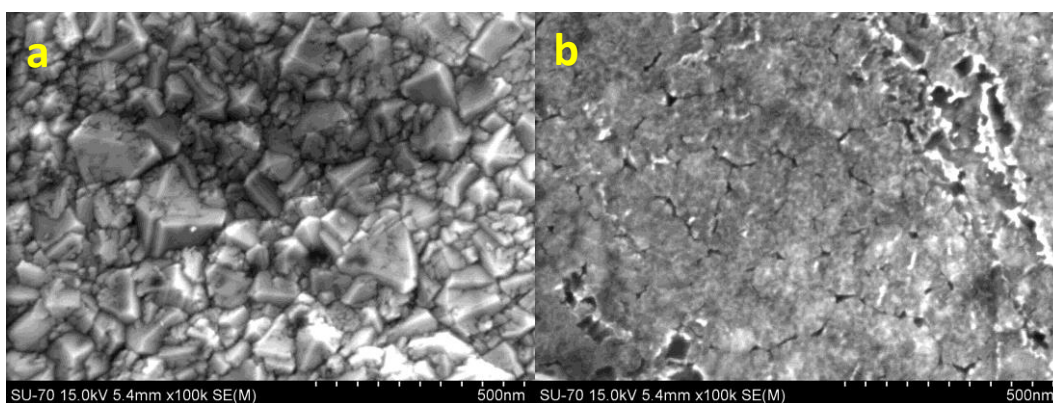
Figure 3.24 - a: Growth side of the film where its faceted structure can be observed; b: substrate side of the film.
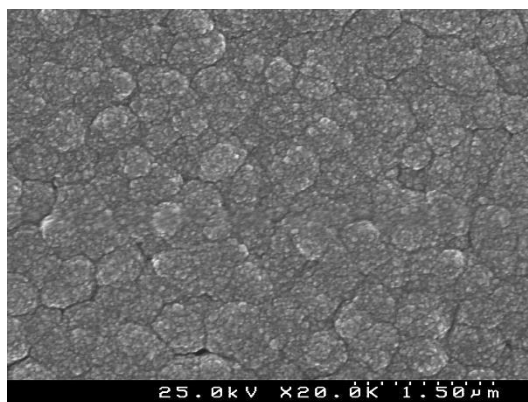
Figure 3.25 - Typical cauliflower structure of a NCD film.

From the growth side of the film it can be seen that among the diamond crystals there is some non-diamond material (Figure 3.24a). The substrate side reveals that the diamond crystals nucleate on top of an interfacial amorphous region (Figure 3.24b), which is

confirmed by the Raman spectrum. For undoped NCD the Raman spectrum shows the diamond peak at 1333 cm^{-1}, and four extra features at 1150, 1350, 1480 and 1550 cm^{-1}. The 1350 and 1550 cm^{-1} peaks are the D and G bands of disordered and ordered graphite, respectively, while the peaks at 1150 and 1480 cm^{-1} have been attributed to transpolyacetylene (TPA) present in the NCD grain boundaries [203,204]. The B-NCD presents a high crystalline quality as it can be observed by the intensity and small full width at half maximum (FWHM) of the diamond peak (Figure 3.26) and by the low intensity of the D and G bands, especially when considering it is a nanocrystalline film and has a very high density of grain boundaries (Figure 3.24a). A qualitative indication of the presence of boron atoms in the diamond film can also be observed in the Raman spectra by the shifting of the diamond peak to a lower wavenumber, at 1331.2 cm^{-1} [71]. Since carbon has 4 valence electrons and boron has only 3, the presence of this element will introduce an electronic hole available for electrical conductance and also implies a reduction in the bonding energy of diamond, which causes the lattice parameter to increase [75]. This relaxation effect induces an overall tensile strength on the films, which can be detected in the Raman spectra by the shifting of the diamond peak to lower wavenumbers.

The film was also characterized by EDS (Figure 3.27a-c). Besides carbon (Figure 3.27d) some residual silicon was identified (Figure 3.27e), from the polishing of the substrate with SiC abrasive paper. The electron diffraction pattern of the film (Figure 3.28) was indexed revealing an expansion of the interplanar spacing of the (111) planes by 0.43%, which is similar to a 0.3% lattice dilation reported by other authors [212]. This is in good agreement with the work of Pleskov and co-workers, which state that boron is preferentially incorporated in the (111) lattice, and at lower amounts in the (100) planes [71].
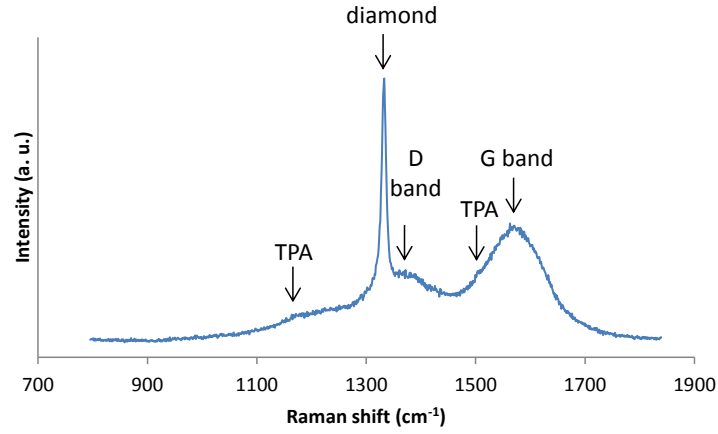
Figure 3.26 - Raman spectra of the B-NCD film showing its high crystalline quality.
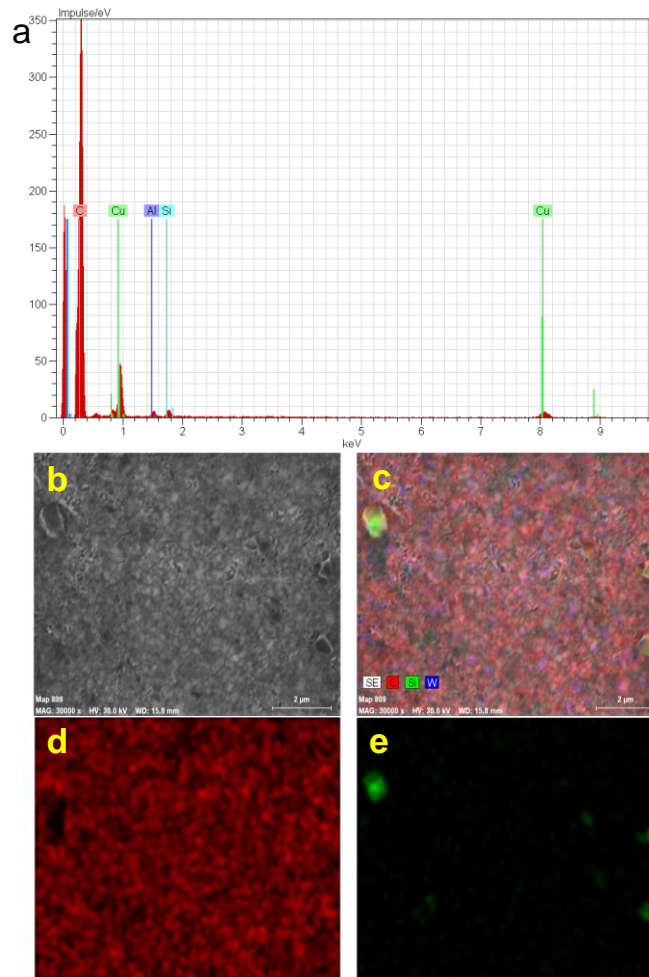
Figure 3.27 - EDS map of the B-doped film, where the distribution of carbon material and residual Si can be observed.
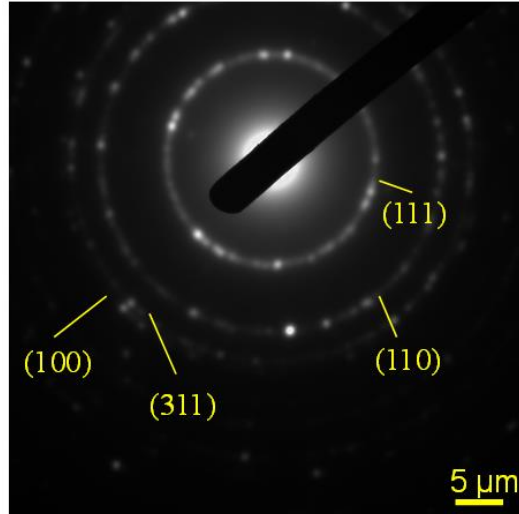
Figure 3.28 - Diffraction pattern of the B-doped nanocrystalline diamond specimen where it is possible to identify the most intense scattering plane families: (111), (110), (311) and (100).

The TEM micrographs in bright field mode exhibit some dark regions in a lighter matrix (Figure 3.29). These correspond to superimposed diamond crystals, where the electrons are scattered with more intensity than in the lighter regions. In these lighter zones some diamond crystals are observed, but there is mainly amorphous material, which can be identified in the dark field micrographs of the same area of the specimen. As an example, the central area from Figure 3.29 does not present a crystalline arrangement, regardless of the direction of the incident beam in the dark field mode (Figure 3.29c). It is possible that these regions correspond to amorphous carbon, or polyacetylene, which is known to exist in the grain boundaries of nanocrystalline diamond [203,204]. In some of these amorphous regions some lattice ordering was observed (Figure 3.30a and b), which as reported by Wurzinger et al. [212], may be due to a stabilizing effect of boron towards the growth of some crystalline graphite lamellae, that otherwise would be etched away by hydrogen. The mixed nature of diamond/amorphous material observed in this film is in good agreement with the works of Das et al. and Michaelson et al. [211,213], reporting the formation of superimposed layers of graphite, amorphous carbon and a mixed layer between amorphous carbon and diamond, which is where the nucleation of diamond starts. The B-NCD film presents some common defects already reported for diamond films [214], among which crystal twinning was the most commonly observed one (Figure 3.31). Although defects

are always naturally present, especially in polycrystalline films, the large difference between the thermal expansion coefficient between diamond and tungsten may have contributed for an increase of the defect concentration. These defects are especially important in what relates to the electrode kinetics. The oxidation and reduction reactions occur at the electrode-electrolyte solution interface. At this interface the electron-transfer is considered to be a tunneling of the electron between electronic states on the electrode and the states of the reactant. The tunneling probability is proportional to a distance, x, over which the electron is being transferred, and also to a β parameter that reflects the energy barrier height and the nature of the solvent/electrolyte medium between the states. Thereby, the electrode and the reaction kinetics and mechanism are influenced by the structure of the interfacial region, particularly the physicochemical properties of the electrode material [215]. Consequently, properties such as the microstructure, the density of defects and the electrical conductivity are important and the extent to which any one of these properties can affect a redox reaction depends intensely on the nature of the analyte [215].
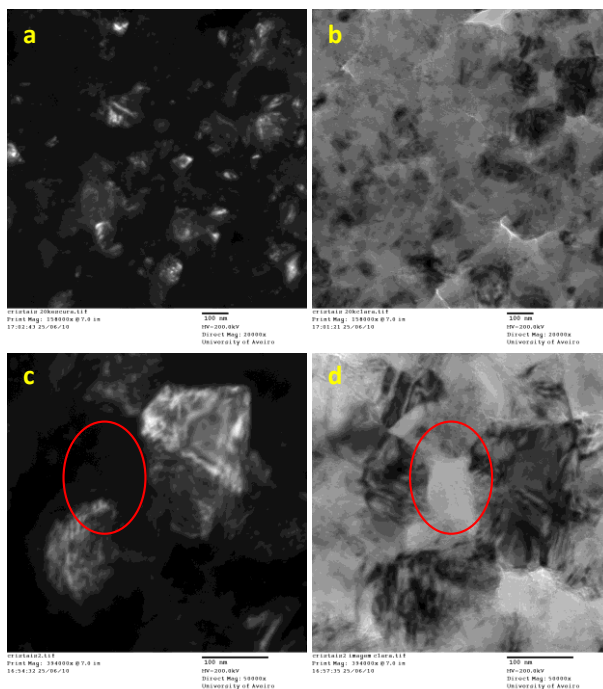
Figure 3.29 – Dark and bright field TEM images of the diamond film showing an overall view of the diamond film in a) dark field mode and b) bright field mode. The presence of amorphous material among the diamond crystals can be observed inside the red circle area in c) dark field mode and d) bright field.
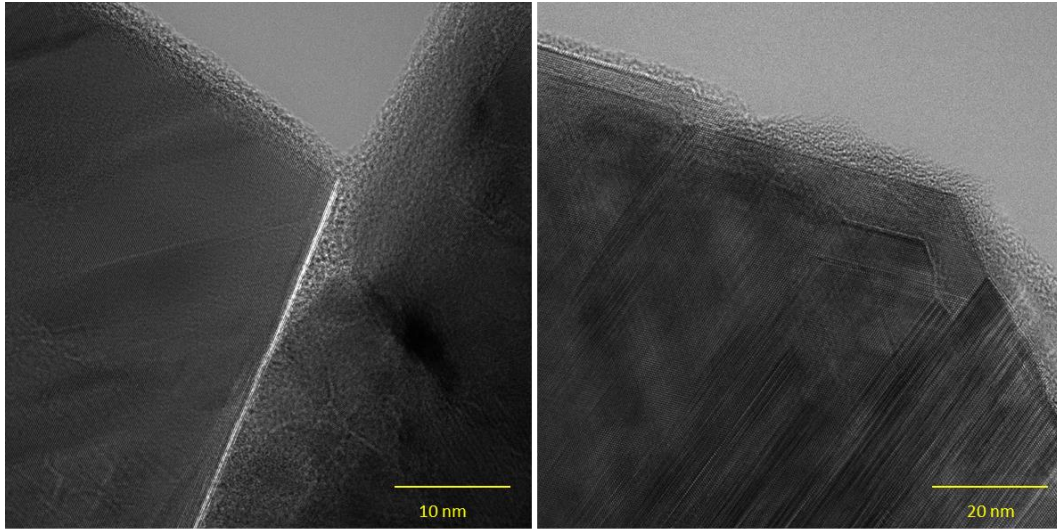
Figure 3.30 - High magnification view of the diamond crystals and some amorphous carbon in the outer grain regions.
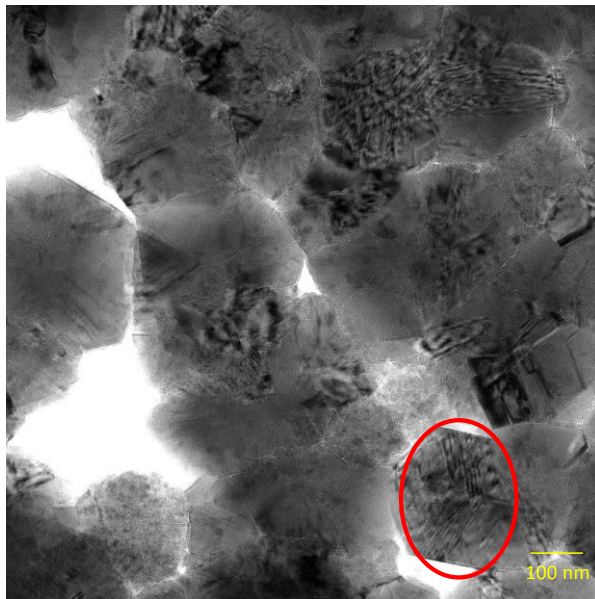
Figure 3.31 - Twinning defects in the diamond crystals.

The elemental composition of the film was determined by EELS as well as a qualitative evaluation of the uniformity of the boron distribution in the sample. The analysis was performed in different spots of the film with different microstructural characteristics, namely in grain boundary regions, in the interior of the grain and in amorphous regions. Information about the elemental composition of the film and the electronic structure can be obtained from the analysis of the core level excitations at the C 1s edge. It has been

reported several times that this excitation allows distinguishing between diamond and sp^2 bonded material like graphite or other forms of carbon. The C 1s excitation corresponds to electronic transitions from the C 1s core level to unoccupied states with C 2s-2p character. While for pure diamond these unoccupied states are solely of σ character, for sp^2 bonded carbon there are unoccupied π states at lower energies [216]. Therefore, the C 1s-π transition can be identified by a broad peak at 285.4 eV and the C 1s excitation to σ unoccupied states is characterized by peaks at 292 eV for graphite and 289 eV for the diamond edge [216]. On the EELS spectra from Figure 3.32 there are two main features which are attributed to graphite and diamond. The highest intensity peak was measured at 289.4 and is attributed to the carbon C 1s edge of diamond. The lower intensity broad peak at 282 eV was attributed to amorphous carbon forms due to the 3.4 eV shifting from the C 1s-π transition value. However, the edge of diamond does not present its usual shape [217], which might indicate the presence of graphite or the influence of other non-diamond carbon phases. At lower energies two extra features to the diamond spectrum appear at ~188 and ~157 eV, which have been attributed to boron 1s edge and to the L2 transition of silicon (from the SiC abrasive paper), respectively. The absolute quantification of the elemental composition of the film measured by EELS indicates a low boron percentage of 1.93% in the film. Although boron could be detected, the EELS spectrum in Figure 3.32 was measured in high resolution, with the smallest aperture. For lower resolution measurements (Figure 3.33), it is very hard to detect the signal from the boron atoms and in some regions of the film there is no signal at all, which indicates that this element is not uniformly distributed. In a recent ab initio study, Barnard and Sterneberg [218] report that the boron atoms are incorporated at preferential sites at the grain boundaries and nearby grain regions. Accordingly Wurzinger et al. report that the boron concentration in CVD diamond films grown by the HFCVD method is also inhomogeneous with higher boron concentrations in outer grain zones [212].
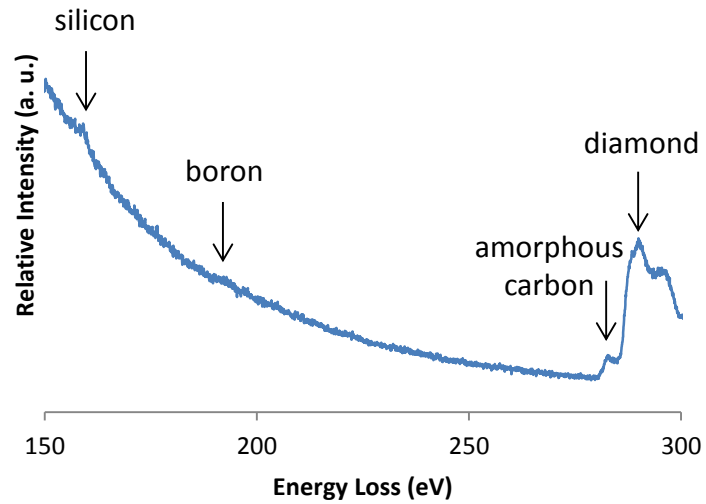
Figure 3.32 - EELS spectrum in high resolution showing the diamond edge, and three other features at 157, 188 and 282 eV, corresponding to the L2 silicon edge, the boron edge and non-diamond material, respectively.
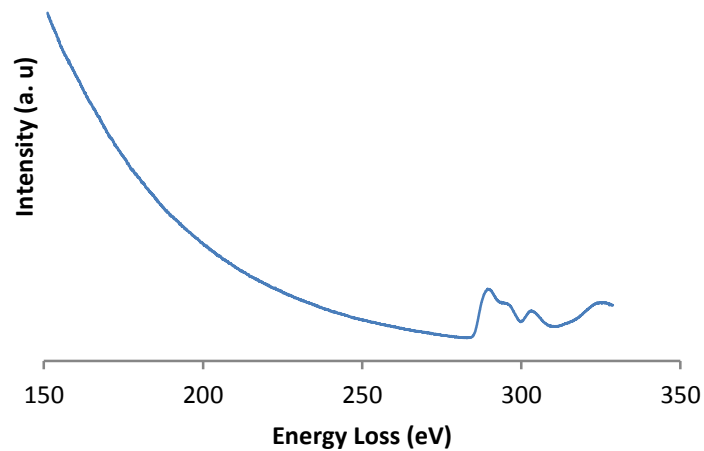
Figure 3.33 - EELS spectrum of the film using the second widest TEM aperture, where no sign of the boron can be measured.

3.7.3. Conclusions

In this work a B-NCD film in the nucleation stage was grown and characterized. The Raman spectra revealed the crystalline quality of the film. Boron was identified by a shift in the diamond peak of the Raman spectra and by a 0.43% expansion of the (111) lattice. The TEM observation revealed the presence of amorphous material among the diamond nanocrystallites. By comparing the same areas in the bright field and in the dark field mode, and it was also possible to identify different kinds of defects such as crystal twinning and dislocation lines. The EELS spectrum allowed detecting the presence of the diamond edge at 289 eV and also of non-diamond material. Boron was also detected in small amounts, with a concentration of 1.93% of boron in the film and was found to present a nonhomogeneous distribution.

This study of the tungsten/diamond interface allowed the detailed observation of the diamond crystallite microstructure and identify the presence of boron right from the initial stages of growth. This permitted evaluating the minimum deposition time needed to effectively establish a diamond film coverage on top of the interfacial layer with amorphous material. Adding to the knowledge acquired in section 3.3, this work was useful to understand the evolution of diamond film growth and contributed for the learning on how to fabricate diamond microelectrodes with enough purity and reproducibility of behavior, enabling the work to step up from simple voltammetry measurements without a specific target, to fully functional sensors with real applicability that can constitute a valid technological solution.

3.8. On the improvement of the electrochemical behavior of boron doped diamond microelectrodes

On section 3.3, BDD was grown on top of tungsten sharp wires with a focus on the diamond films alone, targeting the fabrication of an object that could truly be called a microelectrode from the standpoint of physical dimensions but relegating the electrochemical behavior to second plan. This section presents a short overview of the route that was adopted to fabricate diamond microelectrodes with scientific applicability, especially in the field of corrosion monitoring.

The selection of growth conditions for boron doped CVD diamond was developed following the feedback from electrochemical experiments done with diamond MEs produced using different parameters. The initial target was defined by the available literature on similar works. Although it is quite easy to find seemingly controversial information, a general trend can be drawn on properties such as the potential range of water stability, capacitive currents and information regarding kinetics for various redox couples. A work from 1995 named "Cyclic Voltammetric Studies of Charge Transfer Reactions at Highly Boron-Doped Polycrystalline Diamond Thin-Film Electrodes" [219], among other important ones [220–222], provides a good example of what is to be expected, electrochemically speaking, from the growth of high quality boron doped diamond films.

Figure 3.34 gives an indication of the range of methane-hydrogen proportion, temperature, and pressure conditions, around which much labor was done to progressively refine the electrochemical behavior of the diamond microelectrodes presented in this work. More important than the growth conditions *per se* was the establishment of strict procedures in every step of microelectrode fabrication. From these, an important mention has to be made about the difficulty that is coating sharp tungsten wires with diamond by HFCVD. This technique is very well suited for large scale depositions and allows versatility like no other. However, for microscale depositions, it is extremely demanding. Considering a deposition area of a few square centimeters, it is easily assumed that by setting all parameters constant and ensuring they remain so, during the deposition time, the same outcome must be observed most

of the times, if not all. This proposition does not hold for deposition at the microscale and a great deal of care must be taken to fairly ensure that the nearly invisible sharp tungsten wires are again and again positioned in the exact same region of the substrate holder. The representation of the HFCVD in Figure 3.35, schematically shows the care developed in the positioning and alignment of the sharp tungsten wires relatively to the expected gas flow inside the reaction chamber. This is a vital procedure if any conclusion is to be drawn from varying the growth parameters, and for achieving reproducible results. Then, after the growth period is completed and the system is almost cooled to room temperature, a good deal of luck is needed for the diamond coated MEs not to be destroyed by the collapse, upon cooling, of the fragile tungsten carbide filaments that served as thermal activation source for the gas.
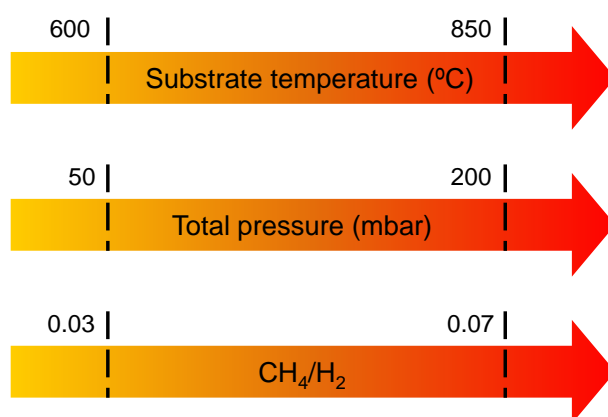
Figure 3.34 – Parametric window studied for boron doped CVD diamond growth.
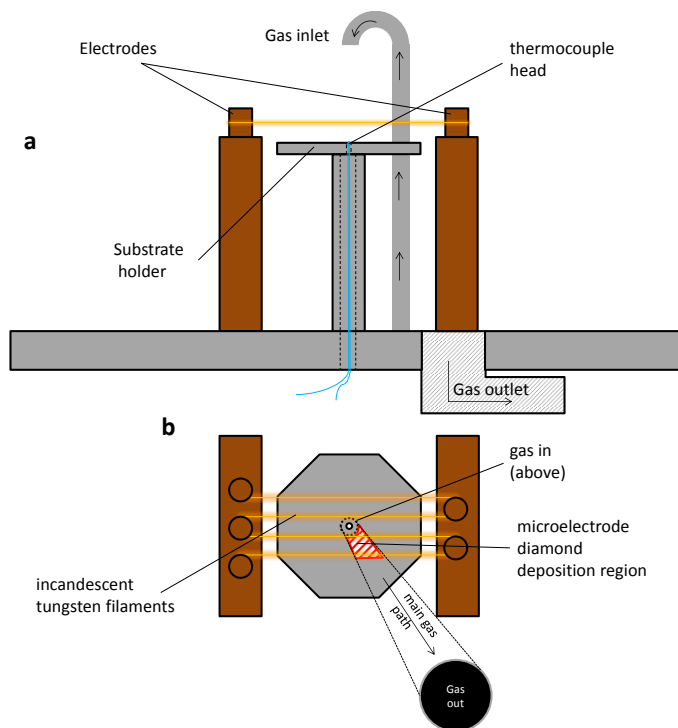
Figure 3.35 – CVD reactor showed in detail from a) front view; b) top view evidencing the growth region of diamond coatings on sharp tungsten wires (dashed red zone).

Nevertheless, Figure 3.36 and Figure 3.37 confirm that the task was possible and the difficulties were overcome. They provide microstructural and electrochemical information about the typical behavior of the diamond microelectrodes fabricated in this work, in different solutions of 50 mM NaCl, 10 mM $K_3[Fe(CN)_6]$ + 10 mM $K_4[Fe(CN)_6]$ in 50 mM NaCl and 1 mM ferrocenemethanol in 50 mM NaCl.

The $Fe(CN)_6^{3-/4-}$, usually an outersphere redox couple, is known to be very sensitive to carbon surfaces, displaying an innersphere electron transfer instead. Conversely the electron transfer of $FcOH^{0/+}$ occurs at the outersphere.

Although all the four microelectrodes indicated in Table 3.3, Figure 3.36 and Figure 3.37 have a similar behavior regarding the different solutions, these figures can give an indication of the influence of both the microstructure and the boron doping level in the electrochemical behavior.

Figure 3.36 (microelectrodes A and B) concerns microelectrodes with diamond films grown at low pressure (50 mbar), while Figure 3.37 (microelectrodes C and D)

corresponds to diamond growth at a higher pressure (180 mbar). A and B exhibit diamond of larger grain size (sub-micrometric) in comparison to C and D (nanometric).

A was grown with boron concentration (in solution) of 2000 ppm, while B had a boron concentration of 10000 ppm. When tested with the $Fe(CN)_6^{3-/4-}$ redox couple, although both MEs exhibited slow electron transfer kinetics, B shows a more reversible behavior and a symmetry between the anodic and cathodic waves, most likely deriving from its higher boron content.

Now, comparing the effect of the grain size, A and B show a higher catalytic activity towards hydrogen and oxygen evolution, than C and D, which exhibit water stability ranges of more than 4 V. Since C and D are nanocrystalline, it would be reasonable to assume that because of their higher densitiy of grain boundaries, the water electrolysis reactions (which proceed by an innersphere mechanism with adsorption of intermediates) would be favored, in comparison to A and B. Conversely, no particular enhancement of adsorption seems to occur, since hydrogen and oxygen evolution progress more slowly at C and D. However, the behavior of all four electrodes towards the $FcOH^{0/+}$ couple indicates that the redox reaction proceeds in a very similar way for the four microelectrodes showing quasi-reversible electron transfer, which suggests that charge transfer is not hindered in any of the microelectrodes. This and the fact that in all probability NCD can provide more adsorption sites for water electrolysis, suggests that different conductivity mechanisms are in play, depending on the distribution and type of surface states. The contribution of each to redox reactions will depend on the nature of the analyte species.

Hence, the growth optimization of the BDD films based on the feedback from the electrochemical behavior of the MEs, allowed the fabrication of microelectrodes with wide potential window and reasonably fast electron transfer kinetics. These were then used in their unmodified state and also with surface modification with heteroatoms other than hydrogen (O, F), in order to attempt specific measurements, namely of oxygen (sections 4.3 and 4.4) and pH (section 4.5). The detection of metal ions was also attempted with limited success, both with as-grown (section 4.3) and modified (not shown) MEs.

Table 3.3 – Selected microelectrode growth conditions.

Microelectrode	H_2 (ml/min)	CH_4 (ml/min)	Ar+B (ml/min)	Substrate temperature (^{0} C)	Pressure (mbar)	[B] in solution (ppm)
A	100	5	4	800	50	2000
B	100	5	4	800	50	10000
C	100	5	4	700	180	2000
D	100	5	4	700	180	6000
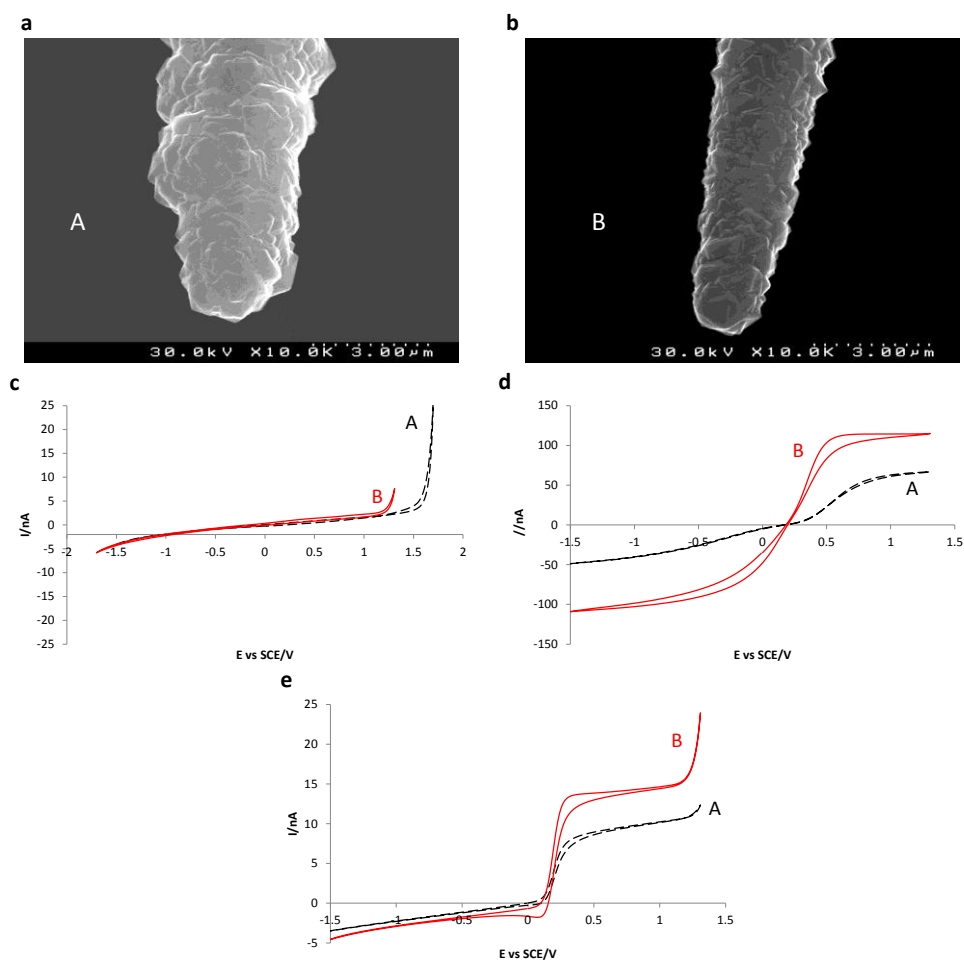
Figure 3.36 - Microelectrode A and B showing a-b) surface morphology; c) polarization in 50 mM NaCl, 100 mV/s vs SCE; d) polarization in 10 mM $K_3[Fe(CN)_6]$ + 10 mM $K_4[Fe(CN)_6]$ in 50 mM NaCl, 100 mV/s vs SCE; e) 1 mM ferrocenemethanol in 50 mM NaCl, 100 mV/s.
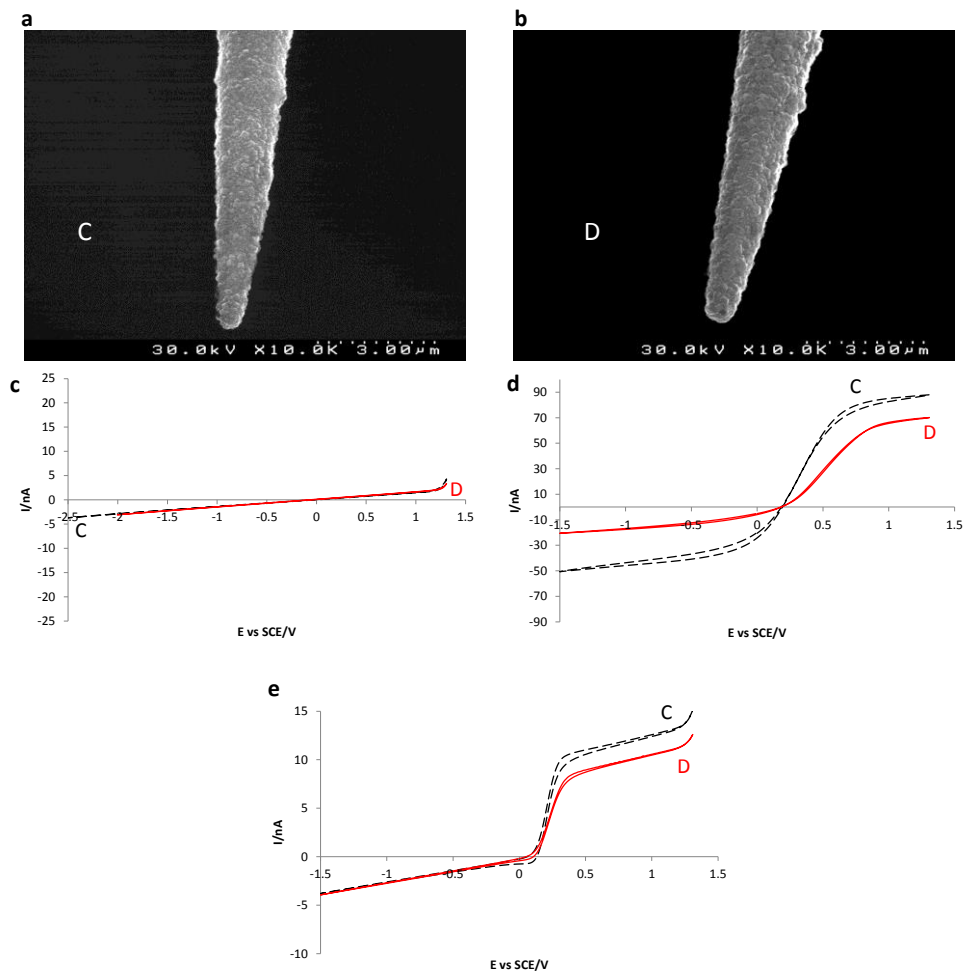
Figure 3.37 - Microelectrode C and D showing a-b) surface morphology; c) polarization in 50 mM NaCl, 100 mV/s vs SCE; d) polarization in 10 mM $K_3[Fe(CN)_6]$ + 10 mM $K_4[Fe(CN)_6]$ in 50 mM NaCl, 100 mV/s vs SCE; e) 1 mM ferrocenemethanol in 50 mM NaCl, 100 mV/s.

4. Diamond microelectrodes as probes for studying corrosion

4.1.   Corrosion of metals in aqueous solution

The corrosion of metals is driven by their thermodynamic instability in the presence of humidity. Figure 4.1 represents an elementary corrosion cell where the oxidation of a metal, M, to its ionic form M^{m+} on the anodic site is coupled to the reduction of the species X^{x+} to X on the cathodic sites [223].
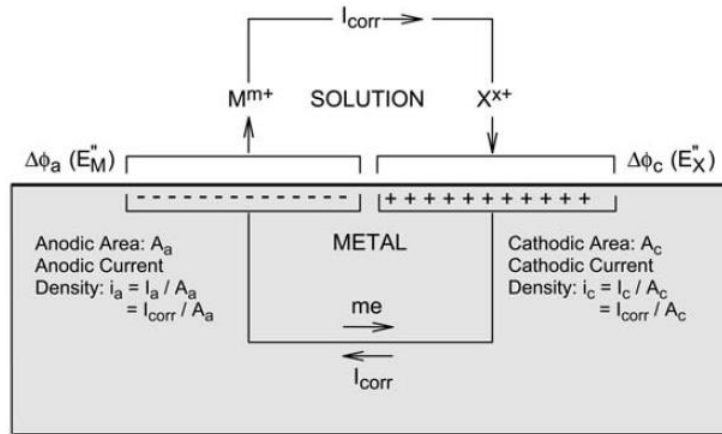
Figure 4.1 – Aqueous corrosion of metal (adapted from [223]).

The electron transfer gives origin to differences in electrical potential between the metal and the solution, $\Delta\phi_a$ and $\Delta\phi_c$, at the anodic and cathodic site, respectively:

$$\Delta\phi_a = \phi_{M,a} - \phi_{S,a} \qquad \text{(Eq. 4.1)}$$

$$\Delta\phi_c = \phi_{M,c} - \phi_{S,c} \qquad \text{(Eq. 4.2)}$$

Where $\phi_{M,a}$ and $\phi_{M,c}$ are the metal potential at the anodic and cathodic sites, respectively, and $\phi_{S,a}$ and $\phi_{S,c}$ are their counterparts on the solution side. The current flows in solution from anodic to the cathodic site, because $\phi_{S,a} > \phi_{S,c}$, which means that the potential driving the current in solution, $\Delta\phi_S$, is

$$\Delta\phi_S = \phi_{S,a} - \phi_{S,c} = \left(\phi_{M,a} - \Delta\phi_a\right) - \left(\phi_{M,c} - \Delta\phi_c\right) \qquad \text{(Eq. 4.3)}$$

Since the metal is a good conductor, it can be considered that potential differences in the metal are negligible and

$$\Delta\phi_S = \Delta\phi_c - \Delta\phi_a \qquad \text{(Eq. 4.4)}$$

Following Ohm's law, the corrosion current, I$_{corr}$, is then

$$I_{corr} = \frac{\Delta\phi_c - \Delta\phi_a}{(R_S + R_M)} \qquad \text{(Eq. 4.5)}$$

These electric potential differences at the anodic and cathodic sites are merely representative of an equilibrium condition for which no net current flows, the so called equilibrium half-cell potentials. Under current flowing conditions, the areas of the anodic and cathodic regions are important, and the half-cell potentials are shifted by a value η, the overpotential, which increases in magnitude with higher current densities, and the real corrosion current becomes:

$$I_{corr} = \frac{[\Delta\phi_c + \eta_c(I_{corr}/A_c)] - [\Delta\phi_a + \eta_a(I_{corr}/A_a)]}{(R_S + R_M)} \qquad \text{(Eq. 4.6)}$$

To become anodic, i.e. undergo corrosion, the half-cell potential of a metal must be inferior to the half-cell of a corresponding cathodic reaction. Although this is important, the physicochemical condition of an exposed metal surface is also determinant for it to corrode. Hence imperfections like dislocations, scratches and grain boundaries or even other factors such as the crystal orientation and alloying elements and phases, are very important on determining if a given metal will become anodic, which type of corrosion will occur and at what rate [223].

For a metal, M, the most elementary corrosion reactions are:

$$M + mH^+ \rightarrow M^{m+} + \frac{m}{2}H_2 \qquad \text{for pH<7} \qquad \text{(Eq. 4.7)}$$

$$M + mH_2O \rightarrow M^{m+} + mOH^- + \frac{m}{2}H_2 \qquad \text{for pH≥7} \qquad \text{(Eq. 4.8)}$$
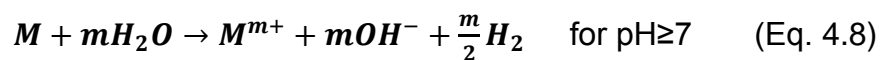
This means that the metal M will be released in solution in its ionic form, with valence m, by the action of hydrogen ions. As the pH increases, water molecules increasingly contribute for metal oxidation. Hence, electrons are transferred from anodic to cathodic sites on the metal, M, corresponding to a change in charge from M to M^{m+} and from mH^+ to $^m/_2$ H_2. Given the electron mobility allowed in the metal, these reactions can occur in distinct places which can be restrained to atomic distances or occur in huge macroscopic areas of several square meters. If the anodic and cathodic sites are nearly undistinguishable and undergo changes and reversal with time, uniform corrosion is said to occur. If it is possible to resolve these areas and they do not change with time, then the corrosion is said to be localized and its observation is almost exclusive in anodic areas [223].

But corrosion does not depend on pH alone. Other variables like the concentration of dissolved gases like O_2 or CO_2, the presence of complexing agents or the presence of species that precipitate the metal ions released in solution, can combine to define the localization and rate of corrosion reactions. As an example, the presence of dissolved oxygen in solution will result in the occurrence of the following reactions:

$$M + \frac{m}{4}O_2 + mH^+ \rightarrow M^{m+} + \frac{m}{2}H_2O \qquad \text{for pH<7} \qquad \text{(Eq. 4.9)}$$

$$M + \frac{m}{4}O_2 + \frac{m}{2}H_2O \rightarrow M^{m+} + mOH^- \qquad \text{for pH≥7} \qquad \text{(Eq. 4.10)}$$
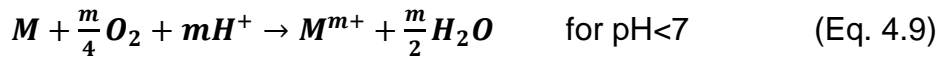
In practice, this means that corrosion is accelerated because there is an additional reaction consuming electrons. However, the formation of corrosion products (take the example of Fe_2O_3 or $FeO(OH)$ on the surface of iron) and their change with time will also influence the corrosion rate. Depending on the adhesion and porosity of the formed precipitates, they might constitute barriers through which ionic species and O_2 will have to diffuse to sustain corrosion. Conversely, if the precipitates are non-adherent and have very low solubility, the corrosion rate can accelerate due to the continuous extraction of metal ions. For metals that form well adhering protective films, corrosion is strongly attenuated and its rate drops several orders of magnitude [223].

4.2. Scanning probe techniques for the study of corrosion

4.2.1. The scanning vibrating electrode technique

The SVET (Scanning Vibrating Electrode Technique) is an electrochemical technique suited for the study of ionic fluxes, having been first applied to corrosion by the effort of Isaacs [224]. This technique can measure local currents at the surface of metals immersed in electrolyte solutions. These currents derive from ionic fluxes with origin in electrochemical reactions on the metal surface [225]. The oxidation and reduction reactions occurring in anodic and cathodic sites cause variations in the concentration and distribution of ionic species, which in turn create electric fields, as shown in Figure 4.2. By using a vibrating microelectrode to scan the surface of interest the potential difference between points can be determined versus a reference electrode. The recorded signal is transformed to an AC signal with the same frequency as the vibration of the microelectrode. A current map of the whole surface can easily be obtained by setting a grid of points to measure, and using Ohm's law to calculate the current intensity from the potential difference recorded between points [225]. An alternative to SVET is SRET (Scanning Reference Electrode Technique) in which the probe is used in a static configuration as current is measured instead of potential.

The technique has been used for research on pit formation, electrochemically active pin-hole defects in coatings, corrosion inhibitor performance, galvanic corrosion, etc.
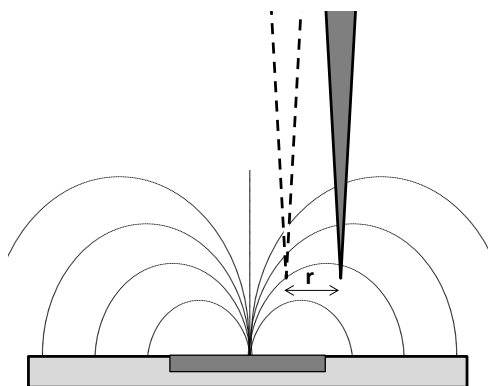
Figure 4.2 – SVET measurement scheme showing a microelectrode vibrating with an amplitude *r,* which along with the frequency of vibration will be used to determine the value of the ionic current (adapted from [225]).

4.2.2. Scanning Kelvin probe

The Scanning Kelvin Probe (SKP) technique is used for the measurement of micro-galvanic activity near an electrochemically active surface in the presence of a thin electrolyte layer or drop, or even in humid air and it allows the determination of the work function of conducting and semiconducting materials [226].

The Kelvin Probe tip and the surface of the sample form a capacitor. The distance between the tip and the surface varies by vibrating the probe and an AC current then flows through an external circuit, with an intensity that is consequence of the potential variation between the tip and the surface. This potential difference can be compensated by adjusting the external voltage. The probe is usually made of a material with constant surface potential. (e.g. a Ni/Cr wire tip), which implies that the locally measured potential arises only from the surface potential of the sample (Figure 4.3) [26].

A reference electrode is used to calibrate the Kelvin probe by touching the surface of the sample. Simultaneous measures with the two probes yield the potential which differs from the corrosion potential by a constant value, related to the experimental setup (eq. 4.11) [226].

$$E_{corr} = constant + \left(\frac{\phi_1 - \phi_2}{e}\right) \qquad \text{(Eq. 4.11)}$$

Where ϕ_1-ϕ_2 is the difference in work function between the Kelvin probe and the sample and e is the electron charge. The technique allows the investigation of coating degradation, performance of corrosion inhibitors, etc.
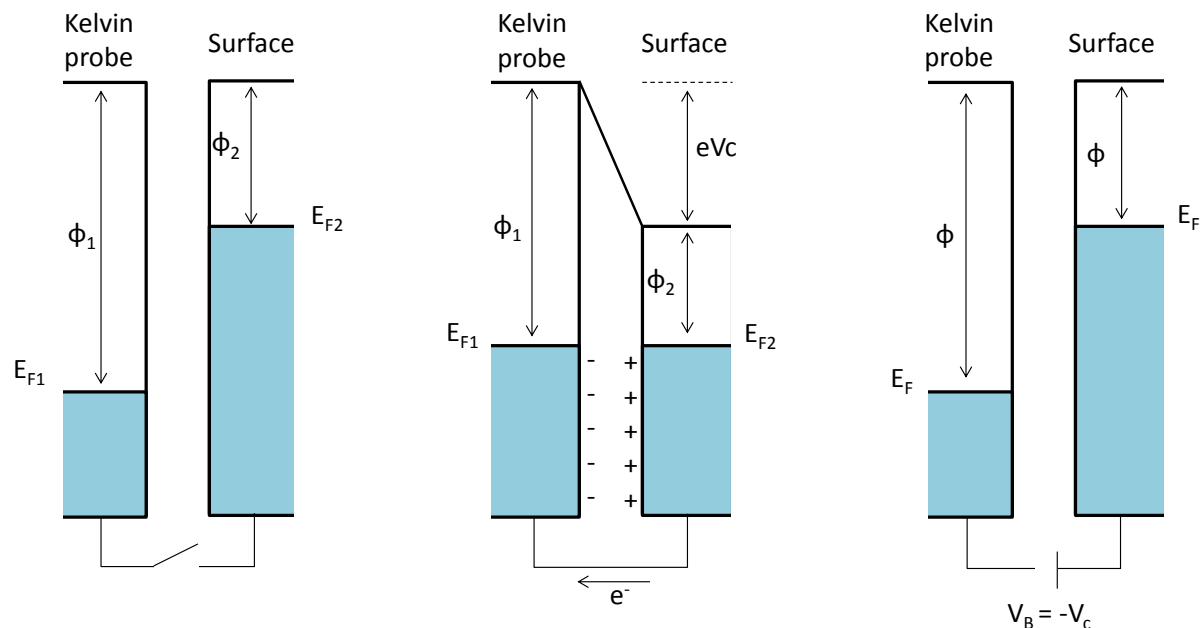
Figure 4.3 – Energy level variations as basis for Scanning Kelvin Probe measurements (adapted from [226]).

4.2.3. Local electrochemical impedance spectroscopy

Electrochemical Impedance Spectroscopy is a widely used technique for the study of corrosion rates. It measures the polarization resistance, R_p, of a metal, which is proportional to the rate of corrosion occurring at the monitored interface [227].

$$R_p = \frac{B}{i_{corr}}$$ (Eq. 4.12)

$$B = \frac{b_a b_c}{2.3(b_a + b_c)}$$ (Eq. 4.13)

Where b_a and b_c are anodic and cathodic Tafel slopes, respectively.

By this technique the properties of an electrode/electrolyte system are evaluated as a function of the frequency of an applied ac signal of small amplitude, at a fixed working point. Impedance spectra is collected over a frequency range that can go up to 10

orders of magnitude [228]. Data evaluation is done with the aid of Bode plots, which display the complex impedance spectra as function of the frequency *f* of the applied AC signal. An equivalent circuit is needed for fitting the experimental data and information about system properties and their changes with varying experimental conditions can be extracted [228].

Local impedance electrochemical spectroscopy (LEIS) consists on the application of a sinusoidal voltage perturbation between the sample and reference electrode. The current density over a sample is then probed by a double-electrode as a function of applied frequency. The probe is fixed in a stationary point and the sample below is dislocated with X/Y stages. For any frequency, the current density of the solution is extracted from Ohm's law and the potential difference between the probe electrodes:

$$i(\omega)_{local} = \frac{\Delta V(\omega)_{probe}\kappa}{l} \qquad \text{(Eq. 4.14)}$$

Where $\Delta V(\omega)_{probe}$ is the AC voltage difference between the probe electrodes, κ is the conductivity of the electrolyte solution and *l* is the distance between the probe electrodes. The local impedance can then be determined using the following relationship:

$$|Z(\omega)|_{local} = \frac{V(\omega)_{applied}}{i(\omega)} \qquad \text{(Eq. 4.15)}$$

Where $V(\omega)_{applied}$ is the AC perturbation potential applied between the reference electrode and the surface. This technique has been applied to corrosion studies such as pitting corrosion and the examination of defective coatings, among others [228].

4.2.4. Scanning electrochemical microscopy

Scanning Electrochemical Microscopy (SECM) uses a microelectrode as scanning probe for measuring faradaic currents, originating from a diffusion controlled redox reaction of a mediator species at the SECM tip. This current is affected by the nature of the sample below the tip and the distance between both. The electric state of the tip and

the substrate can be controlled separately which allows this technique to operate under a variety of modes [229]. For corrosion investigation three of them have proved to be more useful: the feedback mode, the generation/collection mode and the redox competition mode.

In the feedback mode, both electrically insulating and conducting substrates can be imaged by SECM, employing a redox mediator species. The SECM tip is made to scan the X–Y plane of the surface of the sample. The measured faradaic current is limited by the diffusion of the mediator, and is associated to the separation between the tip and the sample bellow, i.e., a topographic image can be obtained (Figure 4.4). The resolution of the image is obviously limited by the radius of the SECM tip [20].

However, the redox mediators used in SECM can interfere in the investigation of corrosion processes. The generation/collection mode allows electrode processes and coupled homogeneous reactions to be studied. Both substrate generator-tip collector and tip generator-substrate collector variants can be used. The former is useful to determine concentration profiles of electroactive species originating from the substrate. This is adequate for detecting species resulting from anodic oxidation of metals if the adequate potential is selected [230].

The tip generator-substrate collector mode is suited for the study of homogeneous reactions occurring in the gap between the tip and the substrate. However, some relevant limitations are inherent to this mode. One of them is the loss of sensitivity with increasing substrate areas because the background current increases. A limit in resolution is also imposed, since the smaller the SECM tip, the more the current signal will be indistinguishable from the background [231]. Hence, in cases such as imaging of catalytic activity, this mode has proved to be inadequate. A possible solution is to use the redox competition mode. With this operating variant, both the tip and the substrate compete for the electroactive species, which in some cases like the study of catalytic materials for the oxygen reduction reaction, has been proved successful [231].

Recently other SECM variants have been used. Perhaps the most successful is AC-SECM in which an oscillating potential perturbation is applied to the tip and an AC current is then measured for different perturbation frequencies. The greatest advantage is possibly working without the need of redox mediators [232].

The use of SECM for corrosion research has been demonstrated in cases of pitting corrosion [233], galvanic corrosion [234], inhibitor performance [235], evaluation of organic coatings [236], among others.
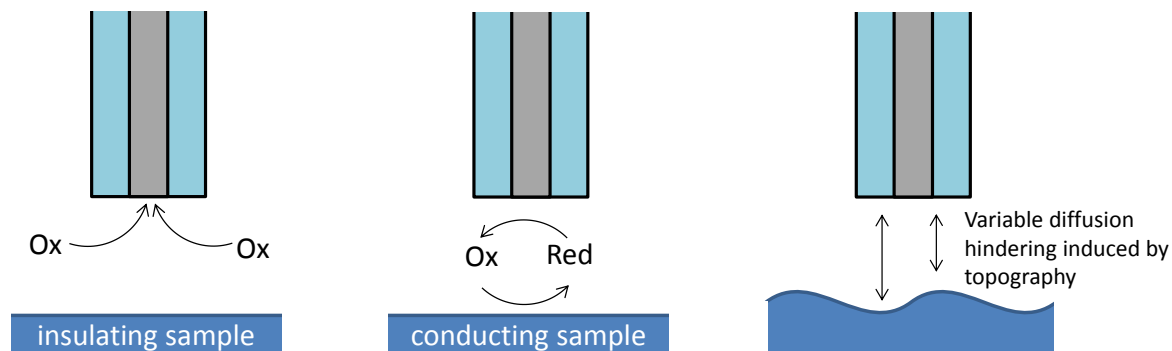
Figure 4.4 – SECM operation dependence with the electrical nature of the sample and surface topography.

The sections 4.3 to 4.5 below correspond to three scientific articles focusing on the application of diamond microelectrodes for localized amperometric (4.3 and 4.4) and potentiometric (4.5) measurements, using the instrumentation of a SVET system. On section 4.3, as-grown diamond microelectrodes are used for Zn(II) and molecular oxygen measurements. Section 4.4 regards the use of BDD MEs with CF_4 plasma surface modification, as a route to enhance the sensitivity and response time for dissolved oxygen measurements. Finally, on section 4.5, BDD MEs with surface modification by oxygen plasma are demonstrated as being pH sensitive and constituting a possible solution for mapping the pH variation in corrosion systems.

4.3.   Boron doped nanocrystalline diamond microelectrodes for the detection of Zn^{2+} and dissolved O_2

E. L. Silva, A. C. Bastos, M. A. Neto, R. F. Silva, M. L. Zheludkevich, M.G.S. Ferreira, F. J. Oliveira

CICECO - Dept. of Ceramics & Glass Engineering

University of Aveiro, Campus Universitário de Santiago, 3810-193 Aveiro, Portugal

elsilva@ua.pt

Abstract

Boron-doped nanocrystalline diamond (B-NCD) films were grown by the hot filament chemical vapour deposition (HFCVD) technique on top of sharp electropolished tungsten substrates, in order to create amperometric microelectrodes (MEs) for detection of Zn^{2+}(aq) and dissolved O_2. The boron source was a B_2O_3 + ethanol mixture dragged by Argon gas through a bubbler. Different B_2O_3 concentrations were used to study the doping effect on the electrochemical behaviour. The B-NCD MEs exhibited a working potential window of about 3.5 V in 5 mM NaCl, with low background current and good chemical inertness. The best electrochemical kinetics was achieved for the ME with highest boron doping content. The linear relationship between zinc concentration and zinc reduction current was found in a wide concentration interval from 10^{-5} M to 10^{-2} M of $ZnCl_2$ in a 5 mM NaCl background. Measurements with a Fe-Zn galvanic couple immersed in 5 mM NaCl demonstrate potential applicability of the B-NCD ME for use in localized corrosion studies.

Keywords: B-NCD, microelectrodes, zinc, corrosion, amperometric

4.3.1. Introduction

Apart from its outstanding mechanical and thermal properties [237], CVD diamond has been object of intense study for the last two decades due to its promising electrical properties, when doped by other elements, particularly boron [98,206,238]. Therefore diamond was studied for electrochemical purposes [83] taking into account its superior chemical stability. Boron-doped CVD diamond was reported to exhibit a potential window of water stability wider than any other solid electrode material. A very low background current and extreme chemical inertness and resistance to fouling due to the non-polar H terminated surface can also be counted as important advantages [70,128,192]. The promising results have encouraged high interest on diamond to be applied for microelectrodes as well [118]. As a result of electrode miniaturization to a critical dimension of <25 μm [8], which enables working with enhanced mass transport and steady state currents, as well as measurements in high resistivity media, CVD diamond microelectrodes (MEs) became an increasing matter of research, mainly in the biological field.

A variety of microstructures ranging from microcrystalline to nanocrystalline diamond can be obtained by synthesis in metastable conditions, which is the case of CVD methods such as the hot filament assisted CVD (HFCVD). Nanocrystalline diamond is the most interesting for MEs because of its grain size allowing maximum miniaturization of the electrode [139]. Although there are many bio-related publications with diamond electrodes [119,120,191,239–241] and some works concerning the detection of trace metals and use of B-doped diamond electrodes in SECM [131,242,243], to our knowledge there are no published works applying B-doped diamond MEs to the corrosion field, where they can also play an important role.

Our main interest in this work was focused on optimization of the electrochemical properties of boron-doped nanocrystalline diamond (B-NCD) films to be used in amperometric MEs for corrosion studies. An example of such measurement is the distribution mapping of electrochemically active species generated or consumed in confined areas on corroding metal surface. Such experiments are of prime importance for understanding mechanisms and kinetics of corrosion and self-healing processes in the local defects of active coatings [234,244]. Particular interest is in the case of metal

cations that are reduced at potential range where the reduction of water and dissolved oxygen can mask their amperometric detection. This is a limiting condition for most electrode materials currently in use but it may be an opportunity for B-NCD based MEs. One of the most corrosion relevant cases is determination of local concentration of zinc cations in the electrolytes near corroding surface of galvanized steel. Zinc has widespread applications of great importance such as galvanic coatings on steel, as anodes for common batteries or in brass metallurgy. It is also relevant in the metabolism of plants, animals and microorganisms [245–247].

The quantification of zinc is therefore a significant matter for many different areas, but the means available are limited mostly to spectroscopic and electrochemical stripping techniques [248–250]. Recently, Strasunske et al. [251] obtained good results by using silver amalgam electrodes (3 mm in diameter) to analyze river water by differential pulse anodic stripping voltammetry. Tada et al. have reported the voltammetric detection of Zn^{2+} by using a small zinc disk electrode to probe the corrosion of Zn/steel couple, but within a narrow concentration range and with millimetric, not micrometric, resolution [252]. Attempts also have been made for localised potentiometric detection of Zn^{2+} with ion-selective microelectrodes but the electrodes still present low sensitivity, low selectivity, short lifetime and complex fabrication [253,254]. In terms of the use of B-NCD electrodes, the group of G.M. Swain has reported satisfactory results using B-NCD electrodes for the detection of Zn^{2+} and other heavy metals by anodic stripping voltammetry, although large metal deposits and electrode fouling were a problem [255,256]. However, the size of the electrode again does not allow the spatial mapping in the micrometric range.

In the present work, we report the fabrication of B-NCD microelectrodes and their use as probes for Zn^{2+} and oxygen detection by performing cyclic voltammetry (CV) and microamperometry measurements at fixed potential in zinc chloride solutions and in a model Zn-Fe galvanic corrosion system.

4.3.2. Experimental

4.3.2.1. Microelectrode fabrication

Substrate preparation

Electrosharpened tungsten wires (99.9%+, Ø125 μm, Goodfellow, England) were used as a body of electrode. The sharpening of the wires was performed via electropolishing in a custom-made dynamic flow system, using a 3 M NaOH solution. Each filament was connected as a working electrode (anode) in the electropolishing system and was sharpened by applying a potential difference of 10 V between the working and the counter electrode during 50 s while keeping the solution flowing. The tips were sharpened down to radii of <100 nm and ultrasonically cleaned with distilled water. Afterwards they were ultrasonically seeded during 10 minutes in a suspension of nanodiamond powder (~6 nm, 98+ %, ABCR, Germany) in distilled water and ultrasonically cleaned during 15 minutes in ethanol to remove the rest of powder.

Diamond film growth

The diamond films were grown by HFCVD with four tungsten filaments at a temperature of 2300 ºC that worked as gas activators and substrate heating sources. The sharpened tungsten tips were positioned horizontally on a substrate holder below the filaments at a distance of 7 mm. B-NCD films were grown during 30 minutes. The substrate temperature and the total gas pressure were kept constant at 770 ºC and 180 mbar, respectively. The gas phase was composed by hydrogen and methane with a 0.07 CH_4/H_2 ratio with addition of the boron doping mixture. The boron source for doping the films was a solution of boron oxide (B_2O_3, 99.6%, ABCR) dissolved in ethanol inside a gas washing bottle. This boron-containing solution was dragged by argon gas into the CVD reaction chamber, with a constant $(Ar+B)/H_2$ ratio of 0.03. Solutions with three different B_2O_3 concentrations of $2x10^{-4}$, $1x10^{-3}$ and $2x10^{-3}$ M were tested for the S1, S2 and S3 microelectrodes, respectively. The microstructure of the grown films was evaluated by scanning electron microscopy (Hitachi SU-4100). UV μ-Raman spectroscopy (HORIBA JOBIN YVON HR800UV), using the line 325 nm from a He-Cd

laser (KIMMON IK series) for surface excitation, allowed the identification of the different carbon sp^2/sp^3 phases incorporated in the coatings and the presence of residual stresses.

Electroactive area delimitation

The B-NCD covered tungsten wires were partially insulated with acid resistant varnish (Lacomit, AGAR) with the aid of a micrometric manipulator under a microscope in order to limit the electroactive area just at the apex.

4.3.2.2. Electrochemical measurements

Electrode characterization

The electrochemical response of the B-NCD MEs was tested by cyclic voltammetry with a AUTOLAB PGSTAT302N potentiostat/galvanostat (Eco Chemie, The Netherlands). The electrochemical cell was kept inside a Faraday cage, open to air, and consisted on the B-NCD ME as working electrode, a platinum counter-electrode and a saturated calomel electrode (SCE) as reference. All potentials in this paper are referred to SCE except for the line and 2D-map scans in corrosion testing, where a Ag|AgCl electrode was used as reference. The electron transfer kinetics was evaluated in 10 mM $Fe(CN)_6^{3-/4-}$ in 5 mM NaCl (all reagents were *pro analysis* grade from Riedel-deHäen). The B-NCD MEs were compared with platinum and gold microelectrodes (10 μm discs embedded in cylindrical glass with a conical tip of 200 μm in diameter) for the detection of Zn^{2+} in $ZnCl_2$ solutions ranging from 10^{-6} M to 10^{-2} M in 5 mM NaCl (pH=2). All potentiodynamic measurements were performed with a scan rate of 100 mV s^{-1}.

Application to corrosion testing

A model system consisting of a Fe-Zn galvanic couple immersed in 5 mM NaCl solution was used in order to evaluate applicability of the B-NCD MEs for mapping the distribution of Zn^{2+} and O_2 near active corroding metallic surfaces. Microamperometry measurements were performed with an IPA2 amplifier (Applicable Electronics Inc., USA) in the voltammetric/amperometric mode, using a 2 electrode arrangement, with a

Ag|AgCl electrode as counter and reference electrode. Linear or 2D scans were done using B-NCD ME at a distance of 100 µm from the surface. Lines and maps were recorded at a potential of -0.9 V (vs. Ag|AgCl) for detection of dissolved O_2 and -1.6 or -1.3 V (vs. Ag|AgCl) for detection of Zn^{2+}.

4.3.3. Results and discussion

4.3.3.1. Electrode characterization

The microscopic observations of the coated W-microelectrodes demonstrate presence of a dense intact diamond layer on the metal surface, which was confirmed by Raman spectroscopy. Each of the Raman spectra in Figure 4.5 shows the following features: i) at 1140 and 1470 cm^{-1}, commonly assigned to transpolyacetylene (TPA) in the grain boundaries; ii) at 1333 cm^{-1}, indicating the presence of diamond crystals; iii) at 1340 cm^{-1} and 1540 cm^{-1}, assigned to the D and G bands of graphite, respectively [203].
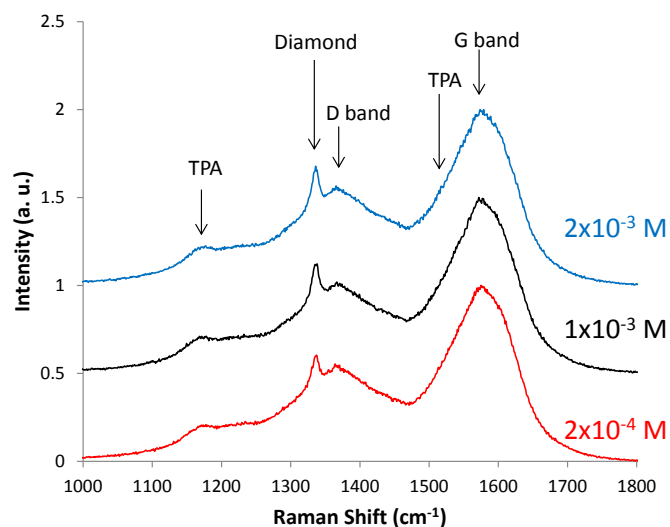
Figure 4.5 - Raman spectra (325 nm wavelength) of the B-NCD films grown with different B_2O_3 concentrations of $2x10^{-4}$, $1x10^{-3}$ and $2x10^{-3}$ M. There are five main features: at 1140 and 1470 cm^{-1}, assigned to transpolyacetylene (TPA) in the grain boundaries; at 1333 cm^{-1}, indicating the presence of diamond crystals; at 1340 cm^{-1} and 1540 cm^{-1}, assigned to the D and G bands of graphite, respectively.

No voids are observed at the B-NCD films, meaning that the tungsten tip is well insulated from the analyte by the B-NCD coating (Figure 4.6a). Good coverage and intactness of the diamond film is crucial in order to avoid the penetration of electrolyte to the metal surface and the consequent electrochemical response o tungsten during the measurements. The tungsten tips with B-NCD films were coated with a polymer layer in order to provide an electrical insulation leaving only an apex as exposed zone of the probe. The exposed are was about ~30 μm^2 with a tip radius of ~0.5 μm (Figure 4.6b).
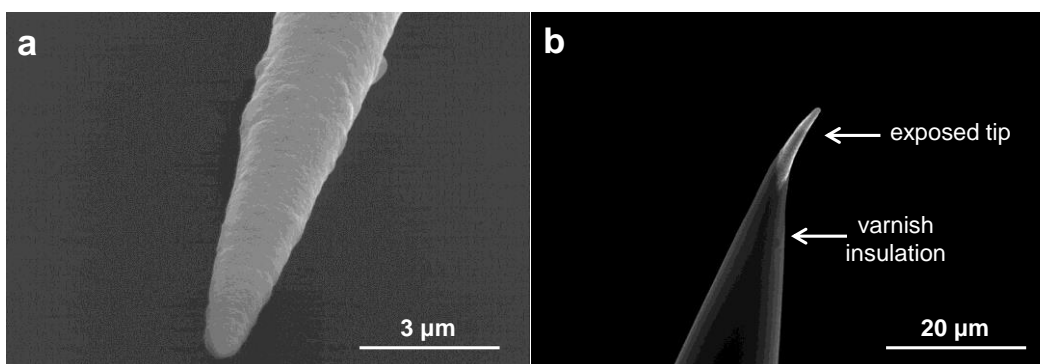
Figure 4.6 - SEM micrographs of a) B-NCD film grown on top of sharp tungsten wire, b) B-NCD probe insulated with varnish, showing a typical exposed area.

The CV measurements were performed on a bare tungsten microelectrode in the potential range from -1.5 to 1 V in 5 mM NaCl in order to exclude the situation of W-substrate contribution for the electrochemical measurements, (Figure 4.7a). Besides water reduction, three oxidation peaks are observed that can be related to the formation of W_2O_5, WO_2 and WO_3 at the tungsten surface, since these are known to be the most stable oxide products [257].

None of these peaks was observed in the current-potential curve of the B-NCD microelectrode as shown in Figure 4.7a (inset) in the same solution within the referred potential range, confirming the absence of response from the W substrate. Instead, only water oxidation (starting at ~1 V) and a small response from water reduction were observed. The kinetics for the latter process is extremely slow at the B-NCD surface as can be seen in Figure 4.7b for the S1 ME, which shows a very high overpotential for hydrogen evolution. This behavior corresponds to a ~3.5 V usable window, which is larger than the 2.5-3.0 V window reported in various works for B-NCD [50,123,211].
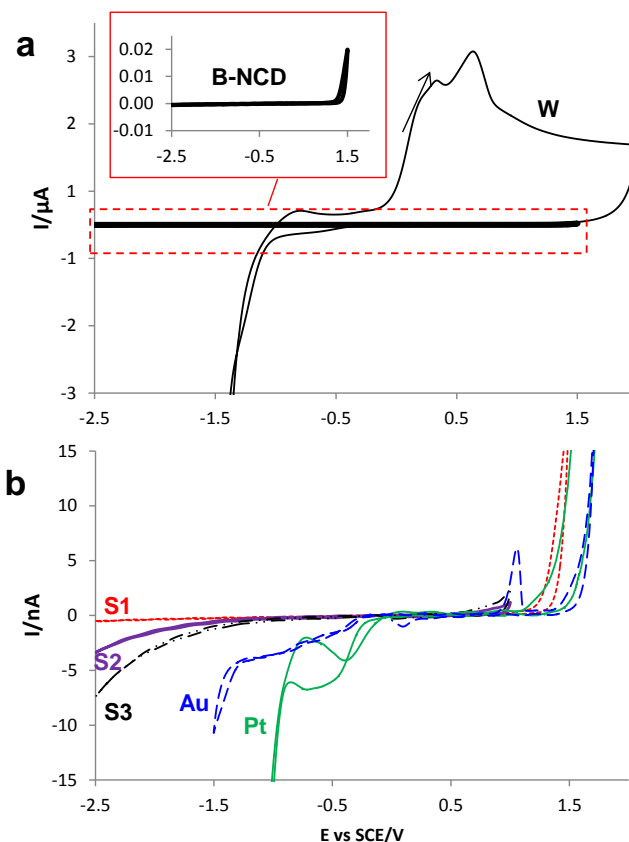
Figure 4.7 - Voltammograms of a) a bare tungsten microelectrode and a B-NCD (S1) probe in 5 mM NaCl, b) Pt, Au and S1, S2 and S3 B-NCD microelectrodes in 5 mM NaCl.

The response of the B-NCD MEs was also compared with platinum and gold MEs in the same solution. It can be observed that the reduction of dissolved oxygen and water are easier on both platinum and gold, with overpotentials lower than the exhibited by the B-NCD MEs, although they do present a higher overpotential for water oxidation.

The unfavorable kinetics for water and oxygen reduction at the B-NCD surface, however, could be also an indication of slow kinetics for other processes. For obvious reasons, there is no point in producing MEs with extensive potential windows if the electron transfer kinetic is not adequate within the working window. Attending to the electrochemical properties of CVD diamond and, in particular, to the microstructure of NCD, the slow kinetics of this material is likely to be associated with low conductivity

originated by ineffective boron doping. NCD presents a huge number of grain boundaries due to the size of its crystallites. These regions can contain a high amount of different non-diamond carbon species such as graphitic phases and trans-polyacetylene which are sp^2 bonded when NCD is grown by HFCVD [203]. The grain boundaries can be a problem for the overall electrical conductivity of doped NCD films in several ways. First, although the non-diamond carbon phases in the boundaries can provide electrical conductivity to undoped NCD, they are not a reliable form of charge transport because of the implicit instability of these carbon forms, which can easily be etched or oxidized, either electrochemically or thermally [63]. Conversely, by promoting the substitutional incorporation of boron atoms into carbon lattice positions, electric conduction by electronic holes is enabled in a consistent manner, ensuring the reliability of the material's electrical conductivity and chemical stability. The second way is also related to sp^2 carbon π bonds and their unsaturated nature, which increase the reactivity of the B-NCD film and also ease the poisoning of the surface [100]. A third mechanism how grain boundaries affect the conductivity of the NCD films is by acting as "sinks" for the boron atoms, thereby reducing the doping degree. According to Goss et al., grain boundaries and near grain edge sites require lower energy for boron integration than intra-grain positions. However boron only contributes to the overall conductivity of the film by occupying substitutional positions in the diamond lattice [96]. Even though grain boundaries are a problem, reducing their number would contribute to a coarsening of the surface microstructure of the ME and could compromise the electrode miniaturization level. The solution relied on improving the conductivity of the MEs by increasing the boron content through higher B_2O_3 concentrations in the doping solutions. Figure 4.7b shows that raising the boron concentration in the solution from 10^{-4} M for the S1 ME to 10^{-3} M for S2 and 2×10^{-3} for the S3 ME resulted in a slight narrowing of the working potential window but also contributed to an improvement in the electrode transfer kinetics, as is shown in the CV curves on Figure 4.8 for the $Fe(CN)_6^{3-}/^{4-}$ redox system. The peak separation, ΔE_p, decreased from 302 mV in S1 to 101 mV in S3, along with the increase of the current peak values (Table 4.1). Although the ΔE_p for reversible 1 electron reactions is expected to be around 59 mV [258], the ΔE_p variation from S1 to S3 indicates a more reversible behavior at the surface of the S3 ME.

An alternative to changing the amount of boron doping is varying the Ar+B flow, but this would also change the amount of available carbon in the active gas phase leading to the deposition of high amounts of sp^2 bonded non-diamond material in the B-NCD films. Thus a good compromise between fast kinetics and acceptable working potential window was obtained in the case of S3 ME particularly for negative potentials which is the region of interest for the detection of Zn^{2+}.
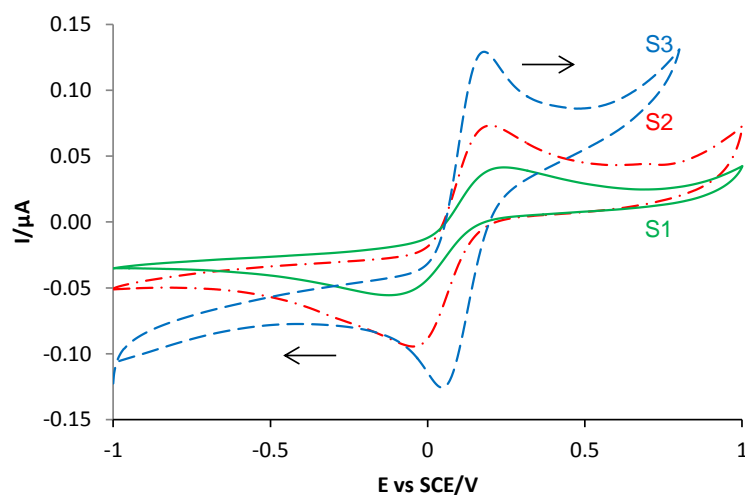
Figure 4.8 - Voltammograms using S1, S2 and S3 B-NCD microelectrodes in 10mM $Fe(CN)_6^{3-/4-}$ + 5 mM NaCl.

Table 4.1 - Electrochemical kinetic parameters for three B-NCD MEs grown with different $[B_2O_3]$ (peak potential separation, ΔE_p, oxidation peak current, i_{ox}, ratio of oxidation and reduction peak currents, I_p^{ox}, I_p^{red}, respectively).

Film	ΔE_p/mV	I_p^{ox}/µA	I_p^{ox}/I_p^{red}
S1	302	0.048	0.92
S2	222	0.105	1.17
S3	101	0.162	1.32

4.3.3.2. Zn^{2+} detection

Several MEs with the S3 composition were studied for the detection of Zn^{2+} and dissolved oxygen. The first step was to compare B-NCD MEs with common inert electrode materials such as platinum and gold. The detection of zinc was performed in acidified ZnCl$_2$ solutions (pH 2) since at this pH Zn^{2+} is clearly dominant over other soluble species such as ZnCl$^+$ and ZnOH$^+$. The formation of carbonated zinc species is also not favorable in acidic conditions [136, 248]. Cyclic voltammetry was also performed on Pt and Au MEs in ZnCl$_2$ solutions with Zn^{2+} concentrations of 10^{-5}, 10^{-4} and 10^{-3} M in a 5 mM NaCl background. The results are presented in Figure 4.9a-c, where the inability of these materials to accurately reduce Zn^{2+} to its metallic form becomes clear. Both the Pt and Au MEs present variations in the current-potential curves denoted by higher currents for increasing Zn^{2+} concentration but not proportionally to the magnitude change in the Zn2+ concentration, Figure 4.9b and c. In Figure 4.9d the current values selected at the potential of -1.6 V for B-NCD and Au and -1.4 V for Pt, are plotted as a function of the Zn^{2+} concentration evidencing the higher sensitivity of the B-NCD ME in this concentration range.
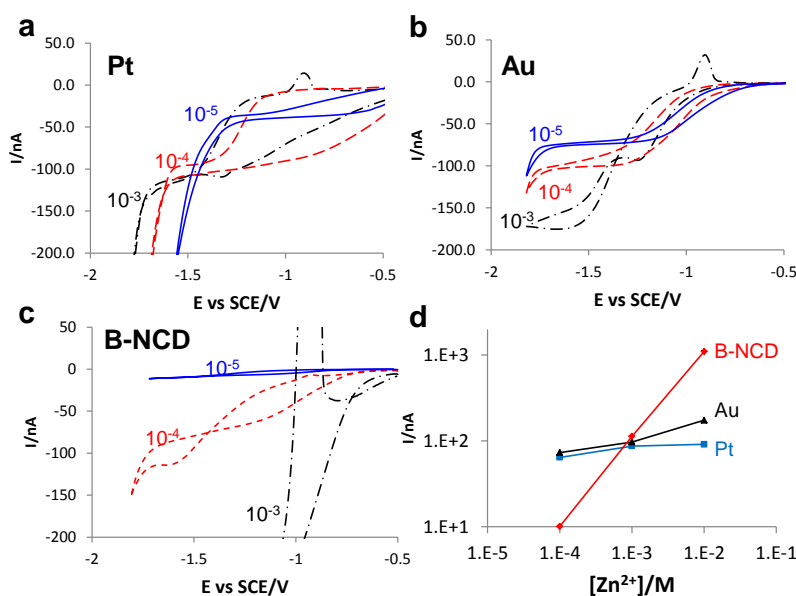
Figure 4.9 - Voltammograms using a) Pt, b) Au and c) B-NCD microelectrodes in ZnCl$_2$ solutions of 10^{-5}, 10^{-4} and 10^{-3} M in 5 mM NaCl, revealing the good performance of B-NCD for the reduction of Zn^{2+} in comparison with the poor behaviour exhibited by Pt and Au. d) Current-concentration curves for B-NCD, Pt and Au microelectrodes in the range 10^{-5}-10^{-3} M Zn^{2+}.

A more complete study was performed by cycling the B-NCD ME from -0.5 V to -1.8 V in ZnCl$_2$ solutions with varying concentration (10^{-2}, 10^{-3}, 10^{-4}, 10^{-5} and 10^{-6} M) in a 5 mM NaCl background as shown in Figure 4.10. The main reactions expected to take place in this range of potentials are the reduction of dissolved oxygen, the reduction of water with hydrogen evolution, the reduction of Zn^{2+} to Zn(s) and the oxidation of Zn(s) back to Zn^{2+} (the waves attributed to each reaction are identified in Figure 4.10).

A two-step reaction, Zn $\rightarrow$ Zn^{+} + e^{-} and Zn^{+} $\rightarrow$ Zn^{2+} + e^{-}, has been proposed for the zinc dissolution in acidic conditions [260,261], whereas the deposition of zinc in ZnCl$_2$ solution was found to be the reverse of the same two-step reaction [262]. According to Cachet and Wiart [263], the Zn$^{+}_{ads}$ intermediate has an inhibitor effect on hydrogen evolution. In fact, the cathodic reactions on zinc near the zinc reversible potential are dominated by zinc deposition when the zinc concentration is higher than 10^{-4} M [264].

In Figure 4.10, the voltammograms for Zn^{2+} concentrations of 10^{-2} M and 10^{-3} M are different from those at lower concentrations. At 10^{-2} M, the polarization towards more negative potentials presents a well-defined plateau of diffusion controlled oxygen reduction until ~-1.25 V, followed by two rising slopes and the corresponding plateaus, one around -1.4 V and the other around -1.6 V, both considered to be related to the deposition of zinc. Excursion towards more negative potentials leads to water reduction with hydrogen evolution, starting around -1.74 V. This potential for H$_2$ evolution is the most negative of all Zn^{2+} concentrations tested, proving the inhibiting effect of higher concentration of Zn^{2+} on the evolution of this gas. On the reverse sweep, Zn^{2+} continues to deposit up to -1.1 V, then the dissolution of the deposited zinc starts and a marked oxidation peak is observed at approximately -0.9 V. The shape of the voltammogram for 10^{-3} M is similar, except for the absence of the second plateau in the cathodic sweep in the zinc deposition region and for the water reduction which starts earlier. This is probably due to the lower concentration of Zn^{2+}, which makes hydrogen evolution more favorable. No clear plateaus are detected in the cathodic sweep at 10^{-4} M, marking a transition in the behavior of the ME, which is in agreement with reference [264]. On the reverse sweep, diffusion-controlled reduction of Zn^{2+} still occurs, but the oxidation peak intensity is much lower. For 10^{-5} M the reduction of Zn^{2+} at the reverse sweep continues to be measurable but is kinetically controlled with clear dominion of water reduction.

At 10^{-6} M the reduction of Zn^{2+} is hardly detectable, as well as the dissolution peak. Conversely, the hydrogen evolution potential for the 10^{-6} M solution is the lowest of all measured concentrations, indicating that it is more favorable at lower zinc concentrations, which is again in good agreement with the previously referred works.

The average background subtracted current values of three reverse sweeps at -1.6 V were plotted against ZnCl2 concentration (Figure 4.11). The current-concentration dependence exhibits a linear behavior from 10^{-5} M to 10^{-2} M. The curve for a potential of -1.3 V is also plotted to confirm that the current-concentration linear behavior exists at potentials closer to the potential at which Zn^{2+} reduction starts. This linearity is the principal requirement for the amperometric detection of Zn^{2+}. The detection limit was determined by taking three times the standard deviation for each plot, which sets a value of 7.34×10^{-6} M for the lowest detectable concentration for MEs produced using the conditions given in the experimental section for S3 B-NCD coatings.
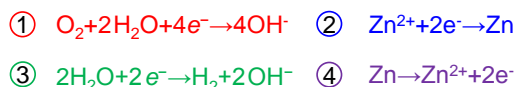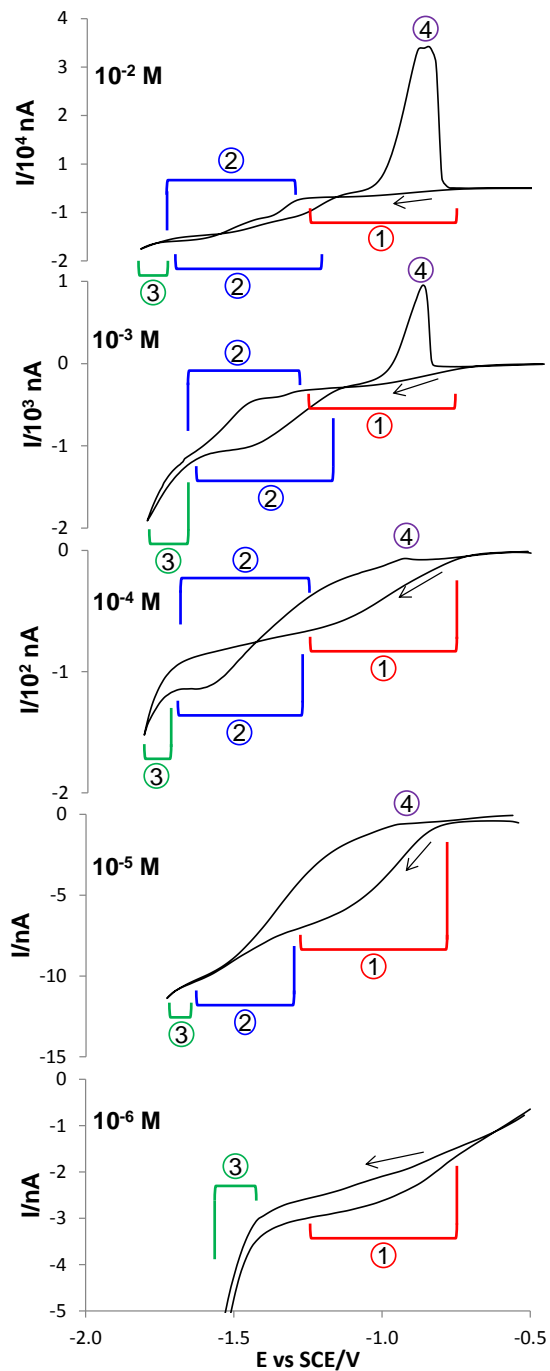
Figure 4.10 - Voltammograms of a S3 B-NCD microelectrode in $ZnCl_2$ solutions of 10^{-6}, 10^{-5}, 10^{-4}, 10^{-3} and 10^{-2} M in 5 mM NaCl, showing dissolved oxygen reduction (red line), Zn^{2+} reduction (blue line), water reduction (green line) and Zn oxidation. (Note the 10 fold change in the current scale for the different concentrations).
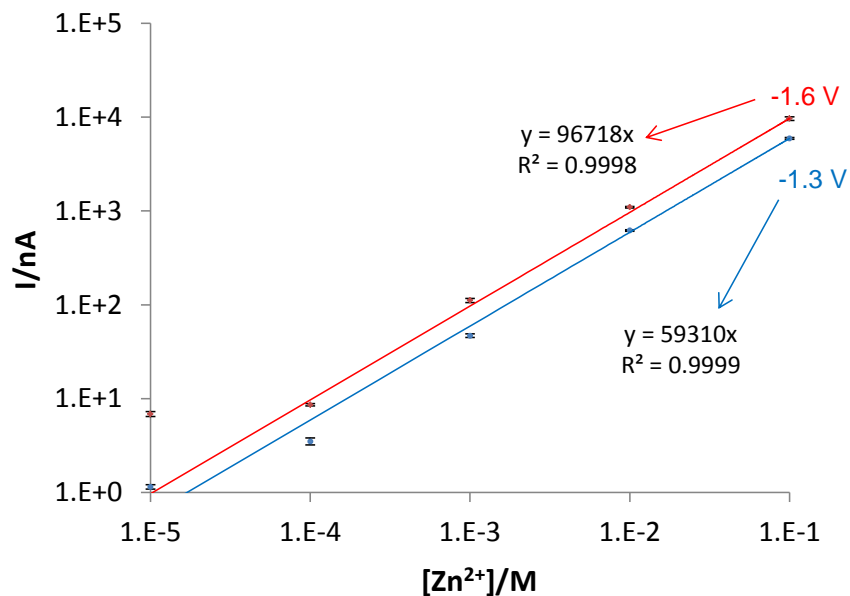
Figure 4.11 - Relationship between concentration of Zn^{2+} and the reduction current measured by the S3 B-NCD ME at -1.6 and -1.3V vs SCE from 10^{-6} to 10^{-2} M Zn^{2+}.

4.3.3.3.   Application to the corrosion of a Fe-Zn galvanic couple

In order to evaluate applicability of the B-NCD MEs in investigation of corrosion processes, measurements were performed on a model Fe-Zn galvanic couple immersed in a 5 mM NaCl solution. Figure 4.12a depicts a schematic of the cell used and Figure 4.12b a representation of the measurements performed over the couple. Figure 4.13 shows the currents related to the reduction of dissolved O_2 or reduction of Zn^{2+} to Zn at the ME, recorded in a line that passed 100 μm above the Fe and Zn electrodes. The current due to reduction of O_2 was measured with the tip polarized at -0.9 V vs Ag|AgCl and was proportional to the O_2 local concentration. The lowest values where recorded above the iron electrode which is the cathode in the galvanic couple. The oxygen consumption at the Fe surface diminishes its local amount, leaving less to react at the microelectrode tip. The oxygen reduction current also decreases above the zinc anode because, in spite of being it the couple's anode, oxygen reduction also takes place there. This happens since in parallel to the galvanic corrosion there is self-

143
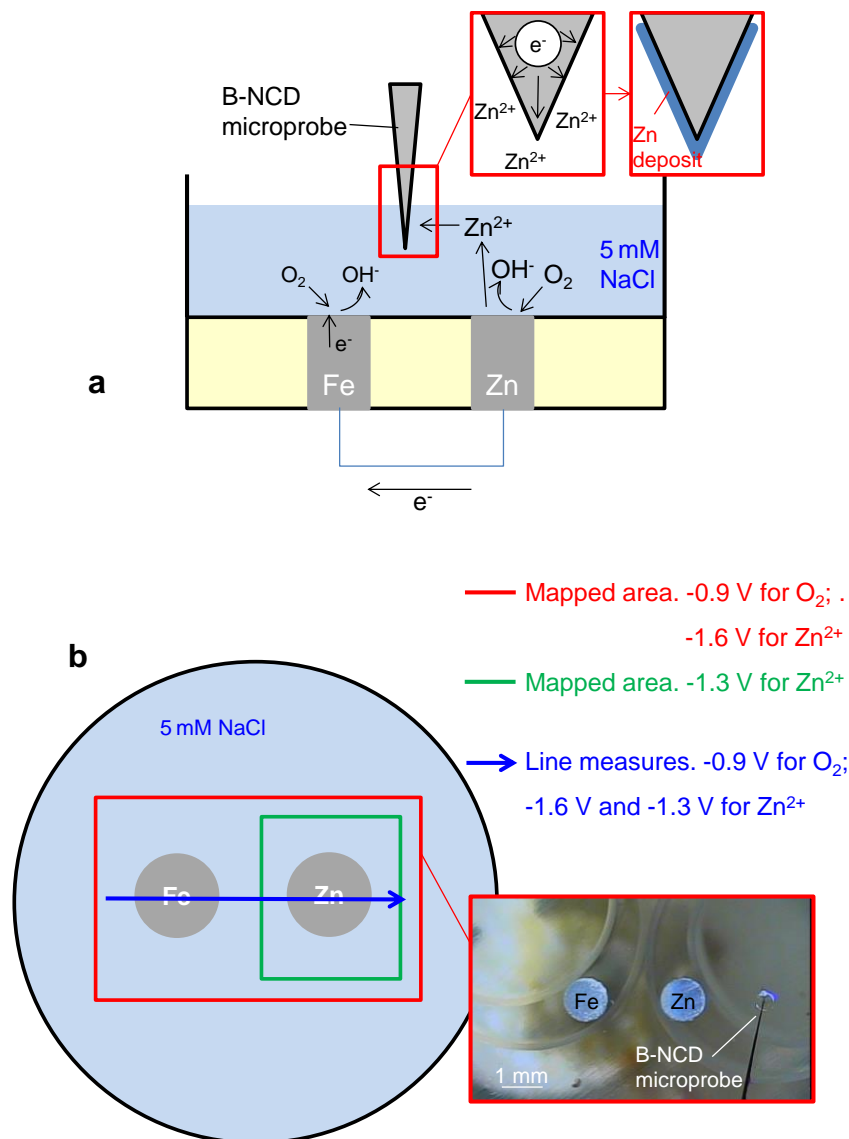
Figure 4.12 - Experimental setup for microamperometric measurements with a S3 ME. a) Fe-Zn galvanic couple immersed in 5 mM NaCl for Zn^{2+} and dissolved oxygen detection. b) Schematics of the measurements performed.

corrosion of zinc which leads to presence of local cathodic areas with oxygen reduction processes on Zn surface.

The oxidation of zinc generates Zn^{2+} ions that can be detected with the microprobe polarized at -1.6 V vs Ag|AgCl. The current raised above the zinc anode as expected but didn't return to the values found at the bulk, possibly due to accumulation of metallic zinc at the surface of the ME, with consequent increase in the electroactive area. This accumulation of Zn was found to be the main limitation of the B-NCD ME. Thereby, the

test was repeated with a lower applied potential of -1.3 V. In this case, the current increased above the zinc anode only, while a lower constant value was observed for the bulk solution.
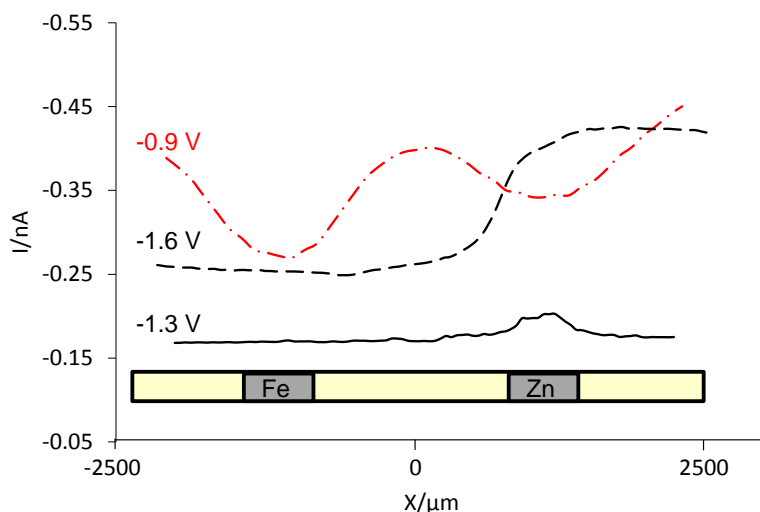
Figure 4.13 - Linear microamperometric measurements using a S3 ME for Zn^{2+} reduction at -1.6 V (dashed black line) and -1.3 V (continuous black line) and dissolved O_2 reduction at -0.9 V (red dotted line).

The increase of electroactive area by zinc accumulation is confirmed in Figure 4.14 where a sequence of cycles between -1.1 and -2.1 V presents a current rise from cycle to cycle, indicating a progressive deposition of this metal at the surface of the ME. If the upper limit of the cycles was -0.8 V instead of -1.1 V, thus including the zinc oxidation, the regeneration of the original surface would take place. Figure 4.15 shows a sequence of ten cycles from -0.8 to -1.75 V where the oxidation of the zinc just deposited renews the surface leading to similar voltammograms in every cycle. This can be a solution to overcome the unwanted increase in electrode's area.
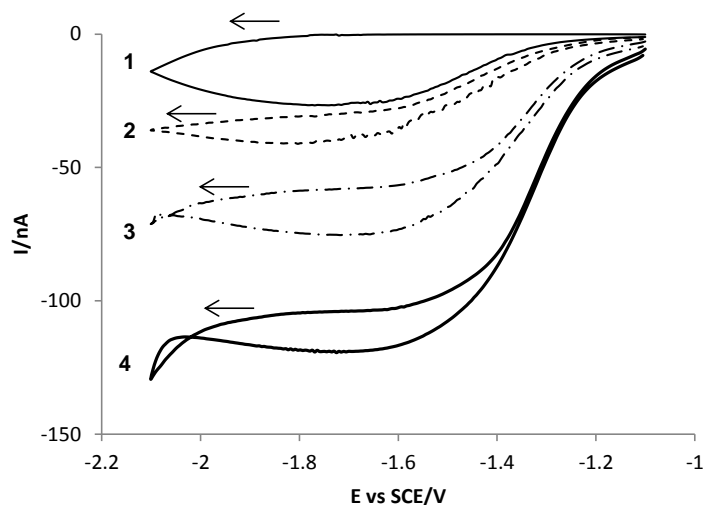
Figure 4.14 - Voltammograms of the S3 ME cycled from -1.1 to -2.1 V repeatedly, showing a progressive current increase due to accumulation of Zn on the surface of the ME.
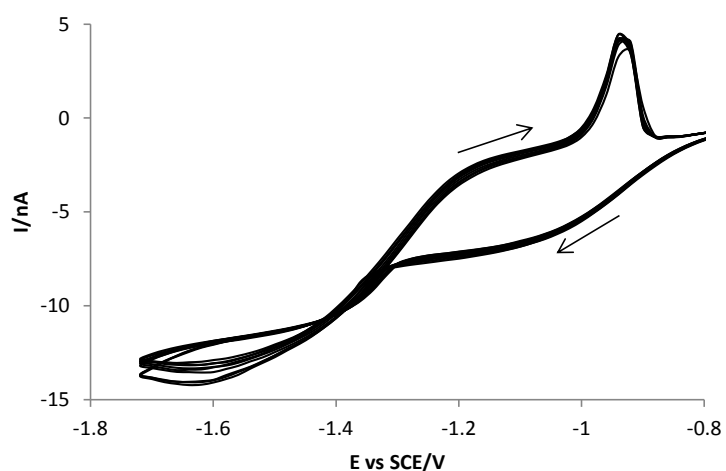
Figure 4.15 - Voltammograms of the S3 ME during ten consecutive cycles from -0.8 to -1.75 V, showing the reproducibility of the measurements if the B-NCD surface is renewed by Zn oxidation to the bulk.

The mapping of the concentration of oxygen and zinc ions was also performed using the developed MEs. A potential of -0.9 V was applied for mapping the distribution of dissolved oxygen, 100 μm above the entire area of the galvanic couple (Figure 4.16). As observed for the line measurements, the current was lower above the metallic regions (lowest above Fe), keeping a constant higher value in the bulk solution surrounding the galvanic couple. A potential of -1.3 V was applied to the tip in order to map the distribution of Zn^{2+} in the same area as for oxygen. The result presented a current

146

increase in the beginning, after which the ME lost the sensibility, showing a nearly invariable current for all the remaining area. This may have been caused by zinc accumulation and surface blocking due to zinc oxide or zinc hydroxide formation, since the local pH above the iron cathode is expected to be considerably higher than in the rest of the NaCl solution, as OH$^-$ is the product of the reduction of dissolved oxygen. Conversely, by mapping only above the zinc anode (Figure 4.17), a current raise was observed above the anodic region, what seems to support the surface blocking hypothesis for the mapping of the full Zn-Fe couple area. Solutions for this problem may outcome from further exploring the growth conditions or surface functionalization of the CVD diamond films.
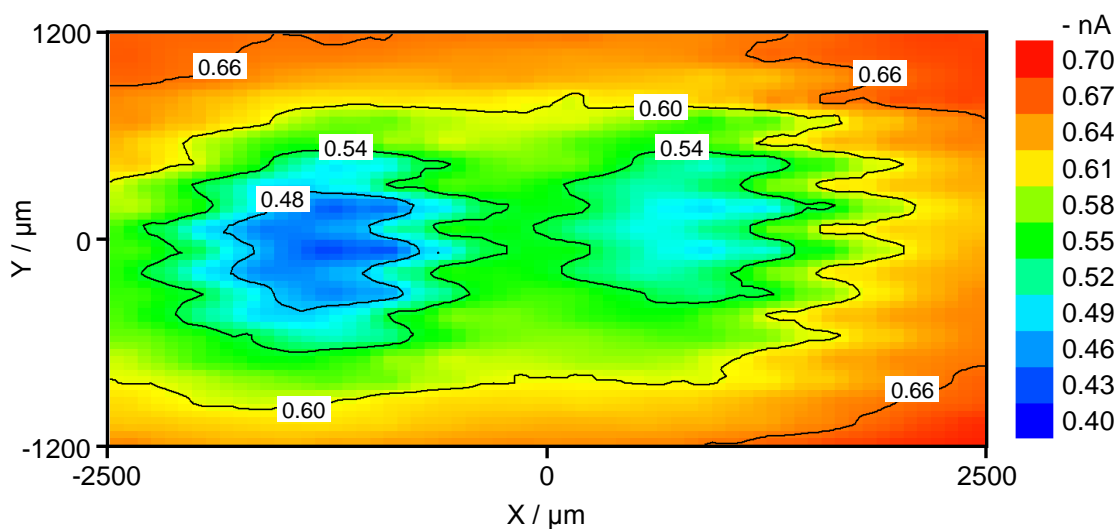
Figure 4.16 - Map of dissolved oxygen detected microamperometrically with a S3 ME polarized at -0.9 V vs. Ag|AgCl.
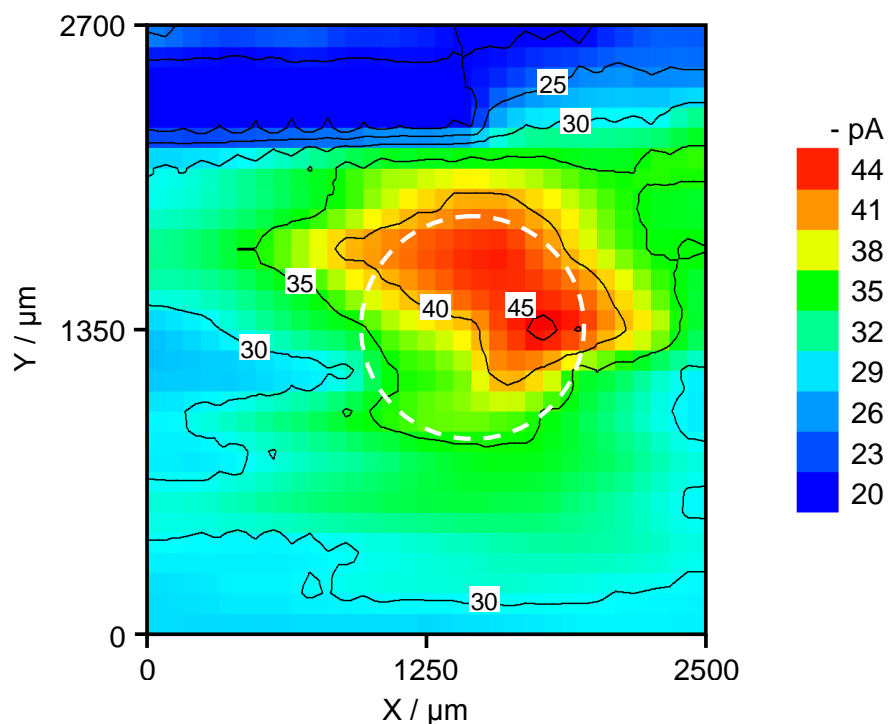
Figure 4.17 - Map of Zn^{2+} detected microamperometrically with a S3 ME polarized at -1.3 V vs Ag|AgCl (the dashed circle indicates the position of the zinc electrode).

4.3.4. Conclusions

Boron doped nanocrystalline diamond microelectrodes were produced and tested towards their prospective use in corrosion studies. The electrodes showed a wide working potential window (~3.5 V) and low background current in 5 mM NaCl, which was the medium intended for the corrosion testing. Good electrochemical reversibility was confirmed with the $Fe(CN)_6^{3-/4-}$ redox system. A linear relationship was found between the zinc reduction current and Zn^{2+} concentrations from 10^{-5} M to 10^{-2} M in a 5 mM NaCl background solution. The microelectrodes were tested as amperometric microprobes to map the oxygen and Zn^{2+} distribution in solution above a Fe-Zn galvanic couple. It was possible to detect, with lateral resolution, the decrease of O_2 near both metals and zinc cations production at the anode. Although B-NCD MEs have shown the capability to detect Zn^{2+}, further optimization is still required to avoid a significant deposition of metallic zinc, which was the main drawback observed.

Acknowledgements

4.4.　　New fluorinated diamond microelectrodes for dissolved oxygen detection

E.L. Silva[*1], A.C Bastos[1], M.A. Neto[1], R.F. Silva[1], M.G.S. Ferreira[1], M.L. Zheludkevich[1,2], F.J. Oliveira[1]

1-CICECO – Department of Materials and Ceramics Engineering, University of Aveiro, Campus Universitário de Santiago, 3810-193 Aveiro, Portugal

2-MagIC, HZG, Geesthacht, Germany

*e-mail: elsilva@ua.pt

Abstract

The present work reports on a novel needle type oxygen microsensor based on boron doped diamond (BDD)with tailored surface aiming in better electrochemical performance. The microelectrodes (ME) are produced by growing diamond films using HFCVD (Hot Filament Chemical Vapor Deposition) on top of electrochemically sharpened tungsten filaments. The diamond is functionalized using CF_4 RF-plasma post-treatments resulting in fluorine termination of the surface.

The quantitative detection of the dissolved oxygen is demonstrated and supported with successful fitting to the theoretical values calculated for diffusion limited current on hemicylinder shape electrode. The developed MEs were calibrated and tested as probes for microamperometric mapping of dissolved oxygen in a Zn-Fe wire-electrode model galvanic couple immersed in 50 mM NaCl. Modified diamond MEs show a faster and more stable response towards oxygen mapping as well as stability for several days of measurements.

4.4.1. Introduction

Dissolved oxygen is one of the prime oxidizing species involved in cellular metabolism as well as in microbiological and corrosion processes [153,265]. In corroding systems, oxygen plays a major role in many cathodic reactions and is a key factor influencing the corrosion potential of a specific material in E-pH diagrams [266]. This influence is best demonstrated when a differential aeration corrosion cell is formed as it often happens in crevices and when biofilms are present. In more common corrosion forms like aqueous and atmospheric corrosion the reduction of dissolved oxygen is the main cathodic process occurring in neutral and alkaline media, being less important at low pH [266]. Access to spatially resolved information on corrosion distribution and mechanisms can be made by localized scanning probe techniques such as SECM [267], SVET [268], SRET [228], micropotentiometry [253], microamperometry [244], etc. The degree of spatial resolution that these techniques provide has motivated their use in various microscopic studies e.g. on galvanic corrosion [269], pitting corrosion [270], examination of defective coatings [271], and "smart" coatings [236], effect of inhibitor addition [272], etc. Clark-type electrodes are the most commonly used oxygen sensors and their function is based on an integrated three-electrode cell insulated in glass [273]. Oxygen permeates through a Teflon or polyethylene membrane at the extremity of the electrode and is reduced at the Pt disk after diffusing through a KCl electrolyte. Introduced in 1953, the reliability of Clark type electrodes for oxygen sensing has even inspired miniaturized versions, although not at a true microscale [274]. Platinum and gold have been demonstrated as suitable alternatives in the form of recessed disk microelectrodes [275,276]. However, the reduction of other species in the potential range of oxygen reduction, electrode fouling in biological environments or surface deactivation after longer measurement periods, in the case of platinum, may interfere with the measurement and impose frequent cleaning and calibration procedures [276].

Boron doped CVD (Chemical Vapor Deposition) polycrystalline diamond has been increasingly attracting the interest of electrochemists as material for electrodes thanks to its well documented electrochemical properties, which include wide electrochemical potential window for water electrolysis, high-signal-to-noise ratio, high chemical stability and resistance to fouling [50,277]. Diamond surfaces are normally hydrogen terminated

under standard growth conditions. Alternatively, options for functionalization with other heteroatoms such as O, F, Cl, and others, can be based on relatively easy procedures. The goal in doing so is to adjust the properties of CVD diamond to the target application [111,278].

Fluorination of diamond surfaces has been reported to allow further expansion of the already wide potential window of diamond for water electrolysis, although reducing the standard rate constant, k_0, for certain redox couples like Eu^{3+}/Eu^{2+}, Fe^{3+}/Fe^{2+} and $Fe[CN]_6^{3-}/Fe[CN]_6^{4-}$ [117]. An important advantage of diamond fluorination is the passivation of sp^2 carbon [279]. The electrochemical contribution of such impurities on diamond, tends to promote the increase of capacitive currents and lower the signal-to-noise ratio [280].

This work reports the fabrication and application of novel oxygen sensitive boron doped diamond microelectrodes modified by CF_4 plasma (F-BDD). After calibration with an optical commercial oxygen sensor device, the plasma modified MEs were used for microamperometric mapping of dissolved oxygen close to the surface of galvanically coupled Zn and Fe model wire-electrodes immersed in a corrosive electrolyte.

4.4.2. Experimental

Boron doped diamond (BDD) microelectrodes were fabricated by coating electrochemically sharpened tungsten filaments with a thin layer of BDD by HFCVD (Hot Filament CVD) techniques. A 91.7% H_2 + 4.6% CH_4 mixture was used for diamond film growth. The remaining 3.7% gas phase was provided by the doping source: a mixture of B_2O_3 dissolved in ethanol, dragged by Argon gas through a gas washing bottle containing the mixture and finally into the CVD chamber. Four tungsten filaments at 2300 ºC provided activation of the gas species with a total chamber pressure of 50 mbar, while the substrate was kept at a constant temperature of 800 ºC. After a growth period of 30 minutes, the methane and boron flow were stopped and the samples were exposed only to activated hydrogen during 30 minutes before cooling down the reactor, to ensure that all the diamond coated tips where H-terminated.

Afterwards the MEs were submitted to a CF_4 RF-plasma (EMITECH K1050X, Quorum Tech., UK) treatment for 5 minutes. In order to evaluate the effect of each plasma on

surface modification, planar tungsten substrates (1X1 cm) were coated with equal diamond films as the ones on the MEs, because of limitations of the equipment for characterizing the small dimensions of the ME tips. Hence, the surface of the planar diamond films was characterized by XPS (X-ray Photoelectron Spectroscopy) (Kratos AXIS Ultra HAS, UK) using an Al Kα X-ray source, before and after plasma modification.

The freshly assembled microelectrodes were calibrated by cyclic voltammetry (Ivium CompactStat potentiostat/galvanostat, Ivium, The Netherlands) with simultaneous comparison to response of an optical O_2 sensor (Hach HQ40d, US). A three electrode configuration with the BDD ME as working electrode, a Pt counter-electrode and an Ag|AgCl reference electrode was used for electrochemical measurements. Both an as-grown BDD and a fluorinated BDD MEs were immersed simultaneously and polarized in turns at a scan rate of 100 mV/s, by shifting the electrical connection. The concentration of dissolved oxygen in a 50 mM NaCl solution was controlled by bubbling argon and a calibration curve was elaborated based on the diffusion limited current of oxygen reduction at the potential of -1.3 V.

A model system consisting of Zn-Fe galvanically coupled wire-electrode cell filled with 50 mM NaCl solution was used to evaluate the applicability of the microelectrodes for localized mapping of the O_2 concentration near active corroding metallic surfaces. Microamperometry measurements were performed with an IPA2 amplifier (Applicable Electronics Inc., USA) in the voltammetric/amperometric mode, using a 2 electrode arrangement, with a Ag|AgCl electrode as counter and reference electrode. 2D X-Y scans were carried out using a microstepping motor driver (USDIGITAL, USA) at a distance of 100 µm between the diamond ME and the surface. X-Z scans permitted obtaining the normal distribution of species above the electrodes. Maps were recorded at -1.3 V (vs. Ag|AgCl) for detection of dissolved O_2.

4.4.3. Results and discussion

4.4.3.1.   Microelectrode surface characterization

The B-doped diamond MEs exhibited a sub-micrometer roughness (100 nm - 1 µm) which allows a good compromise between grain size and minimization of sp^2 impurities. The diamond layers exhibit uniform coverage of the tungsten tips as shown by scanning electron microscopy observation (Figure 4.18). After being submitted to the CF4 plasma treatment, no observable microstructural changes were noticeable (Figure 4.18a-b). This observation is in a good agreement with the results of other authors, after such a short treatment time [281]. The varnish insulation layer covered the full body of the diamond coated tungsten wire with exception of the apex, left uncovered to work as the electroactive surface with ~20 µm extension (Figure 4.18c).
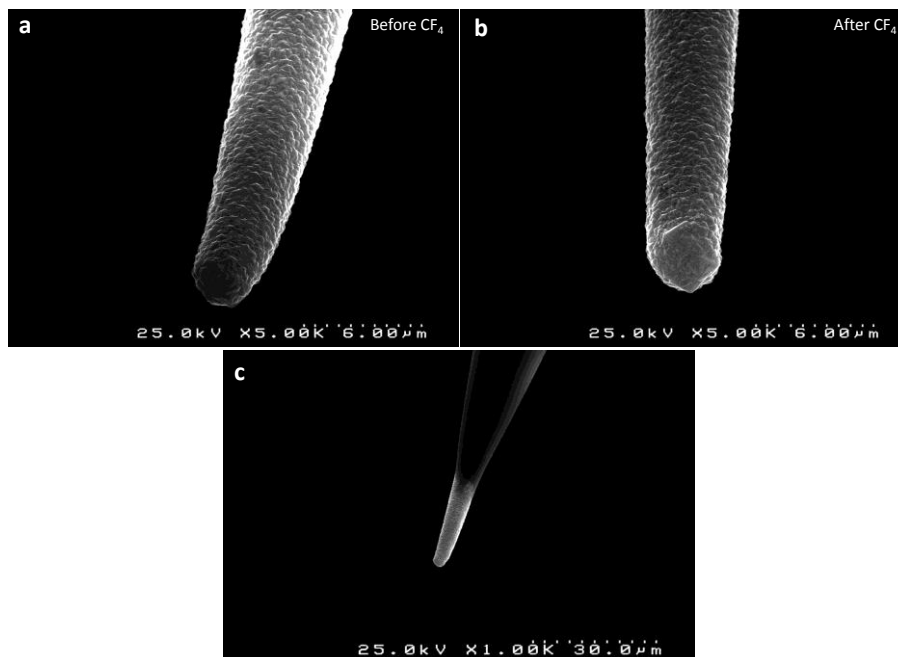
Figure 4.18 - Boron doped diamond microelectrode for which the surface condition a) before and b) after plasma treatment are shown. The insulated microelectrode is shown in c).

In order to evaluate the effect of plasma on surface termination, the surface of the equivalent planar films was analyzed by XPS before and after the treatments. Before plasma treatment a very small O 1s peak is distinguishable most likely because the

boron source (B_2O_3+Et) already contains oxygen (Figure 4.19a). After being exposed to the CF4 plasma, the F1s peaks became much more prominent (Figure 4.19b). Deconvolution of the C1s core level allowed the identification of the different bonding states of the surface carbon atoms. Before fluorination (Figure 4.19c) the diamond surface exhibited high intensity bands at 285, 285.2 and 285.5 eV, assigned to C-C (1), C-H (2) and C-Hx (3) bonds, respectively [282–284]. A higher intensity band at ca. 287 eV was associated to C-O-C (4) bonds, with most probable origin on the doping source. After fluorination (Figure 4.19d), both the C-C and C-H bonding were equally observed. A lower intensity band was identified at ca. 284.2 and assigned to sp^2 carbon (5), most probably deriving from slight amorphization caused by the plasma attack [282,285]. Fluorine associated bands were found at 288.4 and 292.2 eV, associated to C-F (6) and C-F_2 (7) groups, respectively [286,287].
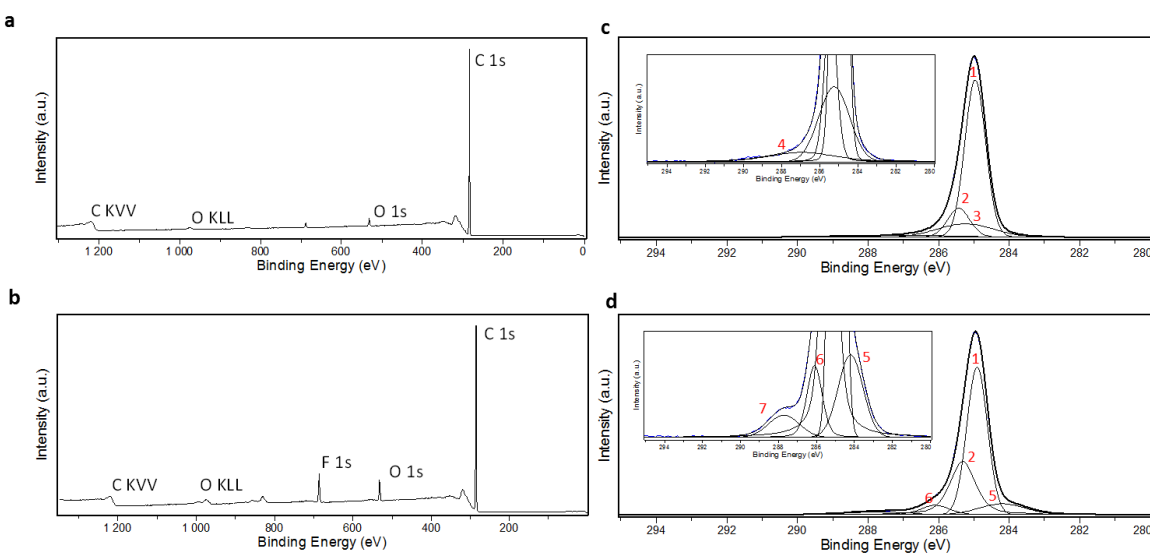
Figure 4.19 - Diamond surface groups determined by XPS for a, c) as grown diamond and b, d) fluorinated diamond.

4.4.3.2.   Calibration of microelectrodes

The calibration procedure for the boron doped diamond MEs was performed at 21.7 º C and 987 mbar with simultaneous amperometric and optical measurement (Figure 4.20a). As-grown and modified microelectrodes were immersed in NaCl 50 mM along with the reference electrode, an optical sensor and the tip of an Argon line. The oxygen

concentration was decreased by stepwise Argon bubbling and voltammetry curves were recorded in turns with each electrode, after the optical sensor showed a stable oxygen concentration. Figure 4.20b and Figure 4.20c show the voltammetric curves of oxygen reduction on the non-treated BDD microelectrode and on the fluorinated one, respectively, with a plateau-like current response in the potential range from ca. -1.2 to -1.6 V. Based on the current values obtained at -1.3 V, calibration curves for both MEs were determined (Figure 4.21a-b). The F-BDD ME showed a strong linear correlation (R2=0.9988) between points and a sensitivity of the electrode of 0.1422 ± 0.006 nA per μM of dissolved oxygen (Figure 4.21b). The detection limit was defined to be 0.63 μM, which is in the same order of previous reports using platinum microdisks [276]. For the as-grown, non-treated, BDD ME (Figure 4.21a), a lower values of linear correlation coefficient is evident, when considering the full O_2 concentration range. By comparing both types of MEs, the non-treated ME exhibits a curvilinear tendency line, corresponding to a correlation between points of 0.969.
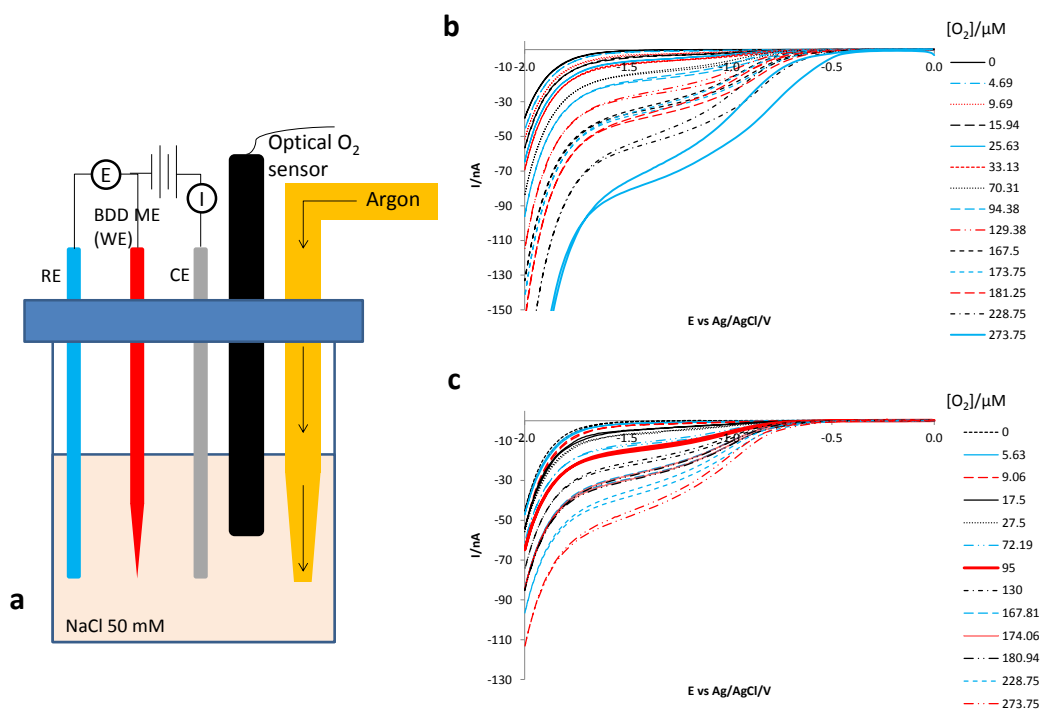
Figure 4.20 - Voltammetry for diamond microelectrode calibration. a) Experimental setup for dissolved oxygen calibration with the measurements were taken in NaCl 50mM for normal oxygen saturation and for successively lower concentrations established by Argon bubbling through the solution; b) and c) Polarization curves taken at 100 mV/s with different oxygen concentrations from 0 to 273.75 μM, at 21.7 °C and 1001 mbar for an as-grown and a F-BDD microelectrode, respectively.

The calibration curve for the F-BDD microelectrode was also fitted according to the theoretical derivation for the diffusion limited quasi-steady state current observed at a hemicylinder (Figure 4.21c and Eq. 4.1) [288], where n is the number of transferred electrons, F is the Faraday constant, A is the electrode area, D is the diffusion coefficient for oxygen (ca. -2.20x10^{-5} cm^2.s^{-1} for pure water [289]), C is the analyte concentration, r is the electrode radius and t is the time of the forward voltammetric scan. Attempts were also made for the conical and prolate hemispheroidal shapes, but none of them fitted the experimental points in an adequate way.

$$i_{qss}^{cylinder} = \frac{2nFADC}{rln\left(\frac{4Dt}{r}\right)}$$

(Eq. 4.1)
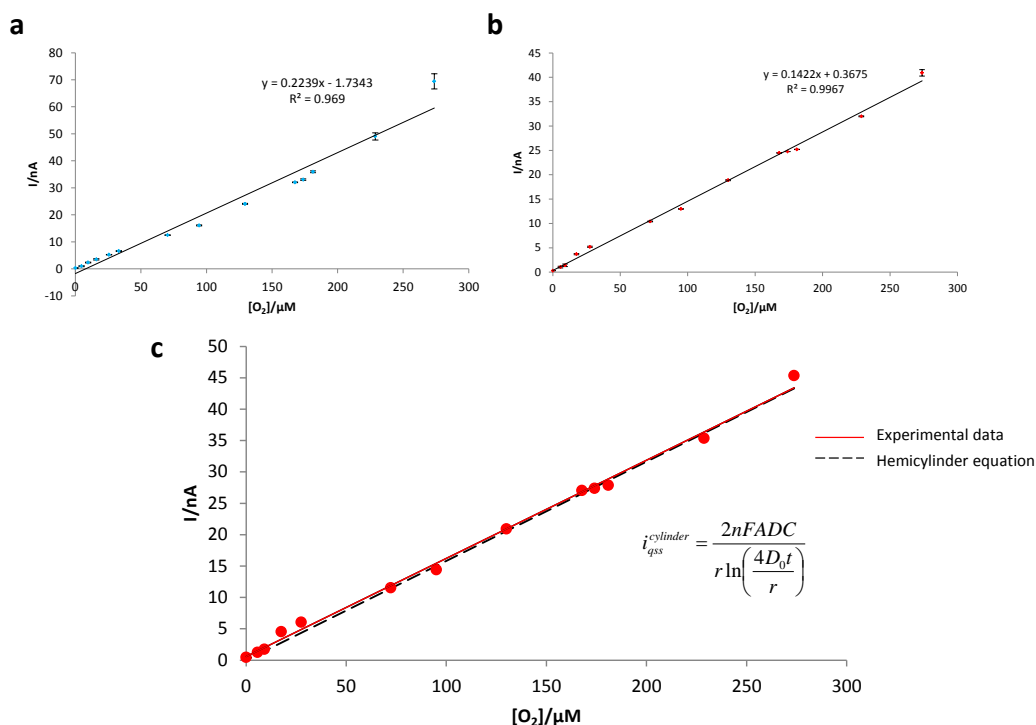
Figure 4.21 - Calibration curves for both electrode types showing a) weak linearity for the as-grown BDD ME (R^2=0.969) and b) stronger correlation between points through the whole concentration range for the F-BDD ME (R^2=0.9967). In c) the calibration curve of the F-BDD ME is reasonably matched by equating the quasi-steady state current of a hemicylinder microelectrode geometry.

4.4.3.3. Microamperometric mapping of dissolved oxygen

The obtained high correlation of the measurement results to the theoretical model confers applicability of the developed F-BDD microelectrode for quantitative detection of dissolved oxygen in aqueous electrolytes. However the microelectrode must also have a fast response time in order to be applicable for localized amperometric mapping.

A model galvanic wire-electrode cell was created for localized electrochemical tests of the newly developed MEs. The main aim of these experiments is to demonstrate the applicability of the developed electrodes for localized corrosion studies. The electrochemical cell is schematically depicted in Figure 4.22a. The maps of oxygen concentration were obtained amperometrically by scanning a 5x2 mm^2 area at 100 µm above the galvanic cell surface. The scans were done with 100 µm point-to-point distance, in a continuous back and forth mode starting from the upper left corner of the rectangular area depicted in Figure 4.22b. The scan rate was adjusted according to waiting time between each ME position, and current averaging time.

The fluorinated diamond ME were polarized at -1.3 V allowing to map the distribution of O_2 (Figure 4.23a). A strong current decrease at the iron cathode was observed due to oxygen reduction at the surface, and less intense current reduction at the anode, caused by the existence of local cathodic regions on zinc originated from additional self-corrosion of this metal. Several MEs were tested, evidencing their reproducibility. A long term stability during several days of measurement was also observed as can be seen from comparison of maps obtained with a fresh electrode and one after 4 days of use (Figure 4.23b).

Furthermore a comparison was made relatively to as-grown MEs, previously demonstrated as viable oxygen sensors [149]. The results are depicted in Figure 4.24. The CF$_4$-treated ME demonstrate fast response for dissolved oxygen mapping, with much lower averaging and waiting times per point, down to 0.01 s for both, with negligible distortion and difference in current intensity (Figure 4.24a-c). Increasing the scan rate in the case of the non-fluorinated microprobes caused an obvious patterning effect due to signal delay as a result of lower responsiveness (higher response time) towards oxygen reduction (Figure 4.24d-e).
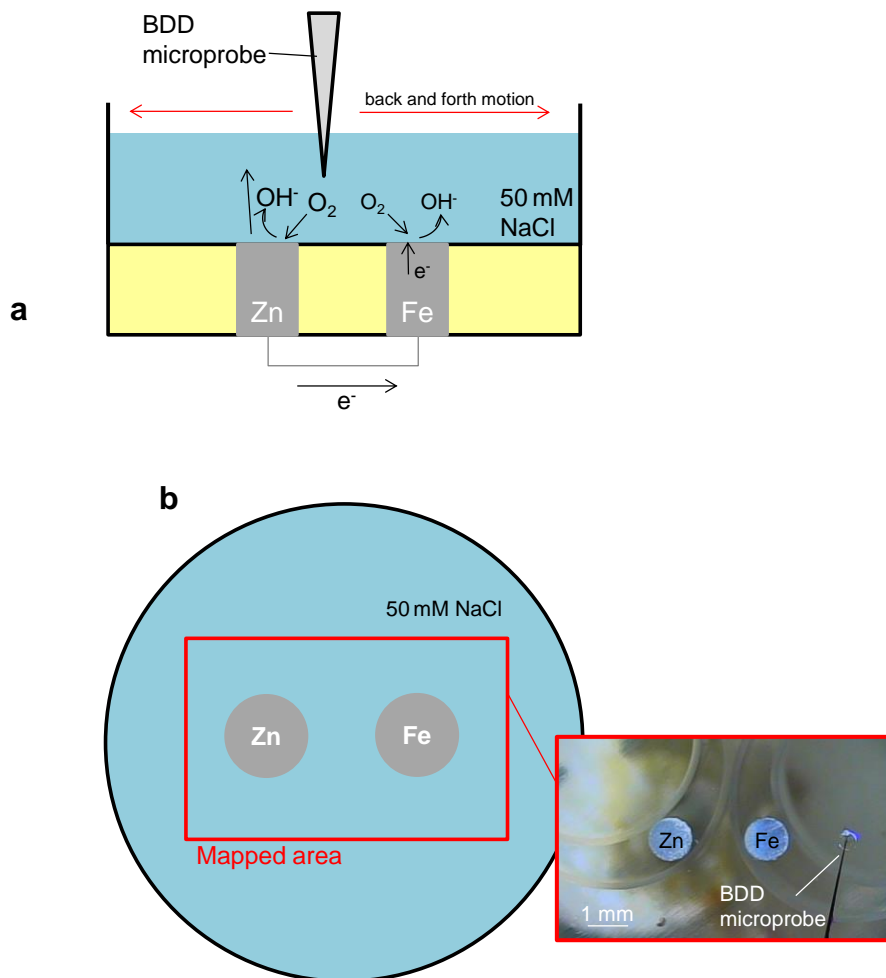
Figure 4.22 - Experimental setup for the microamperometric measurements. (a) Zn-Fe galvanic couple immersed in 50 mM NaCl for dissolved oxygen detection. (b) Schematics of the measurements performed.

Although the current density tends to be lower by the action of surface fluorine groups, these offer a number of advantages. The wider range of water stability of fluorinated diamond ensures that oxygen reduction can occur without interference of hydrogen evolution [117], perfectly isolating the oxygen-due response; the intrinsically low background currents ensure higher detection limit, while the CF_4 plasma treatment *per se* reduces significantly the non-diamond carbon contributions, which are related to undesired adsorption effects, higher double-layer charging current and chemical instability [290].

Hence, upon undergoing fluorination treatment in CF_4 plasma, diamond surfaces exhibited an improved sensing ability for the detection of such a relevant species as

oxygen in corrosion processes, exhibiting a rather fast response, which allows gathering a localized oxygen distribution map in a few minutes.
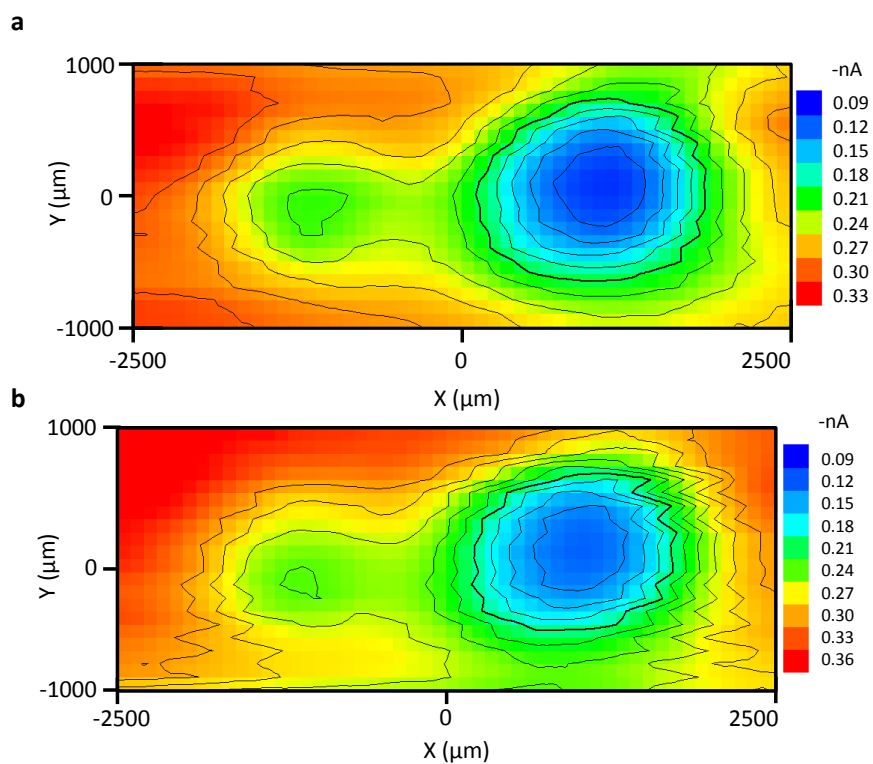
Figure 4.23 - Dissolved oxygen distribution map recorded at -1.3 V with a) a fresh diamond ME modified by CF$_4$ plasma; b) after 4 days of measurement.
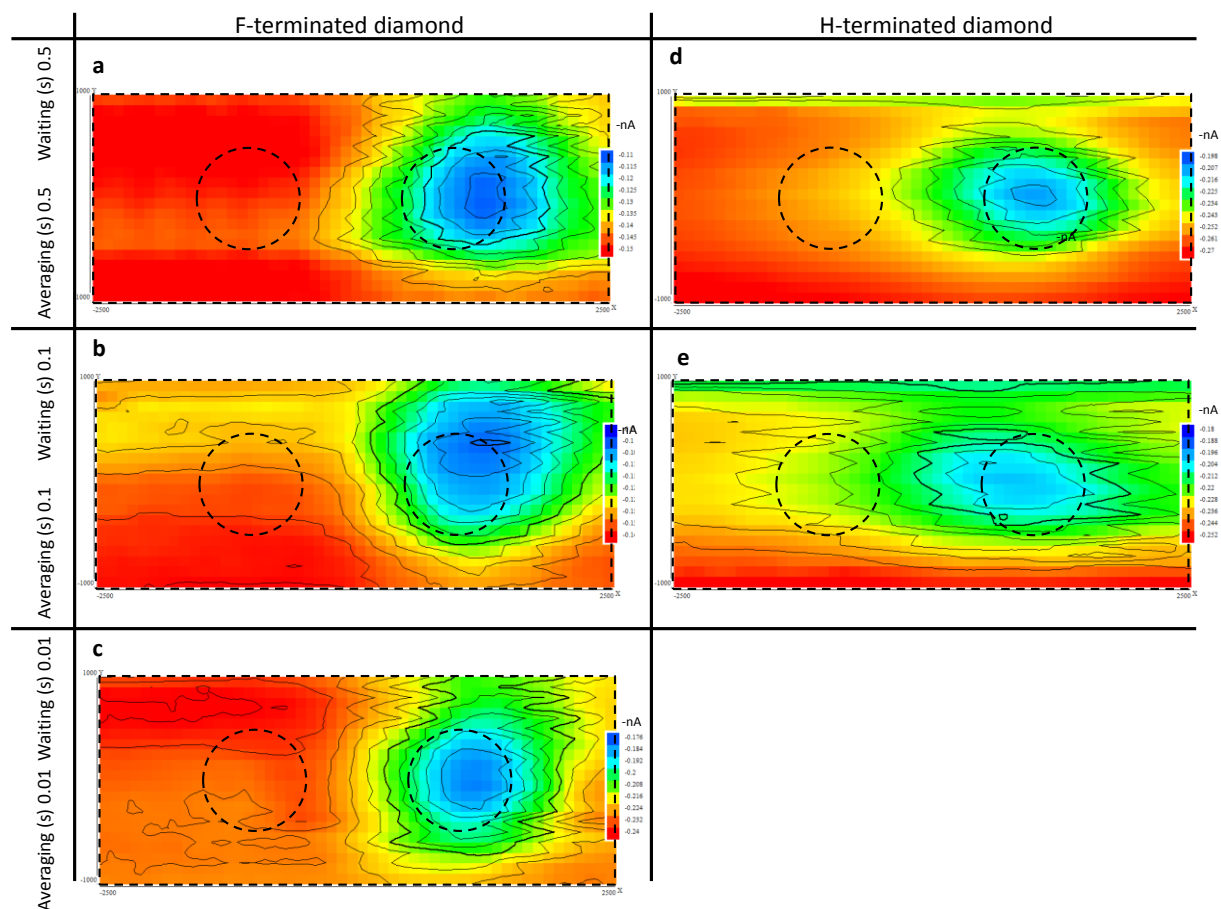
Figure 4.24 - Dissolved oxygen concentration maps recorded with a diamond ME treated with CF_4 plasma and an as-grown ME, polarized at -1.3 and -0.9 V, respectively, with varying averaging-waiting times.

4.4.4. Conclusions

The novel diamond based microelectrode for oxygen detection is reported. The fluorination of diamond-based microelectrodes by CF_4 plasma creates functional C-F groups on the diamond surface that can lead to improvement of sensibility, limit of detection and response time for localized amperometric detection of dissolved oxygen in aqueous electrolyte solutions. Upon calibration with a commercial optical oxygen sensor it was possible to determine a sensitivity of the electrode of 0.1422 ± 0.006 nA/µM of dissolved O_2 with a detection limit of 0.63 µM. By microamperometric tests with a model galvanic cell it was shown that fluorinated diamond MEs can provide

detection of oxygen distribution, exhibiting faster response than the as-grown MEs and also higher longer term stability, especially when higher scanning rates are used. Given their properties and versatility, these new developed diamond-based microelectrodes can now represent a reliable option for challenging localized electrochemical measurements where common electrode solutions are not suitable.

Acknowledgements

4.5.   Novel diamond microelectrode for pH sensing

E.L. Silva*, A.C Bastos, M.A. Neto, R.F. Silva, M.G.S. Ferreira, M.L. Zheludkevich, F.J. Oliveira

CICECO – Department of Materials and Ceramic Engineering

University of Aveiro, Campus Universitário de Santiago, 3810-193 Aveiro, Portugal

*e-mail: elsilva@ua.pt

Abstract

A novel diamond based solid-contact pH-selective microelectrode is reported in the paper for the first time. The diamond films were grown on top of sharp tungsten filaments by HFCVD (Hot Filament Chemical Vapor Deposition). The pH sensitivity of the electrode is achieved via oxygen-termination of the diamond surface with RF oxygen plasma. The MEs were calibrated by zero-current chronopotentiometry registering linearity in the pH 2-12 range. The performance of the diamond microelectrode was demonstrated mapping the pH distribution over corroding Zn-Fe model galvanic cell.

Keywords: diamond; pH-selective microelectrode; HFCVD; galvanic cell

4.5.1. Introduction

The localized sensing of ionic and molecular species close to an active solid-liquid interface is an important challenge for many situations when mechanistic understanding of heterogeneous processes is aimed, e.g., the activity of localized living cell processes, the reactions on electrode surfaces used for energy conversion and corroding metallic surfaces [291]. For localized corrosion, the acidity variation close to the active anodes and cathodes is an important parameter in determining the kinetics of the

electrochemical processes and dictates the local chemistry in the electrolyte close to the active sites [292].

The determination of local pH is commonly done by potentiometric measurements with glass membrane and glass capillary microelectrodes filled with a selective ionophore-based oil-like membrane. These electrodes present some disadvantages like spontaneous leakage of the liquid membrane, short life time and high fragility [19]. Moreover, the sensitivity and selectivity of such electrodes are limited by the adverse effect of trans-membrane ion fluxes in changing the composition of the sample solution near the membrane, which controls the lower detection limit [22]. Overcoming these problems has motivated the development of quite promising novel solid state pH sensors (e.g. polymer membrane based) or improvement of existing ones (e.g. glass membranes, metal/metal oxide sensors) aiming on greater miniaturization and sensibility [293,294].

Sensitivity of CVD diamond to pH has been already reported a number of times now, mainly by integration in ion sensitive field effect transistors (ISFET) [295]. This property adds to others like its inertness in aggressive media and high bio-compatibility, which can confer a stable, long-term operation even in harsh and complex environments [215]. The origin of the pH sensitivity on diamond is still matter of some controversy, but the presence of surface oxygen functionalities seems to be fundamental [295,296]. The mechanism appears to be consistent with the site binding model used to describe the SiO_2/electrolyte interface [297]. Diamond surfaces are normally hydrogen terminated, displaying a hydrophobic character unfavorable for molecular adsorption. Conversely, oxygen-terminated diamond is hydrophilic enabling the formation of differently charged surface groups like C–OH, C–O$^-$ and C–OH$_2^+$, by a protonation-deprotonation mechanism, depending on the proton concentration in solution [295]. Experimental evidence shows that the flatband potential of surface oxidized diamond is pH dependent, which derives from a variation in the charge of the Helmholtz layer induced by the concentration of H$^+$ and OH$^-$ in solution [298].

To our knowledge there are yet no reports on the microscale use of diamod-based microelectrodes for pH sensing.

In this communication we demonstrate the applicability of oxidized diamond microelectrodes as pH sensors for localized electrochemical measurements. The probes exhibited the linear response in the pH range between 2 and 12. The developed microelectrodes were integrated as micropotentiometric probes in a SIET (Scanning Ion-selective Electrode Technique) system for determination of local pH gradients in a corroding Zn-Fe model galvanic micro-cell.

4.5.2. Experimental

Boron doped diamond microelectrodes were fabricated by growing diamond directly on sharp tungsten filaments using the HFCVD (Hot Filament Chemical Vapor Deposition) technique as described elsewhere [149]. A hydrogen rich CH_4-H_2 atmosphere was used for diamond growth. The doping source was B_2O_3 dissolved in ethanol, which was dragged by Argon through a bubbler containing the mixture, into the CVD chamber. After the growth period the methane and boron flow were cut and the samples were exposed only to activated hydrogen during 1h before cooling down the reactor, to ensure that all the diamond coated tips where H-terminated.

Afterwards the MEs were submitted to O_2 RF-plasma (EMITECH K1050X) treatments for 3 minutes. Surface characterization of the diamond films was done before and after plasma modification by XPS (X-ray Photoelectron Spectroscopy) (Kratos AXIS Ultra HAS) using an Al $K\alpha$ X-ray source.

The MEs were then electrically connected to gold plated pins with silver conducting paint (RS Components, UK) for integration with the measurement system.

Commercial pH buffers (Riedel-de Haen) were used for calibration of the MEs from pH 2 to 12.

A galvanic cell consisting of two Zn-Fe wire-electrodes embedded in a cylinder-like epoxy mold was immersed in a 50 mM NaCl solution and used as model system to measure the pH gradient resulting from galvanic corrosion. A homemade AgCl, 0.05 M NaCl electrode worked as external reference electrode. The microelectrode was inserted in a pre-amplifier (input resistance >$1x10^{15}$ Ω) which was mounted in a 3D positioning system and connected to a IPA2 amplifier (input resistance >$1x10^{12}$ Ω). The

instrumentation was manufactured by Applicable Electronics Inc. (USA) and the ASET program (SienceWares, USA) was used to control the measurements and record the data.

4.5.3. Results and discussion

The morphology of the MEs was evaluated by SEM showing a full coverage of the sharp tungsten wires with diamond coatings. The active conical part of the microelectrode has length around 15 µm and apex diameter in the range of 2 µm (Figure 4.25a). Due to size limitations the XPS analysis of the surface ending groups was performed on several planar diamond films, coated at the same time with identical composition to the ones found on the microelectrodes. Before plasma treatment a very small O 1s peak is distinguishable most likely because the boron source (B_2O_3+Et) already contains oxygen (Figure 4.25b). After the oxygen plasma treatment the O 1s peak becomes much more prominent with an O/C ratio of 0.16 (Figure 4.25c).

Deconvolution of the C1s core level allowed the identification of the different bonding states of the surface carbon atoms. In both as-grown and plasma treated diamond surfaces, high intensity peaks were identified at 285 and 285.2 eV, attributed to C-C (peak 1) and C-H bonds (peak 2) respectively (Figure 4.25d) [282,283]. Again, in both cases, peaks with lower intensity were identified from 282.4 to 284.2, which were assigned to sp^2 carbon forms (peak 4) [282,285]. The as-grown films exhibited a peak at 285.5, assigned to C-Hx (peak 3), which was not observed in the plasma treated surfaces. At the oxygen-treated diamond surface the intensity of the C-H and C-C associated peaks was significantly lower than for the untreated case and higher energy peaks from 286 to 288 eV could be well distinguished with most probable origin from carbon bonded to oxygen, C-O-C and C-OH (peak 5), and C=O (peak 6) (Figure 4.25e) [283,285].
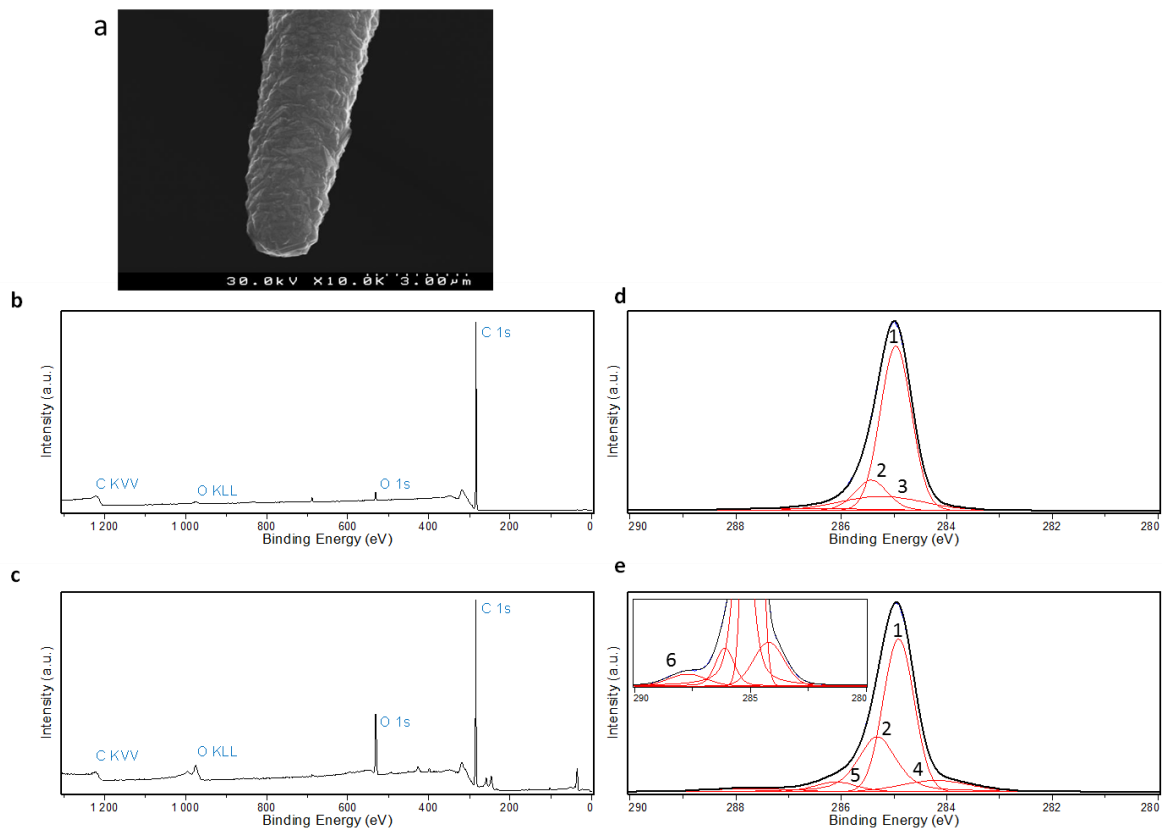
Figure 4.25 - Tip of a diamond microsensor showing a thick, uniform film coverage and XPS spectra of equivalent modified diamond surfaces showing b) and c) surveys of the as-grown diamond and oxygenated diamond surface, respectively; d) and e) C 1s core levels of as-grown diamond and oxygenated diamond surfaces, respectively, showing the lower intensity of the C-H and C-C bonding and appearance of possible C-O-C, C=O and C-OH related features for the latter.

The calibration of pH response of the microelectrodes with standard buffer solutions is depicted in Figure 4.26a. The potential-time steps give a clear indication of the linear behavior achieved with these sensors from pH 2 to pH 12 with approximately 50.8 ± 1.0 mV/pH slope (R^2= 0.9973) (Figure 4.26b) and short response time (t95%<1s) in this range, which is good when comparing to well established pH sensors like glass membrane MEs [299]. This behavior could only be observed with oxidized diamond microelectrodes, for as-grown MEs linearity was absent. Regardless of this non-ideal, near Nernstian behavior, the sensing ability of these MEs for pH profiling was not compromised. Further evidence of this is portrayed in Figure 4.26c showing a potential-time experiment with the same standard solutions in a random way, in which a longer

equilibration time could be observed only in two particular cases, the initial measurement and for sharp pH transitions (e.g. pH9 to 2 in Figure 4.26c). These MEs could operate for at least two days of data recording and several MEs with similar behavior were tested indicating reproducibility of both the measurements and the fabrication method. Thus the microelectrodes provide a fast reproducible response for changes of pH values in a wide interval showing a high potential to be used as high resolution scanning probes.
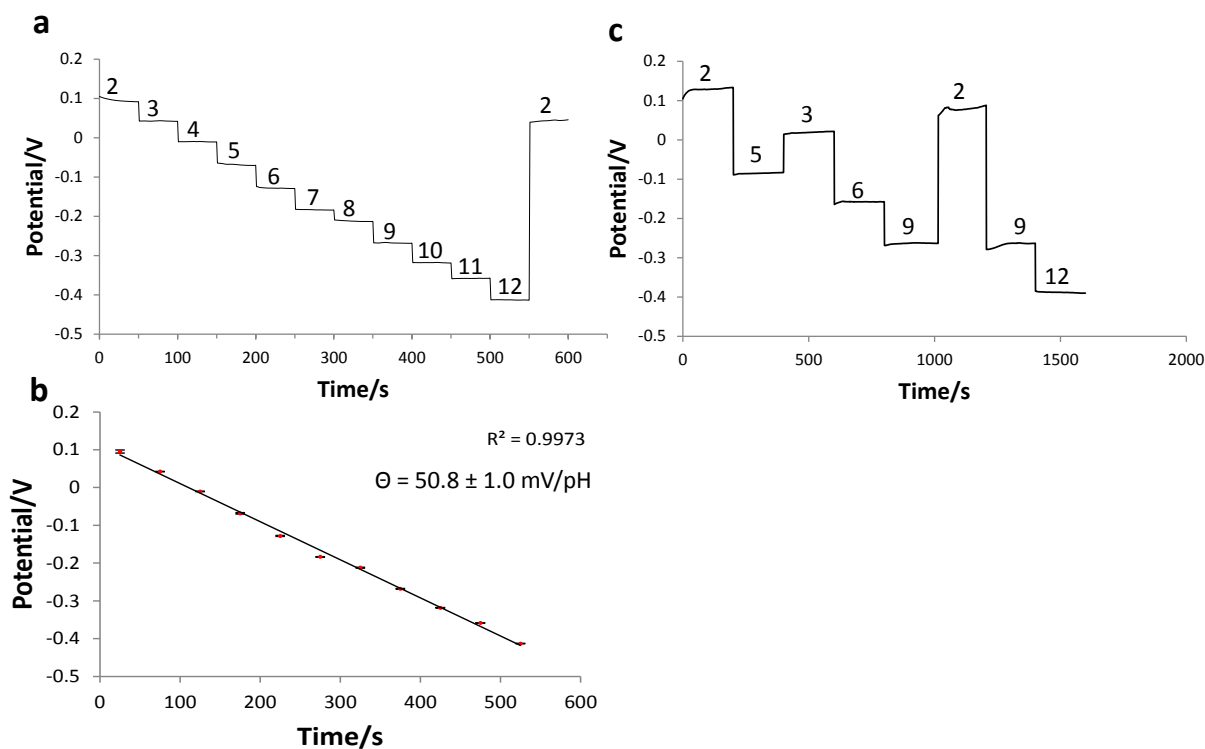
Figure 4.26 - Calibration curve of a diamond pH microsensor showing a) linear range; b) pH sensitivity; c) random pH measurements.

The MEs were also tested to measure the pH variation across the near area (100 μm above) of a Zn-Fe wire-electrode galvanic couple corroding in 50 mM NaCl (Figure 4.27a-b). In this system the zinc anode undergoes anodic dissolution releasing Zn^{2+} according to eq. 4.17. At the cathode OH^- is generated by the reduction of oxygen at the iron surface, according to eq. 4.18. This reaction may proceed from local difference in chemical potential of the zinc surface, although with less significance. The

concentration of available OH⁻ then determines the formation of corrosion products with Zn^{2+}: soluble species like $ZnOH^+$ and $ZnCl^+$ at lower pH or other complexes like $ZnCl_2 \cdot 6Zn(OH)_2$, $Zn(OH)_2$ and ZnO in the more alkaline range [252,259].

$$Zn \rightarrow Zn^{2+} + 2e^- \qquad \text{(Eq. 4.16)}$$
$$O_2 + 2H_2O + 2e^- \rightarrow 4OH^- \qquad \text{(Eq. 4.17)}$$
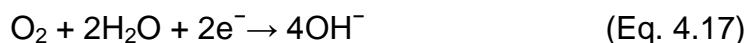
The formation of these species is consequence of localized electrochemical reactions along with mass transportation of the generated ions and the development of chemical reactions as the galvanic corrosion evolves. Consequently, high pH regions will develop above iron, while acidic regions are expected above zinc along with deposition of band-like deposits of the zinc corrosion products at the boundary region between high and low pH zones [259]. The pH above zinc is determined by the concentration of Zn^{2+} conducting the following hydrolysis reaction:

$$Zn^{2+} + H_2O \rightarrow Zn(OH)^+ + H^+ \qquad \text{(Eq. 4.18)}$$
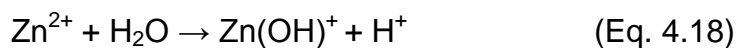
For galvanic corrosion of a Zn/Fe couple in 0.01 M NaCl this concentration usually ranges between ~5-20 mM, after several hours of immersion [252]. Following eq. 4.19, calculations for the expected pH values will be of 4.0 for 1 M Zn^{2+}, 5.0 for 10 mM Zn^{2+} and 6.0 for 0.1 mM Zn^{2+}, accounting only for the influence of anodic dissolution of zinc on pH [300].

The development of respective pH profiles is depicted in Figure 4.27c, representing a micropotentiometric pH map of the Zn-Fe couple by scanning the area with an oxygenated diamond microprobe (Figure 4.27b).

By converting the potential values according to the calibration curve, pH values change between 4.8 above zinc and 9.3 above the iron, which is in good agreement comparing to other studies on this system [259].

These measurements confirm the fast response and usability of diamond microelectrodes for both discrete and continuous pH measurements, despite the

complexity of the corroding media. The limiting influence of ionic species in the behavior of diamond MEs under testing has been previously demonstrated [149].

Hence, diamond MEs present a wide linearity range in comparison to the state-of-the-art for liquid membrane and solid contact microelectrodes. Moreover, their two-step fabrication is simpler and the final product is a robust, highly stable microelectrode adequate for working in corrosion environments and possibly in the always challenging biological environments, given their suitability to do so. Issues like the limit of detection, the response time, and the life time need still to be studied in detail and optimized, but the results shown in this communication seem quite promising.
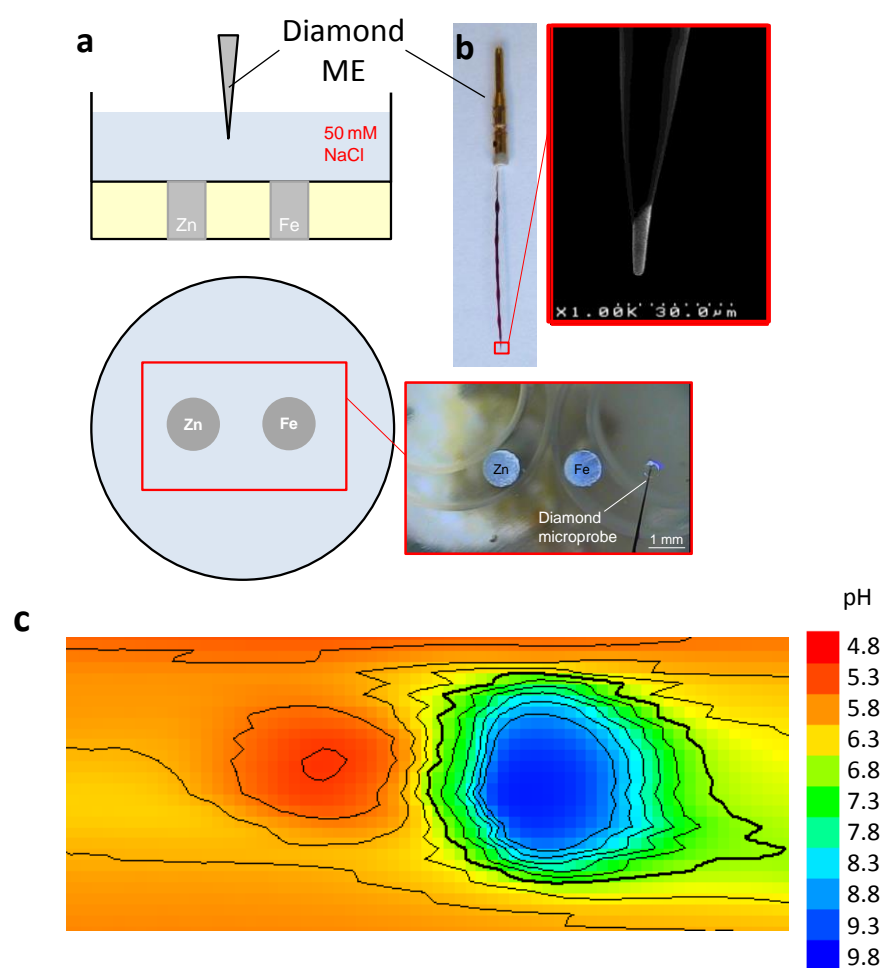
Figure 4.27 - Micropotentiometric measurements showing a) the Zn-Fe galvanic couple immersed in 50 mM NaCl and corresponding area scanned for pH mapping; b) the diamond microsensor; c) pH map of the galvanic couple showing the alkaline cathodic region due to higher concentration of OH^- from oxygen reduction and the acidic region due to hydrolysis of water by Zn^{2+} forming $ZnOH^+$ and H^+.

4.5.4. Conclusions

The pH sensitive microelectrode based on oxygen terminated diamond was developed. H-terminated diamond surfaces were treated by oxygen plasma and modified to contain increased coverage with oxygen functionalities. The presence of possible C-O and C=O groups was observed by XPS with an O/C ratio of 0.16. pH sensitivity of diamond microelectrodes was achieved in this way. The developed microelectrodes show linearity with 50.8 ± 1.0 mV/pH in a wide range from pH 2 to 12. The diamond microelectrode tested on a galvanic Zn-Fe couple immersed in 0.05 M NaCl demonstrates possibility to map pH distribution which varies from ca. 4.8 above the zinc under anodic dissolution and 9.3 over the iron cathodic area due to the high OH^- concentration developing from the reduction of oxygen.

The developed microelectrode is promising when compared to glass-based microelectrodes for various localized pH measurements in systems where fast response, high mechanical and chemical stability is required and micro-scale dimension is a key issue.

5. Conclusions

The work presented in this thesis covers all aspects of boron doped diamond microelectrode fabrication, from substrate preparation to the final application. The main conclusions drawn from this doctoral program are summarized below.

A novel hydrodynamic electrochemical etching method was successfully developed, allowing the transformation of regular tungsten wires into needle shaped substrates with <10 nm radius and high aspect ratio, in less than one minute, by using unsophisticated instrumentation.

The so obtained sharp substrates were coated with conductive boron doped diamond films. A thorough experimental development allowed this process to be done reproducibly by adjustment of the deposition parameters but also of the placement geometry of the substrates inside the reactor chamber.

A study combining TEM and EELS allowed the local microstructural characterization of BDD films in the early stages of growth revealing a mixed crystalline/amorphous carbon interfacial region. Boron was identified by EELS with a concentration of 1.93% but heterogeneous distribution, with possible influence in the diamond (111) lattice, which was found to be expanded by 0.43%.

BDD microelectrodes were characterized electrochemically and tested in model corrosion systems. Overall, the electrodes showed a wide working potential window (3-4V) and low background current in sodium chloride medium, which was also used for corrosion testing. Good electrochemical reversibility was confirmed with the $FcOH^{0/+}$, and the $Fe(CN)_6^{3-/4-}$ redox systems, although the latter redox couple tended to show higher sensitivity to the diamond surface.

The microelectrodes were tested for Zn(II) detection and a log-log linear relationship was found by cyclic voltammetry between the zinc reduction current and Zn^{2+} concentrations from 10^{-5} M to 10^{-2} M in a 5 mM NaCl background solution. As amperometric microprobes, these electrodes allowed to map the oxygen and Zn^{2+} distribution in solution above a Fe-Zn galvanic couple, although a significant deposition of metallic zinc was observed as the main drawback.

Further developments of the microelectrodes were achieved by an adequate functionalization of the diamond surface by plasma treatments. For molecular oxygen detection and mapping, fluorination of diamond microelectrodes by CF_4 plasma was

shown to lead to improved sensibility, limit of detection, response time and longer term stability than as-grown microelectrodes due to the presence of functional C-F groups on the diamond surface. The calibration allowed us to determine a sensitivity of the electrode of 0.1422 ± 0.006 nA/µM of dissolved O_2 with a detection limit of 0.63 µM.

A pH sensitive microelectrode based on oxygen terminated diamond was also developed. By treating the diamond surface in oxygen plasma possible C-O and C=O groups were observed by XPS with an O/C ratio of 0.16. The presence of these groups was observed to be responsible for the pH sensitivity of diamond microelectrodes. The developed microelectrodes showed linearity with 50.8 ± 1.0 mV/pH in a wide range from pH 2 to 12. By testing the diamond microelectrode on a galvanic Zn-Fe couple immersed in 0.05 M NaCl, a pH distribution map showing a variation from ~ 4.8 above the zinc under anodic dissolution to 9.3 over the iron cathodic area, consequence of the high OH^- concentration developing from the reduction of oxygen.

Hence, the developed microelectrodes exhibited a promising range of applications in corrosion research and may be regarded in the future as a solution for localized electrochemical measurements in real systems.

6. Future work

Despite the development, characterization and reasonably successful application of the microelectrodes presented in the previous chapters, there is still a significant portion of knowledge to be acquired about the presented sensors and a good range of unexplored possibilities is to be addressed in the future.

Although a considerable amount of reports can be found in the literature dealing with all the aspects regarding conductive CVD diamond electrodes, the particularities of the diamond films grown in our group entirely justify deeper research on both the microelectrode and especially the macroelectrode form. Considering the scope of applications presented in this work and the initially proposed goals, it would be very interesting to achieve the following: (i) reproducible metal ion detection; (ii) full understanding of metal detection mechanism as well as of the pH and oxygen sensing at the diamond surface level by using a combination of techniques such as Raman mapping, PDEIS (Potentiodynamic Electrochemical Impedance Spectroscopy), XPS and SECM; (iii) application of all-diamond single microelectrodes. This latter point is in a more advanced stage, as can be observed in Figure 6.1 which depicts the final aspect of a recently fabricated all-diamond disk microelectrode.
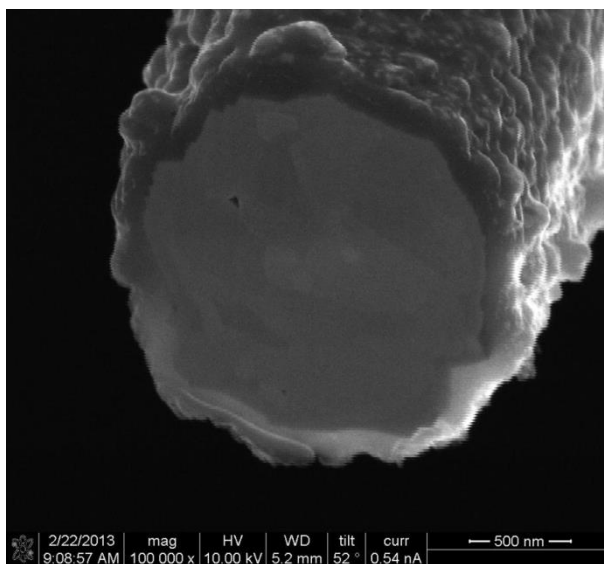
Figure 6.1 – All-diamond microelectrode evidencing the bilayer structure: conductive disk surrounded by insulating outside layer.

Besides the above-mentioned objectives and further exploitation of diamond MEs for research on corrosion systems, the current technological panorama and some demonstrations of interest indicate that the diamond microelectrodes presented in this work have the potential to be applied in other areas, such as diverse biological and environmental studies. A proposal deriving from an international oral presentation suggested the application of diamond MEs as an alternative to carbon fiber in brain research. Recent interest has been demonstrated in the use of diamond MEs to study the influence of polluted environments on the cellular behavior of animals and plants. At a larger scale, the use of diamond macroelectrodes has been considered and used also for the selective treatment of polluted water.

This is thus a theme that covers many branches of science and where much innovative work can still be done.

Bibliography

[1]   G.F. Hays, World Corros. Organ. Pap. (n.d.) 1.

[2]   BCC Research Market Forecasting, Global Markets and Technologies for Sensors, 2013.

[3]   C. Amatore, C. Pebay, L. Thouin, A. Wang, J.-S. Warkocz, Anal. Chem. 82 (2010) 6933.

[4]   W. Kutner, Pure Appl. Chem. 72 (2000) 1483.

[5]   A.M. Bond, Analyst 119 (1994) R1.

[6]   C.G. Zoski, Handbook of Electrochemistry, 1st ed., Elsevier B.V., Amsterdam, 2007.

[7]   R.J. Forster, Chem. Soc. Rev. 23 (1994) 289.

[8]   A.J. Bard, L.R. Faulkner, Electrochemical Methods: Fundamentals and Applications, 2nd ed., Wiley, New York, 2001.

[9]   C.G. Zoski, Electroanalysis 14 (2002) 1041.

[10]   C.M.A. Brett, A.M.O. Brett, Electroanalysis, Oxford University Press, Oxford, 1998.

[11]   M. Cremer, Z. Biol. 29 (1906) 562.

[12]   E. Bakker, E. Pretsch, Anal. Chem. 74 (2002) 420a.

[13]   E. Bakker, E. Pretsch, Trac-Trends Anal. Chem. 27 (2008) 612.

[14]   G. Nagy, L. Nagy, Anal. Lett. 40 (2007) 3.

[15]   G. Eisenmann, D.O. Rudin, J. V. Casby, Science (80-.). 126 (1957) 831.

[16]   E. Pungor, J. Havas, K. Toth, Z. Chem. 5 (1965) 9.

[17]   M.S. Frant, J.W. Ross, Science (80-.). 154 (1966) 1553.

[18]   L.A.R. Pioda, V. Stankova, W. Simon, Anal. Lett. 2 (1969) 665.

[19] D. Amman, Ion-Selective Microelectrodes: Principles, Design and Application, Springer-Verlag, New York, 1986.

[20] A.J. Bard, M. V Mirkin, Scanning Electrochemical Microscopy, Marcel Dekker, New York, 2001.

[21] J. Thomas, A. Craggs, G. Moody, J. Chem. Educ. 51 (1974) 541.

[22] T. Sokalski, A. Ceresa, T. Zwickl, E. Pretsch, J. Am. Chem. Soc. 119 (1997) 11347.

[23] S. V. Lamaka, M.G. Taryba, M.L. Zheludkevich, M.G.S. Ferreira, Electroanalysis 21 (2009) 2447.

[24] B.J. Privett, J.H. Shin, M.H. Schoenfisch, Anal. Chem. 80 (2008) 4499.

[25] E. Pretsch, Trac-Trends Anal. Chem. 26 (2007) 46.

[26] A.J. Bard, G. Inzelt, F. Scholz, Electrochemical Dictionary, Springer-Verlag, Berlin, Heidelberg, 2008.

[27] A.J. Bard, M. Stratmann, F. Scholz, C.J. Pickett, in:, Encycl. Electrochem., Wiley, New York, 2006.

[28] A. Qureshi, W.P. Kang, J.L. Davidson, Y. Gurbuz, Diam. Relat. Mater. 18 (2009) 1401.

[29] I. Rubinstein, A.J. Bard, J. Am. Chem. Soc. 102 (1980) 6641.

[30] P. Ugo, L.M. Moretto, Electroanalysis 7 (1995) 1105.

[31] M. Sheffer, V. Vivier, D. Mandler, Electrochem. Commun. 9 (2007) 2827.

[32] M. Fibbioli, K. Bandyopadhyay, S.G. Liu, L. Echegoyen, O. Enger, F. Diederich, D. Gingery, P. Buhlmann, H. Persson, U.W. Suter, E. Pretsch, Chem. Mater. 14 (2002) 1721.

[33] D. Chen, J. Li, Surf. Sci. Rep. 61 (2006) 445.

[34] G. Bolat, F. Kuralay, G. Eroglu, S. Abaci, Sensors 13 (2013) 8079.

[35] A. Bonnauron, S. Saada, L. Rousseau, G. Lissorgues, C. Mer, P. Bergonzo, M. Bonnauron, Diam. Relat. Mater. 17 (2008) 1399.

[36] A. Pasquarelli, V. Carabelli, Y.L. Xu, E. Colombo, Z.Y. Gao, J. Scharpf, E. Carbone, E. Kohn, Int. J. Environ. Anal. Chem. 91 (2011) 150.

[37] I.J. Cutress, R.G. Compton, Electroanalysis 21 (2009) 2617.

[38] R.L. Whetten, J.T. Khoury, M.M. Alvarez, S. Murthy, I. Vezmar, Z.L. Wang, P.W. Stephens, C.L. Cleveland, W.D. Luedtke, U. Landman, 8 (1996) 428.

[39] J.I. Yeh, H. Shi, Wiley Interdiscip. Rev. Nanomed. Nanobiotechnol. 2 (2010) 176.

[40] C. Punckt, M.A. Pope, J. Liu, Y.H. Lin, I.A. Aksay, Electroanalysis 22 (2010) 2834.

[41] H. Xu, S. Xing, L. Zeng, Y. Xian, G. Shi, L. Jin, J. Electroanal. Chem. 625 (2009) 53.

[42] C. Batchelor-McAuley, C.E. Banks, A.O. Simm, T.G.J. Jones, R.G. Compton, Analyst 131 (2006) 106.

[43] T.-C. Tsai, C.-X. Guo, H.-Z. Han, Y.-T. Li, Y.-Z. Huang, C.-M. Li, J.-J.J. Chen, Analyst 137 (2012) 2813.

[44] A.E. Ross, B.J. Venton, Analyst 137 (2012) 3045.

[45] M. Terrones, Int. Mater. Rev. 49 (2004) 325.

[46] C.N.R. Rao, B.C. Satishkumar, A. Govindaraj, Chemphyschem (2001) 78.

[47] H.O. Pierson, Handbook of Carbon, Graphite, Diamond and Fullerenes - Properties, Processing and Applications, Noyes Publications, Albuquerque, New Mexico, 1995.

[48] R.D.M. de Barros, M.C. Ribeiro, P.T. An-Sumodjo, M.S.D. Juliao, S.H.P. Serrano, N.G. Ferreira, Quim. Nova 28 (2005) 317.

[49] F.G. Celii, J.E. Butler, Annu Rev Phys Chem 42 (1991) 643.

[50] A.F. Azevedo, M.R. Baldan, N.G. Ferreira, Int. J. Electrochem. 2012 (2012) 1.

[51] Y.K. Kim, J.H. Jung, J.Y. Lee, H.J. Ahn, J. Mater. Sci. Electron. 6 (1995) 28.

[52] J.J. Lee, S.F. Komarov, J.B. Hudson, E.B. Stokes, M.P. DEvelyn, Diam. Relat. Mater. 6 (1997) 511.

[53] N.G. Ferreira, E.J. Corat, V.J. Trava-Airoldi, N.F. Leite, Diam. Relat. Mater. 9 (2000) 368.

[54] Y. Liou, Y.R. Ma, Diam. Relat. Mater. 3 (1994) 573.

[55] D. Zhou, D.M. Gruen, L.C. Qin, T.G. McCauley, A.R. Krauss, J. Appl. Phys. 84 (1998) 1981.

[56] D.M. Gruen, Annu. Rev. Mater. Sci. 29 (1999) 211.

[57] L.L.G. Silva, Eletrodos Em Diamante CVD Para Estudos Eletroquímicos, Instituto Tecnológico de Aeroáutica, 2001.

[58] P. May, Philos. Trans. R. Soc. London A (2000) 473.

[59] J. Ristein, Semicond. Semimetals 77 (2004) 37.

[60] J. Ristein, Diam. Relat. Mater. 9 (2000) 1129.

[61] R. Sussmann, CVD Diamond for Electronic Devices and Sensors, John Wiley & Sons Ltd, Chichester, UK, 2009.

[62] G.R. Salazar-Banda, L.S. Andrade, P.A.P. Nascente, P.S. Pizani, R.C. Rocha-Filho, L.A. Avaca, Electrochim. Acta 51 (2006) 4612.

[63] I. Duo, C. Levy-Clement, A. Fujishima, C. Comninellis, J. Appl. Electrochem. 34 (2004) 935.

[64] J. Ristein, Appl. Phys. A 82 (2005) 377.

[65] M.I. Landstrass, K. V Ravi, Appl. Phys. Lett. 55 (1989) 1391.

[66] F. Maier, M. Riedel, B. Mantel, J. Ristein, L. Ley, Phys. Rev. Lett. 85 (2000) 3472.

[67] A. Denisenko, A. Romanyuk, C. Pietzka, J. Scharpf, E. Kohn, Diam. Relat. Mater. 19 (2010) 423.

[68] M. Wang, N. Simon, C. Decorse-Pascanut, M. Bouttemy, A. Etcheberry, M.S. Li, R. Boukherroub, S. Szunerits, Electrochim. Acta 54 (2009) 5818.

[69] Y. Coffinier, S. Szunerits, C. Jama, R. Desmet, O. Melnyk, B. Marcus, L. Gengembre, E. Payen, D. Delabouglise, R. Boukherroub, Langmuir 23 (2007) 4494.

[70] A. Kraft, Int. J. Electrochem. Sci. 2 (2007) 355.

[71] Y. V. Pleskov, Prot. Met. 42 (2006) 103.

[72] M. Schwander, K. Partes, Diam. Relat. Mater. 20 (2011) 1287.

[73] Z.M. Shah, A. Mainwood, Diam. Relat. Mater. 17 (2008) 1307.

[74] H. Kato, D. Takeuchi, N. Tokuda, H. Umezawa, H. Okushi, S. Yamasaki, Diam. Relat. Mater. 18 (2009) 782.

[75] F. Brunet, P. Germi, M. Pernet, A. Deneuville, E.G.F. Laugier, M. Burdin, G. Rolland, Diam. Relat. Mater. 7 (1998) 869.

[76] J. Chevallier, Semicond. Semimetals 77 (2004) 1.

[77] A. Deneuville, Semicond. Semimetals 76 (2003) 183.

[78] P. Gonon, A. Deneuville, F. Fontaine, E. Gheeraert, A. Campargue, M. Chenevier, S. Rodolphe, J. Appl. Phys. 78 (1995) 7404.

[79] V.V.S.S. Srikanth, P. Sampath Kumar, V.B. Kumar, Int. J. Electrochem. 2012 (2012) 1.

[80] R. Haubner, S. Bohr, B. Lux, Diam. Relat. Mater. 8 (1999) 171.

[81] J.H. Won, a. Hatta, H. Yagyu, N. Jiang, Y. Mori, T. Ito, T. Sasaki, a. Hiraki, Appl. Phys. Lett. 68 (1996) 2822.

[82] P. Ashcheulov, J. Šebera, a. Kovalenko, V. Petrák, F. Fendrych, M. Nesládek, a. Taylor, Z. Vlčková Živcová, O. Frank, L. Kavan, M. Dračínský, P. Hubík, J. Vacík, I. Kraus, I. Kratochvílová, Eur. Phys. J. B 86 (2013) 443.

[83] A. Fujishima, Y. Einaga, T.N. Rao, D.A. Tryk, Diamond Electrochemistry, Elsevier Science, Amsterdam, 2005.

[84] M.N.R. Ashfold, P.W. May, J.R. Petherbridge, K.N. Rosser, J.A. Smith, Y.A. Mankelevich, N. V. Suetin, Phys. Chem. Chem. Phys. 3 (2001) 3471.

[85] Y.A. Mankelevich, A.T. Rakhimov, N. V Suetin, Diam. Relat. Mater. 7 (1998) 1133.

[86] M.C. McMaster, W.L. Hsu, M.E. Coltrin, D.S. Dandy, J. Appl. Phys. 76 (1994) 7567.

[87] A. Wang, K. Lee, C. Sun, L. Wen, J. Mater. Sci. Technol. 22 (2006) 599.

[88] Praxair, Diborane, Praxair Material Safety Data Sheet, 2009.

[89] J.R. Petherbridge, P.W. May, M.N.R. Ashfold, J. Appl. Phys. 89 (2001) 5219.

[90] Y.A. Mankelevich, M.N.R. Ashfold, D.W. Comerford, J. Ma, J.C. Richley, Thin Solid Films 519 (2011) 4421.

[91] K.B. Holt, A.J. Bard, Y. Show, G.M. Swain, J. Phys. Chem. B 108 (2004) 15117.

[92] S.-H. Baek, N.J. Curro, E. a Ekimov, V. a Sidorov, E.D. Bauer, J.D. Thompson, Supercond. Sci. Technol. 22 (2009) 065008.

[93] J.P. Goss, P.R. Briddon, S.J. Sque, R. Jones, Phys. Rev. B 69 (2004).

[94] J. Chevallier, A. Lusson, D. Ballutaud, B. Theys, F. Jomard, A. Deneuville, M. Bernard, E. Gheeraert, E. Bustarret, Diam. Relat. Mater. 10 (2001) 399.

[95] M. Gabrysch, S. Majdi, A. Hallén, M. Linnarsson, A. Schöner, D. Twitchen, J. Isberg, Phys. Status Solidi 205 (2008) 2190.

[96] J.P. Goss, R.J. Eyre, P.R. Briddon, Phys. Status Solidi 245 (2008) 1679.

[97] W. Gajewski, P. Achatz, O. Williams, K. Haenen, E. Bustarret, M. Stutzmann, J. Garrido, Phys. Rev. B 79 (2009) 045206.

[98] Y. V Pleskov, A.Y. Sakharova, M.D. Krotova, L.L. Bouilov, B. V Spitsyn, J. Electroanal. Chem. 228 (1987) 19.

[99] N. Tsubouchi, M. Ogura, A. Chayahara, H. Okushi, Diam. Relat. Mater. 17 (2008) 498.

[100] T.N. Rao, A. Fujishima, Diam. Relat. Mater. 9 (2000) 384.

[101] E. Brillas, C.A. Martınez-Huitle, Synthetic Diamond Films: Preparation, Electrochemistry, Characterization, and Applications, Hoboken, New Jersey, 2011.

[102] Y. V Pleskov, Russ. Chem. Rev. 68 (1999) 381.

[103] Y. V. Pleskov, Y.E. Evstefeeva, V.P. Varnin, I.G. Teremetskaya, Russ. J. Electrochem. 40 (2004) 886.

[104] Y. V. Pleskov, Y.E. Evstefeeva, M.D. Krotova, P.Y. Lim, H.C. Shih, V.P. Varnin, I.G. Teremetskaya, I.I. Vlasov, V.G. Ralchenko, J. Appl. Electrochem. 35 (2005) 857.

[105] I. Duo, A. Fujishima, C. Comninellis, Electrochem. Commun. 5 (2003) 695.

[106] H. V Patten, K.E. Meadows, L.A. Hutton, J.G. Iacobini, D. Battistel, K. McKelvey, A.W. Colburn, M.E. Newton, J. V Macpherson, P.R. Unwin, Angew. Chem. Int. Ed. 51 (2012) 7002.

[107] I. Yagi, H. Notsu, T. Kondo, D.A. Tryk, A. Fujishima, J. Electroanal. Chem. 473 (1999) 173.

[108] H. Notsu, I. Yagi, T. Tatsuma, D.A. Tryk, A. Fujishima, Electrochem. Solid State Lett. 2 (1999) 522.

[109] D.A. Tryk, H. Tachibana, H. Inoue, A. Fujishima, Diam. Relat. Mater. 16 (2007) 881.

[110] S. Ferro, A. De Battisti, Anal. Chem. 75 (2003) 7040.

[111] T. Kondo, H. Ito, K. Kusakabe, K. Ohkawa, Y. Einaga, A. Fujishima, T. Kawai, Electrochim. Acta 52 (2007) 3841.

[112] M. Karlsson, P. Forsberg, F. Nikolajeff, Langmuir 26 (2010) 889.

[113] A. Freedman, J. Appl. Phys. 75 (1994) 3112.

[114] A.K. Tiwari, J.P. Goss, P.R. Briddon, N.G. Wright, A.B. Horsfall, R. Jones, H. Pinto, M.J. Rayson, Phys. Status Solidi a-Applications Mater. Sci. 209 (2012) 1709.

[115] S. Hadenfeldt, C. Benndorf, Surf. Sci. 402 (1998) 227.

[116] C.P. Kealey, T.M. Klapotke, D.W. McComb, M.I. Robertson, J.M. Winfield, J. Mater. Chem. 11 (2001) 879.

[117] S. Ferro, A. De Battisti, J. Phys. Chem. B 107 (2003) 7567.

[118] J.B. Cooper, S. Pang, S. Albin, J. Zheng, R.M. Johnson, Anal. Chem. 70 (1998) 464.

[119] Y. Zhou, J. Zhi, Talanta 79 (2009) 1189.

[120] C.A. Martinez-Huitle, Small 3 (2007) 1474.

[121] H. Dong, S. Wang, J.J. Galligan, G.M. Swain, Front. Biosci. 3 (2011) 518.

[122] G.W. Muna, V. Quaiserova-Mocko, G.M. Swain, Electroanalysis 17 (2005) 1160.

[123] J.H.T. Luong, K.B. Male, J.D. Glennon, Analyst 134 (2009) 1965.

[124] N.S. Lawrence, M. Pagels, A. Meredith, T.G.J. Jones, C.E. Hall, C.S.J. Pickles, H.P. Godfried, C.E. Banks, R.G. Compton, L. Jiang, Talanta 69 (2006) 829.

[125] S. Hrapovic, Y.L. Liu, J.H.T. Luong, Anal. Chem. 79 (2007) 500.

[126] S. Xie, G. Shafer, C.G. Wilson, H.B. Martin, Diam. Relat. Mater. 15 (2006) 225.

[127] E. Bitziou, D. O'Hare, B.A. Patel, Anal. Chem. 80 (2008) 8733.

[128] A. Suzuki, T.A. Ivandini, K. Yoshimi, A. Fujishima, G. Oyama, T. Nakazato, N. Hattori, S. Kitazawa, Y. Einaga, Anal. Chem. 79 (2007) 8608.

[129] K.B. Holt, J.P. Hu, J.S. Foord, Anal. Chem. 79 (2007) 2556.

[130] S. Fierro, M. Yoshikawa, O. Nagano, K. Yoshimi, H. Saya, Y. Einaga, Sci. Rep. 2 (2012).

[131] A. Avdic, A. Lugstein, M. Wu, B. Gollas, I. Pobelov, T. Wandlowski, K. Leonhardt, G. Denuault, E. Bertagnolli, Nanotechnology 22 (2011) 145306.

[132] R.M. Wightman, Anal Chem 53 (1981) 1125a.

[133] M. Fleischmann, S. Pons, Anal Chem 59 (1987) 1391a.

[134] A. Molina, J. Gonzalez, M.C. Henstridge, R.G. Compton, J. Phys. Chem. C 115 (2011) 4054.

[135] M. Fleischmann, S. Pons, D.R. Rolison, P. Schmidt, Ultramicroelectrodes, Datatech Systems, 1987.

[136] B.-F. Ju, Y.-L. Chen, Y. Ge, Rev. Sci. Instrum. 82 (2011) 013707.

[137] M.C. Baykul, Mater. Sci. Eng. B 74 (2000) 229.

[138] Y. Ge, W. Zhang, Y.-L. Chen, C. Jin, B.-F. Ju, J. Mater. Process. Technol. 213 (2013) 11.

[139] E.L. Silva, M.A. Neto, A.J.S. Fernandes, A.C. Bastos, R.F. Silva, M.L. Zheludkevich, F.J. Oliveira, Diam. Relat. Mater. 19 (2010) 1330.

[140] D.R. Lide, CRC Handbook of Chemistry and Physics, 74th ed., CRC Press, Boca Raton, Florida, 1993.

[141] M. Pourbaix, Atlas of Electrochemical Equilibria in Aqueous Solutions, NACE, Houston, Texas, 1974.

[142] M.A. Neto, E.L. Silva, A.J.S. Fernandes, F.J. Oliveira, R.F. Silva, Surf. Coat. Technol. 206 (2012) 3055.

[143] H. Pierson, Handbook of Refractory Carbides and Nitrides: Properties, Characteristics, Processing and Applications, Noyes Publications, Westwood, New Jersey, 1996.

[144] A. Warren, A. Nylund, I. Olefjord, Int. J. Refract. Met. Hard Mater. 14 (1996) 345.

[145] K.M. Andersson, L. Bergstr, Int. J. Refract. Metals Hard Mater. 18 (2000) 121.

[146] D.J. Ham, J.S. Lee, Energies 2 (2009) 873.

[147] J. Izquierdo, L. Nagy, J.J. Santana, G. Nagy, R.M. Souto, Electrochim. Acta 58 (2011) 707.

[148] S. V. Lamaka, O. V. Karavai, A.C. Bastos, M.L. Zheludkevich, M.G.S. Ferreira, Electrochem. Commun. 10 (2008) 259.

[149] E.L. Silva, A.C. Bastos, M.A. Neto, R.F. Silva, M.L. Zheludkevich, M.G.S. Ferreira, F.J. Oliveira, Electrochim. Acta 76 (2012) 487.

[150] T. Kihara, N. Yoshida, T. Kitagawa, C. Nakamura, N. Nakamura, J. Miyake, Biosens. Bioelectron. 26 (2010) 1449.

[151] P. Sun, F.O. Laforge, T.P. Abeyweera, S.A. Rotenberg, J. Carpino, M. V. Mirkin, Proc. Natl. Acad. Sci. U. S. A. 105 (2008) 443.

[152] P. Sun, M. V Mirkin, Anal. Chem. 78 (2006) 6526.

[153] R.M. Wightman, 311 (2012) 1570.

[154] X. Xie, D. Stueben, Z. Berner, Anal. Lett. 38 (2005) 2281.

[155] T. Nishimura, A.M.A. Hassan, M. Tomitori, Appl. Surf. Sci. 284 (2013) 715.

[156] P. McDonnell, T. Graveson, C. Rackson, W.J. Kim, J. Phys. Chem. Solids 74 (2013) 30.

[157] J.W. Choi, G.H. Hwang, S.G. Kang, Met. Mater. Int. 12 (2006) 81.

[158] J. Sutanto, R.L. Smith, S.D. Collins, J. Micromechanics Microengineering 20 (2010) 045016.

[159] M. Kulawik, M. Nowicki, G. Thielsch, L. Cramer, H.-P. Rust, H.-J. Freund, T.P. Pearl, P.S. Weiss, Rev. Sci. Instrum. 74 (2003) 1027.

[160] M. Klein, G. Schwitzgebel, Rev. Sci. Instrum. 68 (1997) 3099.

[161] A.-D. Müller, F. Müller, M. Hietschold, F. Demming, J. Jersch, K. Dickmann, Rev. Sci. Instrum. 70 (1999) 3970.

[162] A.K. Kar, S. Gangopadhyay, B.K. Mathur, 1426 (2000).

[163] Y. Nakamura, Y. Mera, K. Maeda, Rev. Sci. Instrum. 70 (1999) 3373.

[164] B.-F. Ju, Y.-L. Chen, M. Fu, Y. Chen, Y. Yang, Sensors Actuators A Phys. 155 (2009) 136.

[165] R. Fainchtein, P.R. Zarriello, Ultramicroscopy 44 (1992) 1533.

[166] W.X. Sun, Z.X. Shen, F.C. Cheong, G.Y. Yu, K.Y. Lim, J.Y. Lin, Rev. Sci. Instrum. 73 (2002) 2942.

[167] D. Xu, K.M. Liechti, K. Ravi-Chandar, Rev. Sci. Instrum. 78 (2007) 073707.

[168] X. Chen, J. Cheng, (2003).

[169] D.A. Saville, (1997) 27.

[170] M. Kulawik, M. Nowicki, G. Thielsch, L. Cramer, H.-P. Rust, H.-J. Freund, T.P. Pearl, P.S. Weiss, Rev. Sci. Instrum. 74 (2003) 1027.

[171] W.X. Sun, Z.X. Shen, F.C. Cheong, G.Y. Yu, K.Y. Lim, J.Y. Lin, Rev. Sci. Instrum. 73 (2002) 2942.

[172] A.I. Oliva, J.L. Pen, E. Anguiano, M. Aguilar, I. Introduction, 67 (1996) 1917.

[173] D. Xu, K.M. Liechti, K. Ravi-Chandar, Rev. Sci. Instrum. 78 (2007) 073707.

[174] E.L. Silva, A.C. Bastos, M.A. Neto, R.F. Silva, M.G.S. Ferreira, M.L. Zheludkevich, F.J. Oliveira, Electrochem. Commun. 40 (2013) 31.

[175] K. V. Ravi, C.A. Koch, Appl. Phys. Lett. 57 (1990) 348.

[176] J. Singh, M. Vellaikal, J. Appl. Phys. 73 (1993) 2831.

[177] A.A. Morrish, P.E. Pehrsson, Appl. Phys. Lett. 59 (1991) 417.

[178] Z. Feng, K. Komvopoulos, I.G. Brown, D.B. Bogy, J. Appl. Phys. 74 (1993) 2841.

[179] W. Kulisch, C. Popov, Phys. Status Solidi 203 (2006) 203.

[180] S.-T. Lee, Z. Lin, X. Jiang, Mater. Sci. Eng. R Reports 25 (1999) 123.

[181] M. Amaral, A.J.S. Fernandes, M. Vila, F.J. Oliveira, R.F. SIlva, Diam. Relat. Mater. 15 (2006) 1822.

[182] Y. V. Pleskov, 38 (2002) 1275.

[183] J. Hu, J.S. Foord, K.B. Holt, Phys. Chem. Chem. Phys. 9 (2007) 5469.

[184] A. Zimmer, O.A. Williams, K. Haenen, H. Terryn, Appl. Phys. Lett. 93 (2008) 131910.

[185] C.J.H. Wort, R.S. Balmer, Mater. Today 11 (2008) 22.

[186] H. Spicka, M. Griesser, H. Hutter, M. Grasserbauer, S. Bohr, R. Haubner, B. Lux, Diam. Relat. Mater. 5 (1996) 383.

[187] M. Nesladek, J.J. Mares, D. Tromson, C. Mer, P. Bergonzo, P. Hubik, J. Kristofik, Sci. Technol. Adv. Mater. 7 (2006) S41.

[188] C. Prado, G. Flechsig, P. Grundler, J.S. Foord, F. Marken, R.G. Compton, Analyst 127 (2002) 329.

[189] T.A. Ivandini, B. V. Sarada, T.N. Rao, A. Fujishima, Analyst 128 (2003) 924.

[190] J. Cvacka, V. Quaiserová, J. Park, Y. Show, A. Muck, G.M. Swain, Anal. Chem. 75 (2003) 2678.

[191] K.L. Soh, W.P. Kang, J.L. Davidson, Y.M. Wong, D.E. Cliffel, G.M. Swain, Diam. Relat. Mater. 17 (2008) 900.

[192] S. Basu, W.P. Kang, J.L. Davidson, B.K. Choi, A.B. Bonds, D.E. Cliffel, Diam. Relat. Mater. 15 (2006) 269.

[193] K.L. Soh, W.P. Kang, J.L. Davidson, S. Basu, Y.M. Wong, D.E. Cliffel, A.B. Bonds, G.M. Swain, Diam. Relat. Mater. 13 (2004) 2009.

[194] J. Park, J.J. Galligan, G.D. Fink, G.M. Swain, Anal. Chem. 78 (2006) 6756.

[195] D.C. Shin, B. V Sarada, D.A. Tryk, A. Fujishima, J. Wang, Anal. Chem. 75 (2003) 530.

[196] J. Barek, J. Fischer, T. Navrátil, K. Pecková, B. Yosypchuk, J. Zima, T. Navratil, K. Peckova, Electroanalysis 19 (2007) 2003.

[197] M. Klein, G. Schwitzgebel, Rev. Sci. Instrum. 68 (1997) 3099.

[198] E. Abelev, N. Sezin, Y. Ein-Eli, Rev. Sci. Instrum. 76 (2005) 106105.

[199] C. Albonetti, I. Bergenti, M. Cavallini, V. Dediu, M. Massi, J.-F. Moulin, F. Biscarini, Rev. Sci. Instrum. 73 (2002) 4254.

[200] R. Hobara, S. Yoshimoto, S. Hasegawa, K. Sakamoto, e-Journal Surf. Sci. Nanotechnol. 5 (2007) 94.

[201] T. Wang, H.W. Xin, Z.M. Zhang, Y.B. Dai, H.S. Shen, Diam. Relat. Mater. 13 (2004) 6.

[202] N.G. Ferreira, E. Abramof, E.J. Corat, V.J. Trava-airoldi, Carbon N. Y. 41 (2003) 1301.

[203] S. Prawer, R.J. Nemanich, Philos. Trans. A. Math. Phys. Eng. Sci. 362 (2004) 2537.

[204] A.C. Ferrari, J. Robertson, Philos. Trans. A. Math. Phys. Eng. Sci. 362 (2004) 2477.

[205] L.L. Silva, E.J. Corat, R.C. Barros, V.J. Trava-Airoldi, N.F. Leite, K. Iha, Mater. Res. 2 (1999) 99.

[206] P.W. May, W.J. Ludlow, M. Hannaway, P.J. Heard, J.A. Smith, K.N. Rosser, Diam. Relat. Mater. 17 (2008) 105.

[207] S. Wang, V.M. Swope, J.E. Butler, T. Feygelson, G.M. Swain, Diam. Relat. Mater. 18 (2009) 669.

[208] P. Achatz, E. Bustarret, C. Marcenat, R. Piquerel, T. Dubouchet, C. Chapelier, A.M. Bonnot, O.A. Williams, K. Haenen, W. Gajewski, J.A. Garrido, M. Stutzmann, Phys. Status Solidi 206 (2009) 1978.

[209] N.G. Ferreira, E. Abramof, E.J. Corat, N.F. Leite, V.J. Trava-Airoldi, Diam. Relat. Mater. 10 (2001) 750.

[210] T. Lin, K.P. Loh, A.T.S. Wee, Z.X. Shen, J. Lin, C.H. Lai, Q.J. Gao, T.J. Zhang, Diam. Relat. Mater. 9 (2000) 1703.

[211] D. Das, R.N. Singh, Int. Mater. Rev. 52 (2007) 29.

[212] P. Wurzinger, P. Pongratz, P. Hartmann, R. Haubner, B. Lux, 6 (1997) 763.

[213] S. Michaelson, A. Hoffman, Diam. Relat. Mater. 14 (2005) 470.

[214] R.J. Zhang, S.T. Lee, Y.W. Lam, Diam. Relat. Mater. 5 (1996) 1288.

[215] M. Hupert, A. Muck, J. Wang, J. Stotter, Z. Cvackova, S. Haymond, Y. Show, G.M. Swain, R. Wang, Diam. Relat. Mater. 12 (2003) 1940.

[216] M. Knupfer, Surf. Sci. Rep. 42 (2001) 1.

[217] O.A. Williams, M. Nesladek, M. Daenen, S. Michaelson, A. Hoffman, E. Osawa, K. Haenen, R.B. Jackman, Diam. Relat. Mater. 17 (2008) 1080.

[218] A.S. Barnard, M. Sternberg, J. Phys. Chem. B 110 (2006) 19307.

[219] S. Alehashem, F. Chambers, J.W. Strojek, G.M. Swain, R. Ramesham, Anal. Chem. 67 (1995) 2812.

[220] M.C. Granger, M. Witek, J.S. Xu, J. Wang, M. Hupert, A. Hanks, M.D. Koppang, J.E. Butler, G. Lucazeau, M. Mermoux, J.W. Strojek, G.M. Swain, Anal. Chem. 72 (2000) 3793.

[221] G.M. Swain, R. Ramesham, Anal. Chem. 65 (1993) 345.

[222] A.E. Fischer, Y. Show, G.M. Swain, Anal. Chem. 76 (2004) 2553.

[223] E.E. Stansbury, R.A. Buchanan, Fundamentals of Electrochemical Corrosion, ASM International, U.S, 2000.

[224] H.S. Isaacs, G. Kissel, J. Electrochem. Soc. 119 (1972) 1628.

[225] A.C. Bastos, A.M. Simões, M.G. Ferreira, Port. Electrochim. Acta 21 (2003) 371.

[226] S. Rossi, M. Fedel, F. Deflorian, M.D. Vadillo, Comptes Rendus Chim. 11 (2008) 984.

[227] P. Roberge, Corrosion Engineering: Principles and Practice, McGraw-Hill, New York, 2008.

[228] P. Marcus, F. Mansfeld, Analytical Methods in Corrosion Science and Engineering, CRC Press, Florida, 2006.

[229] Y. Gonzalez-Garcia, J.J. Santana, J. Gonzalez-Guzman, J. Izquierdo, S. Gonzalez, R.M. Souto, Y. González-García, J. González-Guzmán, S. González, Prog. Org. Coatings 69 (2010) 110.

[230] S. Gonzalez, J.J. Santana, Y. Gonzalez-Garcia, L. Fernandez-Merida, R.M. Souto, S. González, Y. González-García, L. Fernández-Mérida, Corros. Sci. 53 (2011) 1910.

[231] K. Eckhard, X. Chen, F. Turcu, W. Schuhmann, Phys. Chem. Chem. Phys. 8 (2006) 5359.

[232] K. Eckhard, W. Schuhmann, Analyst 133 (2008) 1486.

[233] A. Davoodi, J. Pan, C. Leygraf, S. Norgren, Electrochim. Acta 52 (2007) 7697.

[234] A.M. Simoes, A.C. Bastos, M.G. Ferreira, Y. Gonzalez-Garcia, S. Gonzalez, R.M. Souto, Corros. Sci. 49 (2007) 726.

[235] K. Mansikkamaki, U. Haapanen, C. Johans, K. Kontturi, M. Valden, J. Electrochem. Soc. 153 (2006) B311.

[236] Y. González-García, J.M.. Mol, T. Muselle, I. De Graeve, G. Van Assche, G. Scheltjens, B. Van Mele, H. Terryn, Electrochem. Commun. 13 (2011) 169.

[237] M. Amaral, E. Salgueiredo, F.J. Oliveira, A.J.S. Fernandes, F.M. Costa, R.F. Silva, Surf. Coatings Technol. 200 (2006) 6409.

[238] C.L. Wang, A. Hatta, N. Jiang, J.H. Won, T. Ito, A. Hiraki, Z.S. Jin, G.T. Zou, Thin Solid Films 308 (1997) 279.

[239] J. Zhao, J. Wang, J. Zhi, Z. Zhang, Sci. China Chem. 53 (2010) 1378.

[240] J. Park, H.K. Chang, H. Ha, M.S. Kim, H.J. Ahn, Y.S. Kim, J. Surg. Res. 150 (2008) 17.

[241] P.S. Siew, K.P. Loh, W.C. Poh, H. Zhang, Diam. Relat. Mater. 14 (2005) 426.

[242] Z. Chomisteková, J. Sochr, J. Svítková, Ľ. Švorc, 4 (2011) 11.

[243] N.Y. Stozhko, N.A. Malakhova, M. V. Fyodorov, K.Z. Brainina, J. Solid State Electrochem. 12 (2007) 1219.

[244] A.C. Bastos, O. V. Karavai, M.L. Zheludkevich, K.A. Yasakau, M.G.S. Ferreira, Electroanalysis 22 (2010) 2009.

[245] J. Rogalska, M.M. Brzóska, A. Roszczenko, J. Moniuszko-Jakoniuk, Chem. Biol. Interact. 177 (2009) 142.

[246] L.C. Costello, R.B. Franklin, P. Feng, Mitochondrion 5 (2005) 143.

[247] Z. Luo, X.-Y. Tan, J.-L. Zheng, Q.-L. Chen, C.-X. Liu, Aquaculture 319 (2011) 150.

[248] B. Szewczyk, M. Sowa, A. Czupryn, J.M. Wierońska, P. Brański, K. Sadlik, W. Opoka, W. Piekoszewski, M. Smiałowska, J. Skangiel-Kramska, A. Pilc, G. Nowak, Brain Res. 1090 (2006) 69.

[249] Y. You, E. Tomat, K. Hwang, T. Atanasijevic, W. Nam, A.P. Jasanoff, S.J. Lippard, Chem. Commun. (Camb). 46 (2010) 4139.

[250] S. Yilmaz, S. Yagmur, G. Saglikoglu, M. Sadikoglu, 4 (2009) 288.

[251] K. Strasunske, Ø. Mikkelsen, G. Billon, Electroanalysis 22 (2010) 501.

[252] E. Tada, S. Satoh, H. Kaneko, Electrochim. Acta 49 (2004) 2279.

[253] A.C. Bastos, M.G. Taryba, O.V. Karavai, M.L. Zheludkevich, S.V. Lamaka, M.G.S. Ferreira, Electrochem. Commun. 12 (2010) 394.

[254] V.K. Gupta, R.N. Goyal, M. Al Khayat, P. Kumar, N. Bachheti, Talanta 69 (2006) 1149.

[255] E.A. McGaw, G.M. Swain, Anal. Chim. Acta 575 (2006) 180.

[256] P. Sonthalia, E. McGaw, Y. Show, G.M. Swain, Anal. Chim. Acta 522 (2004) 35.

[257] M. Anik, Corros. Sci. 48 (2006) 4158.

[258] P. Monk, Fundamentals of Electroanalytical Chemistry, John Wiley & Sons, Inc., West Sussex, 2001.

[259] E. Tada, K. Sugawara, H. Kaneko, Electrochim. Acta 49 (2004) 1019.

[260] L.M. Baugh, Electrochim. Acta 24 (1979) 657.

[261] T. Hurlen, K.P. Fischer, J. Electroanal. Chem. Interfacial Electrochem. 61 (1975) 165.

[262] J.T. Kim, J. Jorné, J. Electrochem. Soc. 127 (1980) 8.

[263] P. Jussieu, C. Cachet, R. Wiart, J. Appl. Electrochem. 20 (1990) 1009.

[264] X.G. Zhang, Corrosion and Electrochemistry of Zinc, Plenum Press, New York, 1996.

[265] S. Jouanneau, L. Recoules, M.J. Durand, A. Boukabache, V. Picot, Y. Primault, A. Lakel, M. Sengelin, B. Barillon, G. Thouand, Water Res. 49C (2013) 62.

[266] V. 13- Corrosion, ASM Handbook, 9th ed., 1987.

[267] A.J. Bard, F.R.F. Fan, D.T. Pierce, P.R. Unwin, D.O. Wipf, F.M. Zhou, Science (80-.). 254 (1991) 68.

[268] H.S. Isaacs, Corrosion 43 (1987) 594.

[269] K.B. Deshpande, Corros. Sci. 52 (2010) 2819.

[270] H. Krawiec, V. Vignal, R. Oltra, Electrochem. Commun. 6 (2004) 655.

[271] M.C. Yan, V.J. Gelling, B.R. Hinderliter, D. Battocchi, D.E. Tallman, G.P. Bierwagen, Corros. Sci. 52 (2010) 2636.

[272] K. Mansikkamaki, U. Haapanen, C. Johans, K. Kontturi, M. Valden, J. Electrochem. Soc. 153 (2006) B311.

[273] Z.T. L.C. Clark Jr., R. Wolf, D. Granger, J. Appl. Physiol. 8 (1953) 189.

[274] J. Park, J. Chang, M. Choi, J.J. Pak, D.-Y. Lee, Y.K. Pak, 2007 IEEE Sensors (2007) 1412.

[275] T.-S. Lim, J.-H. Lee, I. Papautsky, Sensors Actuators B Chem. 141 (2009) 50.

[276] M. Sosna, G. Denuault, R.W. Pascal, R.D. Prien, M. Mowlem, Sensors Actuators B Chem. 123 (2007) 344.

[277] A. Fujishima, T.N. Rao, B. V Sarada, Diam. Mater. Vii, Proc. 2002 (2001) 127.

[278] A. Hartl, E. Schmich, J.A. Garrido, J. Hernando, S.C.R. Catharino, S. Walter, P. Feulner, A. Kromka, D. Steinmuller, M. Stutzmann, A. Härtl, D. Steinmüller, Nat Mater 3 (2004) 736.

[279] H.B. Martin, A. Argoitia, J.C. Angus, U. Landau, J. Electrochem. Soc. 146 (1999) 2959.

[280] J.W. Strojek, M.C. Granger, G.M. Swain, Anal Chem 68 (1996) 2031.

[281] T. Kondo, H. Ito, K. Kusakabe, K. Ohkawa, K. Honda, Y. Einaga, A. Fujishima, T. Kawai, Diam. Relat. Mater. 17 (2008) 48.

[282] P. Merel, M. Tabbal, M. Chaker, S. Moisa, J. Margot, Appl. Surf. Sci. 136 (1998) 105.

[283] X.C. LeQuan, W.P. Kang, J.L. Davidson, B.K. Choi, Y.M. Wong, R. Barbosa, W. Lu, Diam. Relat. Mater. 18 (2009) 200.

[284] A. Denisenko, A. Romanyuk, C. Pietzka, J. Scharpf, E. Kohn, J. Appl. Phys. 108 (2010).

[285] J.I.B. Wilson, J.S. Walton, G. Beamson, J. Electron Spectros. Relat. Phenomena 121 (2001) 183.

[286] C. Vivensang, G. Turban, E. Anger, A. Gicquel, Diam. Relat. Mater. 3 (1994) 645.

[287] K. Kanda, N. Yamada, K. Yokota, M. Tagawa, M. Niibe, M. Okada, Y. Haruyama, S. Matsui, Diam. Relat. Mater. 20 (2011) 703.

[288] R.M. Wightman, J. Electroanal. Chem 217 (1987) 417.

[289] I.C. Wang, Chem. Eng. Sci. 43 (1988) 3093.

[290] A. Argoitia, H.B. Martin, J.C. Angus, U. Landau, Proc. Fifth Int. Symp. Diam. Mater. 97 (1998) 364.

[291] M. V Mirkin, Mikrochim. Acta 130 (1999) 127.

[292] N. Sato, Corrosion 45 (1989) 354.

[293] B.P. Nadappuram, K. McKelvey, R. Al Botros, A.W. Colburn, P.R. Unwin, Anal. Chem. 85 (2013) 8070.

[294] H.J. X. Zhang J. Wang, Electrochemical Sensors, Biosensors and Their Biomedical Applications, Elsevier, New York, 2008.

[295] J.A. Garrido, A. Hardl, S. Kuch, M. Stutzmann, O.A. Williams, R.B. Jackmann, A. Härtl, Appl. Phys. Lett. 86 (2005) 073504.

[296] M. Dankerl, A. Reitinger, M. Stutzmann, J.A. Garrido, Phys. Status Solidi-Rapid Res. Lett. 2 (2008) 31.

[297] D.E. Yates, S. Levine, T.W. Healy, J. Chem. Soc. Trans. I 70 (1974) 1807.

[298] T.N. Rao, D.A. Tryk, K. Hashimoto, A. Fujishima, J. Electrochem. Soc. 146 (1999) 680.

[299] R.C. Thomas, J. Physiol. (1974) 159.

[300] M. Taryba, S.V. Lamaka, D. Snihirova, M.G.S. Ferreira, M.F. Montemor, W.K. Wijting, S. Toews, G. Grundmeier, Electrochim. Acta 56 (2011) 4475.